THEORETICAL MODELING OF ELECTRON TRANSPORT IN MOLECULAR DEVICES

A Dissertation

Presented to the Faculty of the Graduate School

of Cornell University

in Partial Fulfillment of the Requirements for the Degree of

Doctor of Philosophy

by

Haitao Wang

May 2009

THEORETICAL MODELING OF ELECTRON TRANSPORT IN MOLECULAR DEVICES

Haitao Wang, Ph.D.

Cornell University 2009

Modern electronics technology has reached a very sophisticated stage. Requirements for smaller and reliable devices are becoming more and more demanding. It is predicted that Moore's law in making a faster CPU is going to break down in the foreseeable future. People start to look into new materials in the hope that soon in the future, one can replace silicon in fabricating computer chips.

Many novel properties arise in meso- and nanoscale systems, among which electron transport properties of such systems are of particular interest to us. Due to the small sizes of the systems, a full quantum mechanical description of the electrons is required. In general, materials used in electron transport studies can be categorized into three kinds: (i) single molecular systems, which have well-defined finite molecular structures, and well quantized energy levels, including π conjugated molecules, such as benzene-dithiol, β-carotene and metal-ligand clusters, such as cobalt bis(terpyridyl) complex and a lot more; (ii) extended "molecules" with repeated structures, such as carbon nanotubes and graphene sheets. These systems typically show continuous energy dispersions in one or more dimensions and quantized subbands in the other dimensions; (iii) quantum dots, which are small fragments of crystalline semiconductors, such as CdSe or Si, with many thousands of atoms. The quantum effects in such systems are usually tuned by adjusting the sizes of these dots.

In this thesis, we used theoretical tools such as the equation of motion

Green's function technique, non-equilibrium Green's functions and linear response theory to try to understand the physics underlying the electron transport processes in some of the systems mentioned above.

In particular, we used an equation of motion Green's function technique combined with the non-equilibrium Green's function formalism to study the effects arising from the electron-electron interaction in the electron transport process. In model calculations we found extra structure for the current-voltage relation at higher biases as compared to the one calculated at a mean-field level. We also studied the Coulomb blockade problem that has been experimentally realized in molecular systems such as cobalt bis(terpyridyl) complex where the effects of gating and bias voltage play an important role. The correct description of electron self-interaction effects were found to be crucial to reproducing the correct Coulomb blockade behaviour. For materials with extended structure, we studied the effects of various static scattering sources on the transmission of electrons through graphene nanoribbons, and further the effects of gating, in particular, in relation to the so-called Klein paradox in graphene. Here we found an interesting subband dependent scattering process that led to significant changes in the transmission as a function of the angle of the applied gate. We also studied the effect of dynamical scattering due to electron-electron interactions in graphene nanoribbons, which were found to lead to large changes in the quantitative transmission coefficients.

BIOGRAPHICAL SKETCH

My name is Haitao Wang. I was born and raised in the city of Shijiazhuang, Hebei province, Northern China. I received my elementary school, junior high school and high school education there. Occasionally, I went out to other parts of China. But the real long stay outside my hometown was when I started my college in the University of Science and Technology of China in Eastern China in the year 2000. I took my major in polymer chemistry and later on my interest switched to theoretical chemistry. My first exposure to scientific research was in a research lab doing quantum dynamics in small systems from 2003 to 2004. The four years in college was such a wonderful experience in my life. I got to know a lot of very good friends and could still remember the hot summers we spent together and the exciting moments when we were watching the World Cup together. In June 2004, I graduated from college and moved to the United States to continue my graduate studies in the Department of Chemistry and Chemical Biology at Cornell. At Cornell, I joined Professor Garnet Kin-Lic Chan's research group. Everything seemed quite different from all my previous experience. I met a lot of people from different backgrounds, each gave me a new opportunity to look at things differently. After four and a half year's study, I will move to the west coast, and start my postdoc career in Professor Shaul Mukamel's group in the University of California at Irvine.

To my dear parents.

ACKNOWLEDGEMENTS

My foremost thank goes to my adviser Dr. Garnet Kin-Lic Chan. It is a great honor to be his first Ph.D. student. Working with him makes my Ph.D. study a unique experience. I very much appreciate all his help and guidance on shaping my research skills. Without him, this dissertation would not have been possible. I thank him for his patience and encouragement that carried me on through all these years.

I feel grateful to all the members of the Chan group. They have been very helpful in both my research and life here at Cornell. I especially thank Dr. Osamu Hino for his valuable help in the initial stage of my research in molecular transport. I greatly thank Dr. Takeshi Yanai for his valuable help in both broadening my understanding of quantum chemistry and improving my computing skills. Dr. Jesse Kinder is a great researcher to work with, he has been very helpful for a lot of topics in my graphene research. Jon Dorando is such a nice collaborator, and it has been a wonderful experience to work with him. I enjoyed working with Johannes Hachmann and feel thankful for his help from time to time, and will always miss so many nice dinner parties at his place in the early years when we got started. I would also like Dr. Dominika Zgid, Debashree Ghosh, Eric Neuscamman and the rest of the group for all their help during the years.

For years, my family have always been very supportive, and I would like to thank them for all their love and encouragement. My time at Cornell was made enjoyable in large part due to many of my friends, among whom I would like to mention Yi Liu, Lijun Fan, Rong Dong and Ying Zhang. We started at Cornell in the same year in the same department, and they have been very helpful for my teaching assistant work for the department. I also enjoyed a lot of relaxing

evenings learning cooking delicious food from them and playing cards with them together.

Finally, I would like to thank the David and Lucile Packard Foundation for funding the research.

TABLE OF CONTENTS

LIST OF TABLES

LIST OF FIGURES

CHAPTER 1

INTRODUCTION

1.1 Perspective

One of the greatest technological inventions of the last century is the transistor, first fabricated at Bell Labs in 1947, for which William Shockley, John Bardeen and Walter Brattain shared the 1956 Nobel Prize for physics. Ever since, it has become one of the key active components in almost all modern electronic devices. Typical transistors are made from inorganic crystalline semiconductors. Among these materials, crystalline silicon is probably the most important one. Compared to electronic devices made from other materials, devices based on crystalline silicon are very reliable under a wide range of conditions, and possess e.g. low energy dissipation thus greater energy efficiency, and are cheap and easy to process.

Because of the typical dimensions of fabrication, the physics of silicon devices can usually be understood at the macroscopic scale. However there is now much interest in materials and devices at smaller meso- and even molecular scales. To understand how the macroscopic and meso- or microscopic physics differ, we need to introduce three characteristic length scales.

1. the Fermi wavelength of the electrons, which is related to the kinetic energy of the electrons around the Fermi level.
2. the mean free path, which is the distance that an electron travels before its initial momentum is destroyed.

3. the phase-relaxation path, which is the distance that an electron travels before its initial phase is destroyed.

These length scales vary widely from one material to another, and can range from a few nanometers to possibly hundreds of microns. To give a few examples, in simple metals, the Fermi wavelength is at the scale of a few angstroms. While in semiconductors, the Fermi wavelength can range from 10 nanometers to 100 nanometers. And at low temperatures, the mean free path or the phase relaxation length in high mobility semiconductors is found in the range from 10 microns to possibly 100 microns.

In materials such as conventional crystalline semiconductors with dimensions that are much larger than all of these three length scales, the wave function's phase information is lost and the momenta of the electrons are also randomized across the length of the sample. Electrons in these materials can be simply described as classical particles. Consequently, these materials usually show classical ohmic conductance behaviour.

However, in materials with dimensions ranging from the meso- to nanoscale the main feature is that when passing through the sample, the momenta of the electrons get altered only to some extent, and the phase of the electronic wave functions in these systems is also largely intact. Thus the electron transport properties are among the most interesting properties of meso- and nanoscale materials because they exhibit quantum effects.

In Fig. (1.1) we show some typical mesocopic and molecular systems in which electron transport properties are studied. In general, we can group these materials into three types:

1. Single molecule materials: Here, the molecular structure is well-defined, and the energy levels are well quantized. Most of the molecular materials under investigation in the field of electron transport nowadays can be largely grouped into either π conjugated molecules such as the photosynthetic pigment β-carotene molecule shown in the upper left of Fig. (1.1), or transition metal compounds composed of a metal surrounded by some ligands such as the phthalocyanine metal complex in the upper right of Fig. (1.1).
2. Extended molecular materials: These include carbon nanotubes, graphene, and conducting polymers, as shown in the lower half of Fig. (1.1). In these materials, the molecular structure is well defined but is extended in one or more directions. This gives rise to continuous energy dispersions in one or more directions, but quantized energy levels in the other directions.
3. Quantum dots: These are typically small fragments of crystalline semiconductors, such as CdSe or Si, typically with many thousands of atoms. The quantum effects are usually tuned by adjusting the sizes of these dots.

In the following, I will briefly review the three characteristic length scales by which we can define different transport regimes. Before talking about this, I'll first introduce several basic concepts.

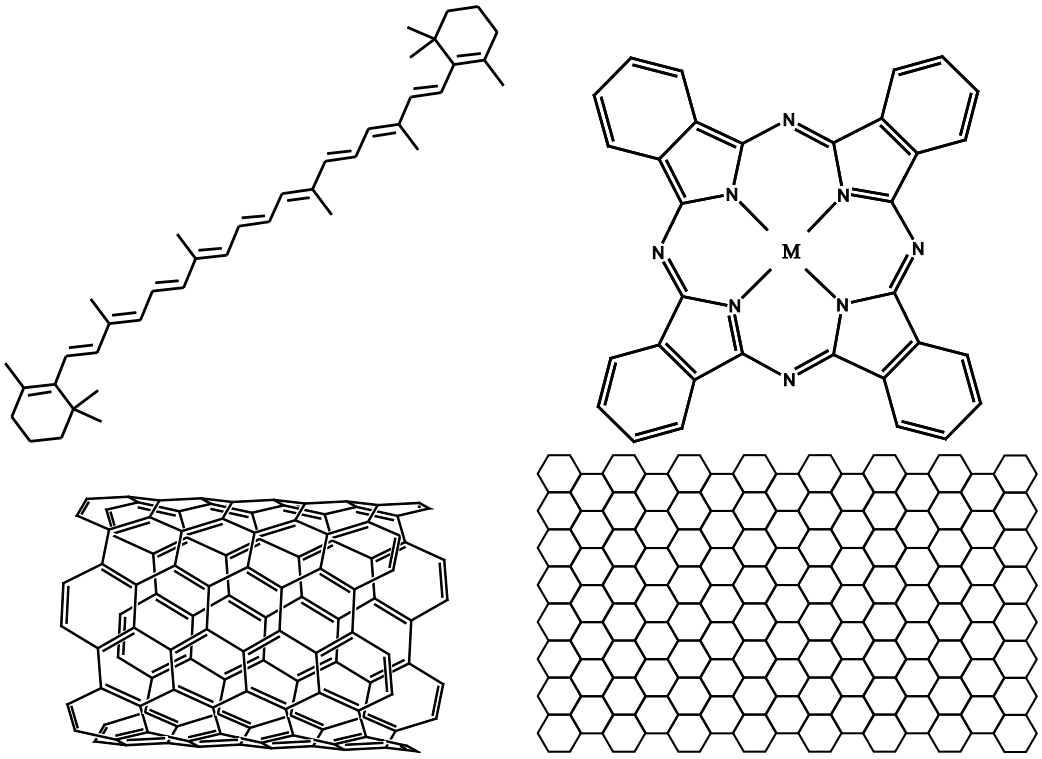

Figure 1.1: Various meso- and nanoscopic systems studied in electron transport. Top left: β-carotene; Top right: phthalocyanine metal complex; Bottom left: Single-walled carbon nanotube; Bottom right: graphene.

1.1.1 Basic concepts

Where does resistance arise?

People have been trying to understand the origin of resistance for a long time. The resistance arises due to scattering of propagating electrons by various mechanisms, including scattering with rigid static scatterers and scattering with dynamic scatterers possessing internal degrees of freedom.

- Static scatterers (fixed internal or external fields)

    1. electron interacting with an impurity

2. boundary mismatch

- Dynamic scatterers (other particles)

1. electron-electron interactions
2. electron-phonon interactions

In a lot of cases, various scattering interactions coexist, but in general one or two scattering mechanisms will dominate the electron transport process. For example, in bulk materials, near room temperature, interaction with vibrational degrees of freedom (i.e. phonons) inside of the materials is the dominant source of scattering. As we go down from room temperature, the phonon scattering is suppressed, and electron-electron scattering starts to take over. And as one keeps lowering the temperature, at lower enough temperature, the resistance will be saturated by the static impurity scattering process.

Transverse modes

It is important to bring up this terminology in the very beginning, since later on we will utilize this concept many times. Fig. (1.2) shows a basic setup for electron transport. A conductor of interest is sandwiched between two semi-infinite electrodes. The length of the conductor is L in one dimension (let us say the x-dimension) and width W for the other two dimensions (y- and z- dimensions). A bias voltage is applied across the conductor which gives rise to a difference between the chemical potentials of the two electrodes $eV = \mu_1 - \mu_2$.

Since the electrodes are sufficiently large, we will describe the electronic wave function (for a single electron) using a set of plane-waves propagating

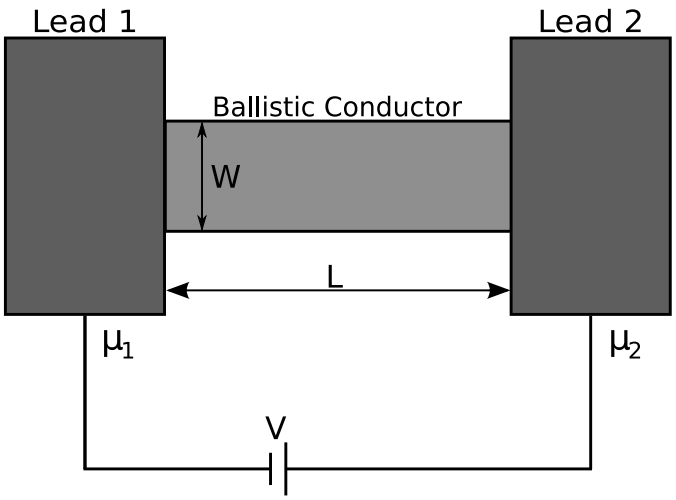

Figure 1.2: Model setup for electron transport.

in the x-direction. Due to the confinement in size in the y- and z-directions, the wavevectors k_y and k_z are quantized, while k_x could be continuous. We define the number of transverse modes as the product of the number of quantized k_y and that of k_z. People also use words such as "conduction channels", waveguides or subbands to represent transverse modes sometimes. In simple conductors in which the different transverse modes do not scatter amongst each other, the total conductance will be the simple summation of conductance from the contributions of all these modes.

1.1.2 Three characteristic length scales

- Fermi wavelength: At low temperatures the current is carried mainly by electrons having an energy close to the Fermi energy so that the Fermi wavelength $\lambda = 2\pi/k_f$ is the relevant length. Other electrons with less kinetic energy have longer wavelengths but they do not contribute to the conductance.

- Mean free path: An isolated electron in a perfect crystalline structure moves as if it were in vacuum but with a different mass. Any deviations from perfect periodicity such as interactions with impurities, vacancies, phonons and other electrons would possibly change the electron from one state to another, thus affecting its momentum. The mean free path L_m is the distance that an electron can travel before its initial momentum is destroyed, that is, $L_m = v_f \tau_m$, where v_f is the Fermi velocity and τ_m is the momentum relaxation time.
- Phase-relaxation length: Scattering not only changes the momentum of an electron, but also gives rise to a phase-shift. In analogy with the mean free path, the phase-relaxation length is the distance traveled by an electron before the original phase information is completely lost, that is, $L_\phi = v_f \tau_\phi$, where v_f is the Fermi velocity and τ_ϕ is the phase relaxation time.

Scattering with static scatterers is called elastic scattering, in which case the electronic wave function will have a definite phase shift, and the wave function remains coherent. Such elastic scattering will contribute to L_m, but not to L_ϕ. Energy is conserved in elastic scattering. On the other hand, dynamic scatters with internal degrees of freedom can possibly excite the electrons into other states which do not conserve energy. If there are a large number of internal degrees of freedom then the phase information of the electronic wave function will also be lost through dissipation. These scattering events are called inelastic scatterings, and they contribute to both L_m and L_ϕ.

As mentioned earlier, for macroscopic conductors, the resistance R is governed by Ohm's law. We use the conductor in Fig. (1.2), then it follows that,

$$R = \rho \frac{L}{W^2}, \tag{1.1}$$

where $\rho\,[\Omega m]$ is the resistivity. The inverse of R is the conductance $G\,[S]$, which is related to the conductivity $\sigma \equiv 1/\rho\left[S\,m^{-1}\right]$ by

$$G = \sigma\frac{W^2}{L}, \tag{1.2}$$

where the conductivity σ is a material property of the sample. It is worth noting that conductivity describes a local property of the material, while conductance describes the capability of electron transport in the particular systems under study. In a macroscopic conductor, which obeys Ohm's law, σ is independent of its length L, while conductance is inversely proportional to L. When the size of conductor becomes comparable with or even smaller than the three characteristic length scales mentioned above, σ will depend on L quantum mechanically. In the quantum limit, the electrons act like waves that show interference patterns. Consequently, the conductance is highly dependent on the boundary conditions of the conductor and various defects that are possibly present in the conductor.

1.1.3 Three transport regimes

We define the time that the electron spends in the conductor as the transit time τ_t. It is worth noting that when comparing the momentum relaxation time τ_m or the phase relaxation time τ_ϕ to the transit time τ_t, τ_m and τ_ϕ do not represent the time for a single scattering event, instead, they correspond to an average of many such events. The word "completely destroyed" is somehow a fuzzy terminology, to be more concrete, the relaxation time corresponds to the time that the momentum of the electron changes by a mount of $\hbar k_f$ or the phase of electronic wave function changes by π. The three characteristic length scales,

together with the length of the systems under study, determine three transport regimes: ballistic, classical, and diffusive transport.

Electron transport in the ballistic regime

In a ballistic conductor, the sample length is smaller than both the mean free path and the phase relaxation length. Thus one expects no significant scattering occurs in a ballistic conductor. The electronic wave function is purely governed by the Schrödinger equation.

We assume that we have a ballistic conductor with a finite size as shown in Fig. (1.2). We further assume that there are no reflections within the electrodes and they have well-defined chemical potentials, which we denote as μ_1 and μ_2, respectively. The current is carried by electrons with $k_x > 0$ from left to right, and the ones with $k_x < 0$ from right to left. The net current is thus carried by electrons with $k_x > 0$ with energies in the range $[\mu_2, \mu_1]$ (Here we assume that $\mu_2 < \mu_1$). The current will be proportional to the number of transverse modes M, multiplied by the number of electrons in the correct energy range. This gives

$$I = \frac{2e^2}{h} M \frac{(\mu_1 - \mu_2)}{e} == \frac{2e^2}{h} MV \tag{1.3}$$

where the constant of proportionality is the so-called conductance quantum $G_0 \equiv \frac{2e^2}{h} = 77.4809 \times 10^{-6} S$, as first derived by Landauer. The conductance is then given by:

$$G_c = G_0 M \tag{1.4}$$

In systems where various scatterers are present, different transverse modes could in principle mix with each other, the simple relation between the conductance and the number of transverse modes in Eq. (1.3) may not be valid

anymore. Nonetheless the conductance follows a similar equation, known as the Landauer formula, which we will describe in detail later

$$G_c = G_0 MT \equiv G_0 \sum_{ij}^{M} \left|t_{ij}\right|^2 \tag{1.5}$$

where T is the averaged transmission probability (also called transmission coefficient) that an electron injected in one electrode will transmit to the other electrode, and t_{ij} characterizes the transmission probability that an electron transmits from the ith channel to the jth channel. To make one thing clear, conductance quantization does not mean that the conductance measured in realistic experiments is quantized where the transmission is not perfect, rather it corresponds to the conductance of a ballistic conductor, which has perfect transmitting channels, while each channel has the transmission coefficient equal to 1. In such case, one recovers the formula (1.3).

For conductors with only a single conduction channel, i.e. $M = 1$, the resistance of the conductor is given by

$$R = \frac{1}{G_c} - \frac{1}{G_0} = \frac{h}{2e^2}\frac{1-T}{T} \equiv R_0 \frac{1-T}{T} \tag{1.6}$$

where R_0 is the resistance quantum.

Note ballistic conductors with a single channel have a *finite* resistance of R_0. This resistance arises essentially because of the mismatch between the conductor and the electrode which is supplying the electrons; the electrons have to "squeeze" themselves into a single channel in order to be conducted.

Electron transport in the classical regime

In the classical transport regime, the sample size is much larger than both the phase relaxation length and the mean free path. Electrons can be treated

as particles neglecting any quantum interference effects. Suppose the propagating electrons experience N scattering events, then the overall transmission probability T can be calculated by combining each transmission probability T_i ($i = 1, 2, \ldots, N$) and each reflection probability $R_i = 1 - T_i$ in a classical way. Considering multiple reflections that could occur during scattering event 1 and 2, the overall transmission probability after scattering event 1 and 2 reads as,

$$\begin{aligned} T_{12} &= T_1T_2 + T_1T_2R_1R_2 + T_1T_2R_1R_2R_1R_2 + \cdots \\ &= \frac{T_1T_2}{1 - R_1R_2} \end{aligned} \tag{1.7}$$

Noticing that $R_i = 1 - T_i$, we can rewrite the Eq. (1.7) as,

$$\frac{1 - T_{12}}{T_{12}} = \frac{1 - T_1}{T_1} + \frac{1 - T_2}{T_2} \tag{1.8}$$

Note that this is additive between the two scattering events. For N scattering events, we have,

$$\frac{1 - T}{T} = \sum_i^N \frac{1 - T_i}{T_i} \tag{1.9}$$

Assuming that each scattering event has the same transmission probability T_0, then we have,

$$\frac{1 - T}{T} \approx N\frac{1 - T_0}{T_0} \tag{1.10}$$

Comparing Eq. (1.6) and Eq. (1.10), from the additive nature of $\frac{1-T}{T}$, we can get,

$$\begin{aligned} R &= R_0 \sum_i^N \frac{1 - T_i}{T_i} \\ &\approx NR_0\frac{1 - T_0}{T_0} \end{aligned} \tag{1.11}$$

Now assuming that the number of scatterers in the sample is proportional to the length of the sample, combined with the fact that R is additive (from Eq. (1.11)), we can now conclude that in the classical transport regime, the conductance follows Ohm's law.

Electron transport in the diffusive regime

In the diffusive regime, the sample size is smaller than the phase relaxation length, but much larger than the mean free path. As a result, the electron wave remains coherent, but the electron has experienced many elastic scatterings before getting out from the conductor. We can model this process by a diffusion equation for the current J.

$$J = eD\nabla n \tag{1.12}$$

where D is the diffusion coefficient and n is the electron density. We can rewrite ∇n in terms of the number of electrons per unit energy (density of states N_s) and the change in chemical potential across the sample, giving,

$$J = e^2 D N_s \frac{\mu_1 - \mu_2}{eL} = e^2 D N_s E \tag{1.13}$$

where E is the electric field across the conductor. From the relationship between conductivity and current $J = \sigma E$, we get,

$$\sigma = e^2 D N_s \tag{1.14}$$

An alternative approach to get the conductivity is to view the current as a drift of all the electrons below the Fermi level, which gives rise to the current as,

$$J = e n_s v_d \tag{1.15}$$

where v_d is the drift velocity of the electrons.

To get v_d, we have,

$$\left[\frac{\Delta p}{\Delta t}\right]_{scattering} = \left[\frac{\Delta p}{\Delta t}\right]_{field} \tag{1.16}$$

Thus,

$$\frac{m v_d}{\tau_m} = eE \Rightarrow v_d = \frac{e\tau_m}{m} E \tag{1.17}$$

Using Eq. (1.15) and Eq. (1.17), we have,

$$\sigma = en_s\mu \tag{1.18}$$

where the mobility is defined as $\mu \equiv \frac{v_d}{E} = \frac{e\tau_m}{m}$.

Comparing Eq. (1.14) and Eq. (1.18), we have,

$$\frac{e}{\mu}D = \frac{n_s}{N_s} = E_f - E_s = \frac{1}{2}mv_f^2 \tag{1.19}$$

where E_s is the bottom of the band and E_f stands for the Fermi level.

Thus by using Eq. (1.19) and the definition for the mobility, we have the diffusion coefficient given by $D = \frac{1}{2}v_f^2\tau_m$.

1.2 Quantum description of electron transport

The success of the scanning tunneling microscope (STM) and the conducting atomic force microscope (AFM) have greatly boosted basic research in the field of electron transport at meso- and nanoscopic scales. Some of the early experimental studies used systems like single fullerene molecules [1], copper(II) phthalocyanine metal complexes [2] and conductive π-conjugated carotene molecules [3]. As mentioned in the last section, in order to understand the electron transport properties of these molecular systems, a full quantum description of the process is required. We will now start with the simplest quantum theory of such kinds, namely, the Landauer formula.

1.2.1 Landauer formula

In the Landauer approach one imagines that there is a small region (which we call here the "molecule" region), which could be a small molecule or quantum dot, connected to two macroscopic electrodes. (People commonly also use the word contacts, reservoirs or leads to denote the electrodes). It is sometimes theoretically convenient to include a portion of the electrode into the molecule region in order to eliminate any effects from geometrical or charge rearrangement due to the presence of the molecule. But in principle this is not necessary. The electrodes are assumed to be simple ballistic conductors, therefore any internal scattering processes are neglected. Because of their macroscopic size, even when a finite voltage bias is applied across the molecule region from one electrode to the other, driving the molecule out of equilibrium, the electrodes maintain well-defined chemical potentials.

Based on Landauer [4], electron transport, in such a setup, should be regarded as a scattering problem: an incoming electron flux from one electrode is scattered by the molecule and transmitted to the other electrode. We will here derive the Landauer formula without any loss of the major features. A more rigorous derivation of the Landauer formula can be found in Ref. [5]. Let us consider for simplicity a two-dimensional system in which the potential along the x-direction is uniform and in the y-direction we have some transverse confining potential U(y) (e.g. a harmonic potential). Here the z-dimension is squeezed, leading to an energy quantization ε_z with very large spacings in the z dimension. For most of the time, the system stays at the lowest energy levels of ε_z, thus the z-dimension can be safely neglected in the following discussion.

The Schrödinger equation for the conductor is then given by:

$$\left[\frac{p^2}{2m} + U(y)\right]\Psi(x,y) = E\Psi(x,y) \tag{1.20}$$

where p is two dimensional, i.e. $p = (p_x, p_y)$. The solutions to the equation read as,

$$\Psi_{nk}(x,y) = \frac{1}{\sqrt{L}} e^{ik_x x}\chi_n(y) \tag{1.21}$$

where L is the length of the conductor over which the wave functions are normalized. The potential $U(y)$ gives rise to quantized transverse modes $\chi_n(y)$. The dispersion relation $E_n(k)$ in this particular case is quadratic for each mode n, and different modes are separated with a constant energy spacing (due to the harmonic confining potential). At a fixed energy E, there will be a finite number $M(E)$ of modes crossing that energy. One then assumes that the application of a bias voltage to the electrodes simply shifts the chemical potentials of the reservoirs such that $\mu_L - \mu_R = eV$ (Here we assume that $\mu_R < \mu_L$). The electrons in the left electrode corresponding to positive momentum in the x direction (+k) are occupied with the Fermi distribution $f_L(\mu_L)$ and the ones with negative momentum (-k) in the right electrode are occupied with the Fermi distribution $f_R(\mu_R)$. We assume that the molecular levels are largely unaffected by the application of the bias voltage.

With these assumptions we are now in a position to compute the current. We know that uniform electron gas with n electrons per unit length moving with group velocity $v = \frac{1}{\hbar}\frac{\partial E}{\partial k}$ carries a current given by $I = env$. Given that the electron density of a single +k state in a conductor of length L is $1/L$, the current carried by the +k states coming from the left electrode is then given by,

$$I^+ = \frac{e}{L}\sum_k v_k f_L(E_k) = \frac{e}{L}\sum_k \frac{1}{\hbar}\frac{\partial E_k}{\partial k} f_L(E_k) \tag{1.22}$$

In one-dimension, we have, in the integral form (we will drop the subscript k of E),

$$\sum_k \to 2 \times \frac{L}{2\pi} \int dk = 2 \times \frac{L}{2\pi} \int \frac{\partial k}{\partial E} dE \tag{1.23}$$

where the "2" in front of the integral stands for the spin.

Combining Eq. (1.22) and Eq. (1.23), the current carried by $+k$ states from all the transverse modes then reads as,

$$I^+ = \frac{2e}{h} \int_{-\infty}^{\infty} f_L(E)\, M(E)\, dE \tag{1.24}$$

In the same way we can calculate the contribution to the current from states with negative momentum $-k$ coming from the right electrode,

$$I^- = \frac{2e}{h} \int_{-\infty}^{\infty} f_R(E)\, M(E)\, dE \tag{1.25}$$

Combining the left and right currents, the total current is,

$$I = I^+ - I^- = \frac{2e}{h} \int_{-\infty}^{\infty} [f_L(E) - f_R(E)]\, M(E)\, dE \tag{1.26}$$

If we assume that the number of modes is constant over the energy range $\mu_R < E < \mu_L$, we get, at zero temperature:

$$I(V) = \frac{2e^2}{h} M \frac{\mu_L - \mu_R}{e} = \frac{2e^2}{h} MV \tag{1.27}$$

The conductance reads as,

$$G_C = \frac{2e^2}{h} M \tag{1.28}$$

In more general cases,

$$G_C = \frac{2e^2}{h} MT (Landauer\, formula) \tag{1.29}$$

where T is the transmission coefficient for a single mode. For a more rigorous derivation of the Landauer formula, we refer to Ref. [6].

So far, we have assumed that the molecular levels (which determine the number of transverse modes M and the transmission probability T) are unaffected by the applied bias. However, when the applied bias is strong, one can show that the current still takes the same general form

$$I(V) = \frac{2e}{h} \int_{-\infty}^{\infty} \tilde{T}(E) \left[f_L(E) - f_R(E) \right] dE \tag{1.30}$$

Here we have dropped our assumption that M and T are energy-independent, and $\tilde{T}(E) = T(E)M(E)$. In the linear response regime and at low temperatures, the conductance is given by

$$G_C = \frac{2e^2}{h} \tilde{T}\left(E_f\right) \tag{1.31}$$

where E_f is the Fermi energy of the system.

1.2.2 When will the Landauer formula fail to work?

To briefly summarize this chapter, in deriving the Landauer formula, we have made the following assumptions,

- In the electrodes, internal scatterings are neglected.
- The electrodes are sufficiently large, that the bias voltage simply shifts the chemical potentials of the electrodes but does not change the Fermi distribution of the electrons in the electrodes.
- The electrodes and the molecule are not coupled through electron-electron interactions.

Another assumption that is implicitly made in our derivation is that the electrons are coherently propagating through the sample, that is, the phase information of the wave function is maintained. Naturally, one might ask the following question: does the Landauer formula remain valid when the electron transport process is incoherent. To answer this question, we first need to introduce the concept of vertical flow.

In certain systems, the electron-electron interactions or the electron-phonon interactions could be sufficiently strong that the propagating electron undergoes an excitation process to access other energies, thus exiting the sample from a very different energy channel compared to the starting channel, as shown in Fig. (1.3). In such a process, one needs to take extra care of the exclusion principle for electrons. It can be proved that in an incoherent process where the transmission coefficient remains uniform across the range of energy change, the Landauer formula remains valid [5]. But one would expect that the Landauer formula needs to be corrected in an incoherent process where the transmission coefficient changes drastically over the energy range of interest, for which the correction is by no means straightforward. Instead, an alternative way to handling incoherent processes due to electron-electron or electron-phonon interactions is necessary, as we will discuss in the following chapters.

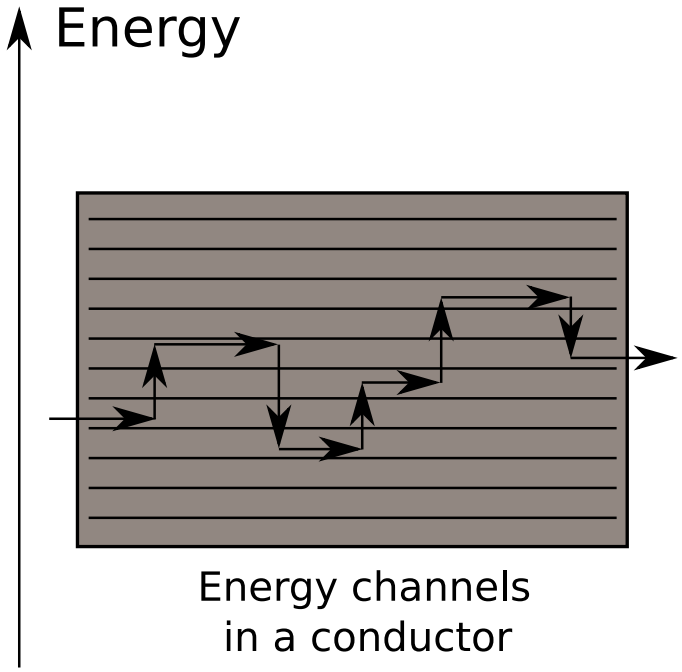

Figure 1.3: Propagating electrons undergo vertical flow in inelastic scattering process.

1.3 Organization of this thesis

In this introduction, I have discussed briefly the various electron transport theories, as well as some basic key concepts that need to be understood properly. The rest of this thesis is organized as follows.

1. The second chapter describes the non-equilibrium Green's function formalism and the equation of motion Green's function technique. This is an attempt to go beyond the single-particle Landauer formalism, in particular to include the effects of electron-electron interactions. We compare various equation of motion approximations to obtain the current-voltage relation.
2. The third chapter describes a Coulomb blockade study on a cobalt

bis(terpyridyl) cluster. This is a study of how the standard Landauer picture used in a mean-field way performs in more difficult cases of electron transport. A discussion of the effect of self-interaction error in mean-field theories of electron transport is included. Part of this chapter appears in the published article [7].

3. The fourth chapter describes an application of basic Landauer theory to scattering problems in two-dimensional graphene sheets. A portion of this chapter (Klein scattering) appears in expanded form, as part of the article [8] is submitted to Nano Letters.

4. The fifth chapter provides some conclusions from previous chapters and gives some ideas for future directions.

BIBLIOGRAPHY

[1] C. Joachim and J. K. Gimzewski. An Electromechanical Amplifier Using a Single Molecule. *Chem. Phys. Lett.*, 265:353, 1997.

[2] G. V. Nazin, X. H. Qin, and W. Ho. Visualization and Spectroscopy of a Metal-Molecule-Metal Bridge. *Science*, 302:77, 2003.

[3] G. Leatherman, E. N. Durantini, D. Gust, T. A. Moore, A. L. Moore, S. Stone, Z. Zhou, P. Rez, Y. Z. Liu, and S. M. Lindsay. Carotene as a Molecular Wire: Conducting Atomic Force Microscopy. *J. Phys. Chem. B*, 103:4006, 1999.

[4] R. Landauer. Spatial Variation of Currents and Fields Due to Localized Scatterers in Metallic Conduction. *IBM J. Res. Dev.*, 1:223, 1957.

[5] S. Datta. *Electronic Transport in Mesoscopic Systems*. Cambridge University Press, 1995.

[6] H. D. Cornean, A. Jensen, and V. Moldoveanu. A rigorous proof of Landauer-Büttiker formula. *J. Math. Phys.*, 46:042106, 2005.

[7] H. Wang and G. K.-L. Chan. Self-Interaction and Molecular Coulomb Blockade Transport in Ab Initio Hartree-Fock Theory. *Phys. Rev. B*, 76:193310, 2007.

[8] J. Kinder, J. Dorando, H. Wang, and G. K.-L. Chan. Perfect Reflection of Chiral Fermions in Gated Graphene Nanoribbons. *submitted to Nano Letters*, 2008.

CHAPTER 2

ELECTRON TRANSPORT VIA THE NON-EQUILIBRIUM GREEN'S FUNCTION FORMALISM AND AN EQUATION OF MOTION GREEN'S FUNCTION TECHNIQUE

2.1 Introduction and motivation

As mentioned in the introduction, the Landauer formula has a wide range of applicability even though it is based on a single-particle description. However, in systems where the propagating electrons interact strongly with other degrees of freedom, such as other electrons or phonons, static potentials, etc., the validity of the Landauer description is not so clear. Thus alternative methods are called for to correctly describe the electron transport process under such conditions.

The following picture (Fig. (2.1)) gives a schematic illustration of the electron transport setup in molecular devices. The molecular device bridges two electrodes which function as reservoirs of electrons. At equilibrium, all three parts share the same chemical potential, thus no charge carrier flow occurs. When a bias voltage, in this case, $eV = \mu_L - \mu_R$, is applied across the molecular device, the current will be driven from the left electrode to the right electrode. In such a case, the system is in a non-equilibrium state. Because charge transport is inherently a non-equilibrium process we will work with a non-equilibrium Green's function (NEGF) formalism for charge transport (sometimes also called the Keldysh formalism) in the following sections.

If we wish to study scattering processes, such as the electron-electron interactions within the molecular devices beyond the Landauer formula, we are led

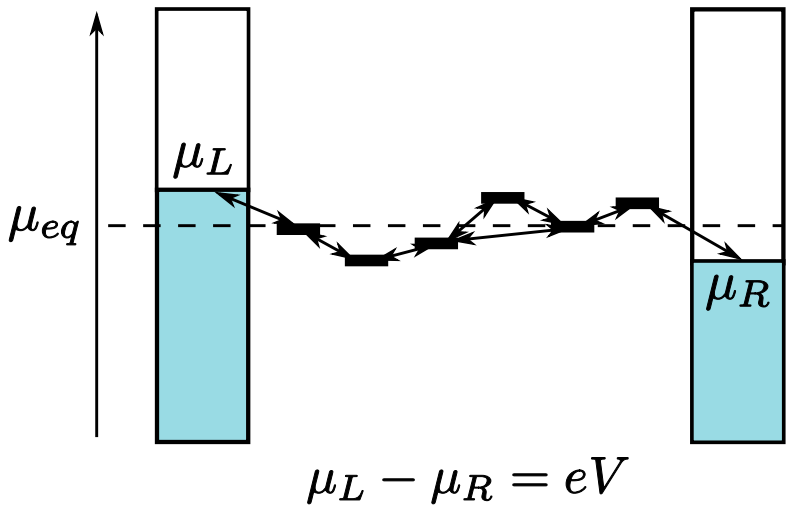

Figure 2.1: Schematic view of electron transport under non-equilibrium condition.

naturally to consider Green's functions within a many-body framework. The exact expressions for the current and conductance using exact many-body Green's functions were first derived by Meir and Wingreen. This does not however, provide a method to calculate these quantities. Early analytic studies of Kondo transport through quantum dots employed the equation of motion technique (typically together with some analytic approximations such as the non-crossing approximation) to provide a tractable route to obtain the many-body Green's function excitations. In this chapter, we provide a preliminary study of how such an equation of motion technique may be generalized so as to be usable in the same numerical computational framework as typically employed in Landauer type calculations of transport.

2.2 Non-equilibrium Green's function formalism

Green's functions are widely used to solve inhomogeneous differential equations such as the Schrödinger equation in quantum mechanics (see Appendix for a more detailed introduction to Green's functions). Using Green's functions, a wide variety of useful physical observables can be calculated conveniently, such as the density of states, electron density, spectrum of the system, and response properties such as the differential conductance. In the following we will show that Green's functions provide a convenient way to treat various scattering processes in the electron transport problem that we are interested in.

For simple non-interacting systems, the non-equilibrium Green's function formalism is not that much different from Landauer's formalism. The power of the NEGF formulation is the possibility of extending the description of the electron transport problem beyond the single-particle picture in order to include electron-electron interactions and other scattering contributions such as electron-phonon interactions. This is particularly important for systems in which such scattering processes dominate, in which the Landauer formula could yield qualitatively incorrect answers.

The Meir-Wingreen NEGF expression for the non-equilibrium current

To start with, we imagine a molecular conductance setup with a molecule sandwiched between two electrodes. We partition this system into three parts: the left electrode, a molecular part and the right electrode, as shown in Fig. (2.2). The electrodes and molecule carry electronic degrees of freedom, which we shall refer to as sites. These sites may be orbitals in either a localized form (such as

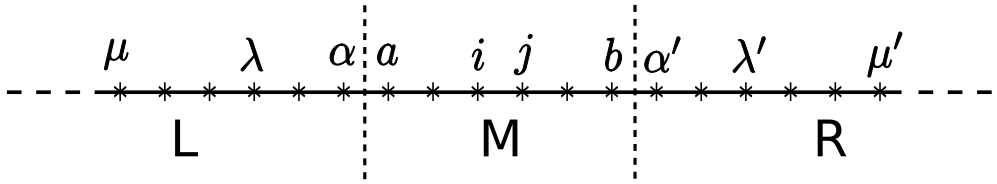

Figure 2.2: Partitioning of the system: Greek letters represent sites in the electrodes and English letters represent sites in the molecular part.

atomic orbitals) or a more delocalized from (molecular orbitals or plane-waves). Here we use Greek letters to represent sites in the electrodes and English letters to represent sites in the molecular part.

The total Hamiltonian is given by,

$$\mathcal{H}_{total} = \mathcal{H}_{mol} + \mathcal{H}_{elec} + \mathcal{H}_{mol-elec} \tag{2.1}$$

where

$$\mathcal{H}_{mol} = \sum_{ij\in M} h_{ij} c_i^\dagger c_j + \sum_{ijkl\in M} h_{ijkl} c_i^\dagger c_j^\dagger c_l c_k \tag{2.2}$$

$$\mathcal{H}_{elec} = \sum_{\mu,\nu\in L,R} h_{\mu\nu} c_\mu^\dagger c_\nu \tag{2.3}$$

$$\mathcal{H}_{mol-elec} = \sum_{\substack{\mu\in L,R \\ m\in M}} \left[h_{\mu m} c_\mu^\dagger c_m + h.c. \right] \tag{2.4}$$

For most electron transport calculations, it is assumed that the electrodes are described by a single-particle Hamiltonian as shown in Eq. (2.3), and that the couplings between electrodes and molecule are also of single-particle form as shown in Eq. (2.4). We also take these two assumptions in our following calculations. For the molecular part, we are interested in effects on transport due to electron-electron interactions, thus we include the two-electron terms as shown in the second term of Eq. (2.2).

First we need a form for the current operator. This was first explicitly derived

in Ref. [1]. Following the charge conservation law, the current $\mathcal{J}$ at any given position x satisfies the continuity equation.

$$\nabla \cdot \mathcal{J}(x) = -\frac{\partial \rho(x)}{\partial t} \tag{2.5}$$

where $\rho(x)$ is the electron density at position x. We can take a discretized form of the gradient operator. Here we choose a site i within the left electrode (in principle we can choose any site in the system, as in steady state, the current is uniform everywhere).

$$J_P - J_{P'} + \frac{\partial \rho_i}{\partial t} = 0 \tag{2.6}$$

where we imagine P to lie between sites $i, i+1$, P' to lie between sites $i-1, i$, and ρ_i is the electron density at site i, given by the expectation value of $ec_i^\dagger c_i$. We assume J_P to take the form

$$J_P = \sum_{l \geq i+1, m \leq i} A_{lm} c_l^\dagger c_m + h.c. \tag{2.7}$$

From the equation of motion of ρ_i,

$$i\hbar \frac{\partial \rho_i}{\partial t} = [\rho_i, \mathcal{H}_{total}] \tag{2.8}$$

and from comparison with our assumed form of J_P, we obtain $A_{lm} = \frac{e}{i\hbar} h_{lm}$. Hence the current that flows out of the left electrode can be written as

$$\mathcal{J}_L = \frac{ie}{\hbar} \sum_{\substack{\lambda \in L \\ m \in M}} \left[h_{\lambda m} \langle c_\lambda^\dagger c_m \rangle - h_{\lambda m}^* \langle c_m^\dagger c_\lambda \rangle \right] \tag{2.9}$$

It is clear from Eq. (2.9), that the current contains contributions from two terms. The first term stands for the current going from the molecule to the left electrode, and the second term stands for the current going from the left electrode to the molecule. Following the definitions of Green's functions (see Appendix), Eq. (2.9) can then be expressed by the lesser Green's functions that connect the

molecular part and the left electrode as shown in Eq. (2.10).

$$\mathcal{J}_L = \frac{e}{\hbar} \sum_{\substack{\lambda \in L \\ m \in M}} \left[h_{\lambda m} \mathcal{G}^<_{m,\lambda} - h^*_{\lambda m} \mathcal{G}^<_{\lambda,m} \right] \tag{2.10}$$

The above formula for the current, while formally exact, is inconvenient, because it involves the matrix elements of a Green's function coupling both the molecule and the (macroscopic) electrodes. This implies that we need to know the quantum state of the entire coupled molecule-electrode system to evaluate the current! Meir and Wingreen showed in Ref. [2] that it was possible to obtain the current in terms of non-equilibrium Green's functions on the molecule alone, and equilibrium quantities (such as the Fermi-Dirac distribution) on the electrodes. The expression is given by

$$\mathcal{J}_L = \frac{ie}{\hbar} \int \frac{d\varepsilon}{2\pi} \mathrm{Tr} \left(\Gamma^L(\varepsilon) \left\{ \mathcal{G}^<(\varepsilon) + f_L(\varepsilon) \left[\mathcal{G}^r(\varepsilon) - \mathcal{G}^a(\varepsilon) \right] \right\} \right) \tag{2.11}$$

where both the trace and all matrix elements appearing in Eq. (2.11) now range over molecular indices only. $f_L(\varepsilon)$ is the Fermi distribution function for the electrons in the left electrode. $\left[\Gamma^L(\varepsilon)\right]_{nm} = 2\pi \sum_{\lambda \in L} h_{\lambda n} h^*_{\lambda m} \rho_\lambda(\varepsilon)$ represents the rate of loss of electrons on the molecule due to the coupling with the electrodes, and gives information on the "lifetime" of electrons resident on the molecule.

At equilibrium (which is valid for the electrodes) the density of states is related to the imaginary part of the single-particle Green's function

$$\rho_\lambda(\varepsilon) = \frac{1}{\pi} \mathrm{Im} \left[g^r_\lambda(\varepsilon) \right] \tag{2.12}$$

where $\rho_\lambda(\varepsilon)$ is the density of states for the left electrode. Correspondingly, $g^r(\varepsilon)$ is the unperturbed Green's function for the left electrode alone, which can be easily computed through a numerical renormalization group procedure as shown in the Appendix in detail. By defining the self-energy as $\left[\Sigma^r_L(\varepsilon)\right]_{nm} =$

$\sum_{\lambda\in L} h_{\lambda n} h^*_{\lambda m} g^r_\lambda(\varepsilon)$, Γ^L is then written as the imaginary part of $\Sigma^r_L(\varepsilon)$, given as,

$$\Gamma^L(\varepsilon) = \frac{1}{2}\left[\Sigma^r_L(\varepsilon) - \Sigma^a_L(\varepsilon)\right] \tag{2.13}$$

In steady state, the current is uniform everywhere, we have $\mathcal{J} = \mathcal{J}_L = -\mathcal{J}_R$. Thus, by writing the current formula in a more symmetric form, we have,

$$\begin{aligned}\mathcal{J} &= \frac{ie}{2\hbar}\int\frac{d\varepsilon}{2\pi}(\mathrm{Tr}\left\{\left[f_L(\varepsilon)\Gamma^L(\varepsilon) - f_R(\varepsilon)\Gamma^R(\varepsilon)\right]\left[\mathcal{G}^r(\varepsilon) - \mathcal{G}^a(\varepsilon)\right]\right\} \\ &+ \mathrm{Tr}\left\{\left[\Gamma^L(\varepsilon) - \Gamma^R(\varepsilon)\right]\mathcal{G}^<(\varepsilon)\right\})\end{aligned} \tag{2.14}$$

It is worth pointing out that, in Eq. (2.14) for the current, the first term in the integrand stands for the contribution to the current from the electrodes to the molecule, while the second term in the integrand stands for the contribution from the molecule to the electrodes. The result of Meir and Wingreen is formally exact for interacting systems coupled with non-interacting electrodes. Both the trace and matrix indices of the quantities appearing in Eq. (2.14) for the current range over the molecular indices only, while the coupling between the molecule and electrodes can be counted by the introduction of self-energies as we will show in the next section.

Under equilibrium conditions when $\mu_L = \mu_R$, we have $f_L = f_R = f_{eq}$. which gives $\mathcal{G}^<(\varepsilon) = -f_{eq}(\varepsilon)\left[\mathcal{G}^r(\varepsilon) - \mathcal{G}^a(\varepsilon)\right]$ and putting this back into Eq. (2.14), the current $\mathcal{J}$ thus vanishes under equilibrium conditions.

If we further neglect the electron-electron correlation in the molecular part, we have the identity (valid for non-correlated systems)

$$\mathcal{G}^<(\varepsilon) = i f_L(\varepsilon)\left[\mathcal{G}^r(\varepsilon)\Gamma^L(\varepsilon)\mathcal{G}^a(\varepsilon)\right] + i f_R(\varepsilon)\left[\mathcal{G}^r(\varepsilon)\Gamma^R(\varepsilon)\mathcal{G}^a(\varepsilon)\right] \tag{2.15}$$

and

$$\mathcal{G}^r(\varepsilon) = -\mathcal{G}^a(\varepsilon) = -i\mathcal{G}^r(\varepsilon)\left[\Gamma^L(\varepsilon) + \Gamma^R(\varepsilon)\right]\mathcal{G}^a(\varepsilon) \tag{2.16}$$

Then the current is given by,

$$\mathcal{J} = \frac{e}{h}\int d\varepsilon \left[f_L(\varepsilon) - f_R(\varepsilon)\right]\mathcal{T}(\varepsilon) \tag{2.17}$$

where $\mathcal{T}(\varepsilon) \equiv \mathrm{Tr}\left[\mathcal{G}^q(\varepsilon)\Gamma^R(\varepsilon)\mathcal{G}^r(\varepsilon)\Gamma^L(\varepsilon)\right]$ is just the transmission function, representing the probability of an electron transmitting from the left electrode to the right electrode at energy ε. This is just the Landauer formula derived in the previous chapter, demonstrating the equivalence of the Landauer formulation and the NEGF formulation for non-interacting systems.

In the linear response limit, when the bias voltage is infinitesimally small, we obtain the Landauer form of the differential conductance, given by,

$$G \equiv \frac{\partial \mathcal{J}}{\partial V} = 2\frac{e}{h}\int d\varepsilon \left[\frac{\partial f_L(\varepsilon)}{\partial V} - \frac{\partial f_R(\varepsilon)}{\partial V}\right]\mathcal{T}(\varepsilon) = 2\frac{e^2}{h}\mathcal{T}_{eq} = G_C \mathrm{Tr}\left\{t^\dagger t\right\} \tag{2.18}$$

In the linear response regime, conductance is nothing but the transmission function multiplied by the conductance quantum $G_C \equiv \frac{2e^2}{h}$, where 2 counts for the spins as we also obtained in the last chapter. While we have shown that Landauer expressions arise in the non-interacting limit of the exact NEGF expressions, the Landauer formula can be shown to be valid for interacting systems under other specific conditions at zero temperature [2, 3].

To summarize: the non-equilibrium Green's function formalism based on the Meir-Wingreen scheme provides an exact expression for the current in transport calculations when the electron-electron interaction is important in the molecular devices. The nice feature of the Meir-Wingreen scheme is that one only needs to focus on calculating Green's function matrix elements corresponding to the molecular part of the problem, not the entire molecule-electrode system. The modification due to the couplings between the semi-infinite electrodes and the molecule are treated as self-energies ($\Sigma_{L(R)}(\epsilon)$) which can be easily computed through a numerical renormalization group procedure.

2.3 Equation of motion Green's function technique

As shown in the previous section, to obtain the non-equilibrium current, one needs to have the Green's functions on the molecule. The simple approximation to obtain the Green's functions (as utilized in most transport calculations) is to treat the electron-electron interactions at a mean-field level. Then, all Green's functions take the form dictated by a non-interacting theory. Taking the retarded Green's function as an example, in the non-interacting picture, it is given by,

$$\mathcal{G}^r_{nm}(\varepsilon) = \left[\frac{1}{\varepsilon^+ - \mathcal{H}^{eff}_{mol}(\varepsilon^+) - \Sigma_L(\varepsilon^+) - \Sigma_R(\varepsilon^+)}\right]_{nm} \tag{2.19}$$

where n and m loop over indices of the molecular part $\mathcal{H}^{eff}_{mol}$ of the total Hamiltonian, which is effectively written in a single-particle framework such as is commonly used in density functional theory, and the couplings between the electrodes and molecule are added through the self-energies $\Sigma_{L(R)}(\varepsilon^+)$. $\varepsilon^+ \equiv \varepsilon + i\eta$, where η is an infinitesimally positive number that maintains the causality of the retarded Green's function.

The mean-field formulation of the NEGF formalism is easy to implement, and works pretty well in a lot of systems, and provides useful insights in understanding the electron transport process. But there are qualitative and quantitative limitations of such an approach. From a quantitative perspective, mean-field treatments of electron-electron interactions, such as through density functional theory, typically underestimate band gaps, and thus typically overestimate the conductance. Disagreements between theory and experiment are typically of several orders of magnitude [4]. These failures are in large part due to the wrong description of self-interaction in mean-field theories(see Appendix). It is still unclear how one can systematically improve density functional theory

to correct for such errors. From a qualitative perspective, mean-field treatments do not reproduce any of the more complicated conductance phenomena, such as the Kondo resonance, which depends on transport processes that involve the correlated motions of electrons.

Here we implement an alternative method that goes beyond mean-field theory to account for the electron-electron interactions in the electron transport process, based on the equation of motion Green's function technique that has been studied earlier [5, 6]. While earlier studies have typically relied on analytic approximations (and therefore, for example, have not been able to treat the finite bias regime), we employ the equation of motion technique in a computational setting in much the same way as the Landauer formula is currently applied. The basic idea of the equation of motion method is to setup a hierarchy of equations for the many-body Green's functions. By implementing a closure at a specific level of the hierarchical structure, we can get a closed set of equations with which we can solve for the Green's functions in a self-consistent way.

We start by applying the equation of motion to the retarded Green's function used in Eq. (2.19) but in the time domain. Other types of Green's functions follow a similar derivation.

The definition of retarded Green's function is given by,

$$\mathcal{G}^{r}_{A,B^{\dagger}}(t,t') \equiv -i\theta(t-t')\left\langle \left[A(t), B^{\dagger}(t')\right]_{+}\right\rangle \tag{2.20}$$

The time dependence of the retarded Green's function comes from two sources as shown in Eq. (2.20). The first place is in the Heaviside function, and the second place comes along with the operator $A(t)$. Applying the equation of

motion, we have,

$$
\begin{aligned}
i\frac{\partial}{\partial t}\mathcal{G}^r_{nm}(t-t') &= i\frac{\partial}{\partial t}\left[-i\theta(t-t')\right]\left\langle\left[c_n(t), c^\dagger_m(t')\right]_+\right\rangle \\
&+ \left[-i\theta(t-t')\right]\left\langle\left[i\frac{\partial}{\partial t}c_n(t), c^\dagger_m(t')\right]_+\right\rangle
\end{aligned} \tag{2.21}
$$

The first term is the time derivative of a Heaviside function, which is just a delta function. The second term involves the time derivative of a destruction operator on the molecule. By applying the equation of motion on this destruction operator, we have,

$$
i\frac{\partial}{\partial t}c_n(t) = \left[c_n(t), \mathcal{H}_{total}\right] \tag{2.22}
$$

$$
\left[c_n, \mathcal{H}_{total}\right] = \sum_\mu h_{n\mu}c_\mu + \sum_j h_{nj}c_j + \sum_{ijkl} h_{ijkl}\left[\delta_{in}c^\dagger_j c_l c_k - \delta_{jn}c^\dagger_i c_l c_k\right] \tag{2.23}
$$

Plugging Eq. (2.23) back into Eq. (2.21), we have,

$$
\begin{aligned}
i\frac{\partial}{\partial t}\mathcal{G}^r_{nm}(t-t') &= \delta(t-t')\delta_{nm} + \sum_\mu h_{n\mu}\mathcal{G}^r_{\mu m}(t-t') + \sum_j h_{nj}\mathcal{G}^r_{jm}(t-t') \\
&+ \sum_{ijkl} h_{ijkl}\left[\delta_{in}\mathcal{G}^r_{jlk;m}(t-t') - \delta_{jn}\mathcal{G}^r_{ilk;m}(t-t')\right]
\end{aligned} \tag{2.24}
$$

By applying the equation of motion, the retarded Green's function $\mathcal{G}^r_{nm}(t-t')$ is now coupled to the single-particle retarded Green's functions such as $\mathcal{G}^r_{\mu m}(t-t')$ connecting to the electrodes and $\mathcal{G}^r_{jm}(t-t')$ connecting to other sites within the molecular part and more importantly the two-particle retarded Green's function such as $\mathcal{G}^r_{jlk;m}(t-t')$.

To obtain a set of equations for the two-particle retarded Green's function $\mathcal{G}^r_{jlk;m}(t-t')$, we need to apply the equation of motion once again, just as we did for the single-particle retarded Green's function $\mathcal{G}^r_{nm}(t-t')$. Following this line, by applying the equation of motion multiple times, one can generate a hierarchy of coupled equations for the many-particle Green's functions. This provides a formally exact way for treating electron-electron correlation in the molecular

part. In practice, we truncate at a certain level, and stop applying the equation of motion further. Then in order to get a closed set of coupled equations for the many-particle Green's functions, we decompose the many-body Green's functions into products of several Green's functions which involve fewer bodies. In fact, it is sufficient to apply such decompositions to the strings of operators arising from the equation of motion of the destruction operator. For example, if we apply a decoupling procedure to the product of three operators appearing in Eq. (2.23),

$$c_j^\dagger c_l c_k \approx \langle c_j^\dagger c_l \rangle c_k - \langle c_j^\dagger c_k \rangle c_l \tag{2.25}$$

this corresponds to the approximation made in a normal mean-field theory. We

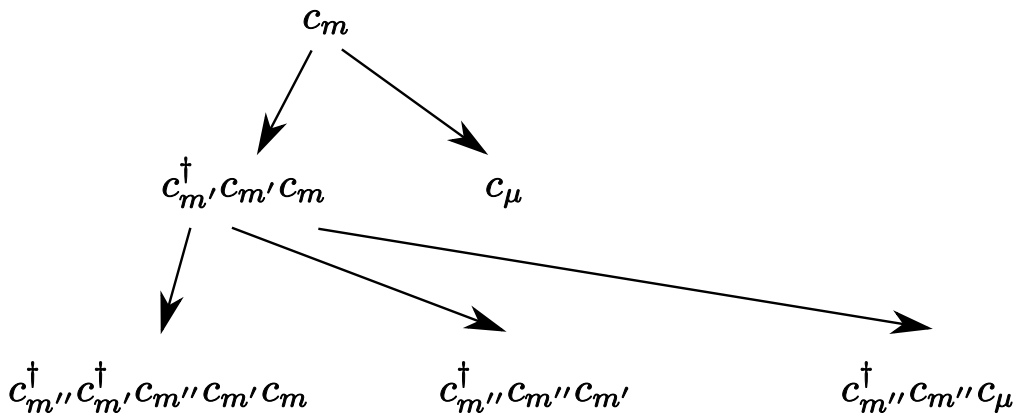

$$c^\dagger_{m''} c_{m''} c_\mu \approx \langle c^\dagger_{m''} c_{m''} \rangle c_\mu$$

Figure 2.3: Example for hierarchical structure generated by applying equation of motion to the destruction operator and derived terms. In order to get a closed set of coupled equations of motion for the many-body Green's functions, we can decompose combinations of operators into products as shown in the last equation.

will refer to this approximation as the first-order mean-field theory (MFT).

To go beyond the first-order mean-field approximation, instead of doing a

decomposition to $c_i^\dagger c_l c_k$ right after the first application of the equation of motion on c_n, we need to continue applying the equation of motion on $c_i^\dagger c_l c_k$. For the lack of better labels, we use the following indices to represent the molecular part of the total Hamiltonian.

$$H_{mol} = \sum_{mn\in M} h_{mn} c_m^\dagger c_n + \sum_{pqrs\in M} h_{pqrs} c_p^\dagger c_q^\dagger c_s c_r \tag{2.26}$$

Now applying the equation of motion, we have,

$$i\frac{\partial}{\partial t} c_i^\dagger c_l c_k = \left[c_i^\dagger c_l c_k, \mathcal{H}_{total}\right] \tag{2.27}$$

which gives,

$$\left[c_i^\dagger c_l c_k, \mathcal{H}_{elec}\right] = 0 \tag{2.28}$$

$$\begin{aligned}\left[c_i^\dagger c_l c_k, \mathcal{H}_{mol-elec}\right] &= \sum_{\mu\in L,R;m\in M} h_{\mu m}\left[c_i^\dagger c_l c_k, c_\mu^\dagger c_m\right] + \sum_{\mu\in L,R;m\in M} h_{m\mu}\left[c_i^\dagger c_l c_k, c_m^\dagger c_\mu\right] \\ &= \sum_{\mu\in L,R;m\in M} h_{\mu m}\left(-\delta_{mi} c_\mu^\dagger c_l c_k\right) + h_{m\mu}\left(\delta_{km} c_i^\dagger c_l c_\mu - \delta_{lm} c_i^\dagger c_k c_\mu\right)\end{aligned} \tag{2.29}$$

$$\begin{aligned}\left[c_i^\dagger c_l c_k, \mathcal{H}_{mol}\right] &= \sum_{mn\in M} h_{mn}\left[c_i^\dagger c_l c_k, c_m^\dagger c_n\right] + \sum_{pqrs\in M} h_{pqrs}\left[c_i^\dagger c_l c_k, c_p^\dagger c_q^\dagger c_s c_r\right] \\ &= \sum_{mn\in M} h_{mn}\left(\delta_{km} c_i^\dagger c_l c_n - \delta_{lm} c_i^\dagger c_k c_n - \delta_{im} c_m^\dagger c_l c_k\right) \\ &+ \sum_{pqrs\in M} h_{pqrs}[\left(\delta_{kp}\delta_{lq} - \delta_{kq}\delta_{lp}\right) c_i^\dagger c_s c_r + c_i^\dagger\left(\delta_{kq} c_p^\dagger - \delta_{kp} c_q^\dagger\right) c_l c_s c_r \\ &+ c_p^\dagger c_q^\dagger\left(\delta_{ir} c_s - \delta_{is} c_r\right) c_l c_k + c_i^\dagger\left(\delta_{lp} c_q^\dagger - \delta_{lq} c_p^\dagger\right) c_k c_s c_r]\end{aligned} \tag{2.30}$$

As shown in the last few terms in Eq. (2.30), applying the equation of motion to a product of three operators such as $c_i^\dagger c_l c_k$ will generate more complex terms such as products of five operators. Such terms are originated from the two-electron term in the molecular part of the total Hamiltonian. Now we apply the decoupling procedure to the product of five operators, taking the last term

$c_i^\dagger c_p^\dagger c_k c_s c_r$ in Eq. (2.30) for example,

$$\begin{aligned} c_i^\dagger c_p^\dagger c_k c_s c_r &\approx \langle c_p^\dagger c_k\rangle c_i^\dagger c_s c_r - \langle c_i^\dagger c_k\rangle c_p^\dagger c_s c_r \\ &+ \langle c_i^\dagger c_s\rangle c_p^\dagger c_k c_r - \langle c_p^\dagger c_s\rangle c_i^\dagger c_k c_r \\ &+ \langle c_p^\dagger c_r\rangle c_i^\dagger c_k c_s - \langle c_i^\dagger c_r\rangle c_p^\dagger c_k c_s \end{aligned} \tag{2.31}$$

from which we can construct a closure including only single-particle and two-particle Green's functions. Thus we have an approximation which we will call the second-order mean-field theory. In the following section, we will provide some calculations that illustrate the differences in the description of electron transport that occur when going from the first-order mean-field approximation to the second-order mean-field approximation.

2.4 Comparison between different levels of mean-field approximations

To study the electron-electron correlation effect on electron transport process, we now apply the equation of motion Green's function technique described above to some simple examples, and compare results using different levels of mean-field approximations.

We use the Hubbard model as shown in Eq. (2.32) for the molecular part of the total Hamiltonian in our calculations.

$$\mathcal{H}_{mol} = -\sum_{\langle ij\rangle}\left(h_{ij} + \delta_{ij}\epsilon_i\right)c_i^\dagger c_j + \sum_{i=1}^{N} U n_{i\uparrow} n_{i\downarrow} \tag{2.32}$$

where $\langle ij\rangle$ represents interaction between nearest neighbouring sites and ϵ_i represents the on-site energy on site i. We assume the on-site Coulomb repulsion

energy U is the same for all the sites in the molecule. $n_{i\uparrow(\downarrow)}$ represents the occupation number of electrons with up or down spin on site i, respectively.

Here are the parameters used in the transport calculations (in a.u.). For illus-

Table 2.1: Parameters for the Hubbard model connected to two non-interacting electrodes.

Parameters	Value	Description
ϵ_{elec}	-1.00	on-site energy for sites in electrodes
h_{elec}	-0.20	hopping energy for nearest neighbouring sites in electrodes
ϵ_{mol}	-1.00	on-site energy for sites in molecule
h_{mol}	-0.10	hopping energy for nearest neighbouring sites in molecule
$V_{mol,elec}$	-0.02	coupling between molecule and nearest neighbouring electrode sites
U_{mol}	-0.20	on-site Coulomb repulsion energy in molecule
μ_{eq}	-1.00	equilibrium chemical potential

tration purposes, the coupling amplitudes $V_{mol,elec}$ between molecule and neighbouring electrode sites are chosen to be small such that the broadening effect on the molecular spectral function due to the interaction with electrodes is small.

The first example we will look at is the one-site Hubbard model, which simply states that there is only one site for the molecule, connected to two semi-infinite electrodes, as shown in Fig. (2.4).

For the one-site Hubbard model, we can easily derive the Green's functions analytically. Taking the retarded Green's function as an example, the analytical

Figure 2.4: One-site Hubbard model connected to two non-interacting electrodes.

form is given by,

$$\mathcal{G}^r_{\sigma\sigma}(\epsilon) \approx \frac{1-\langle n_{\overline{\sigma}}\rangle}{\varepsilon-\varepsilon_\sigma-\Sigma^r_L-\Sigma^r_R}+\frac{\langle n_{\overline{\sigma}}\rangle}{\varepsilon-\varepsilon_\sigma-U-\Sigma^r_L-\Sigma^r_R} \tag{2.33}$$

where σ and $\overline{\sigma}$ stand for alpha and beta spins on the molecule site respectively, and ε_σ is the on-site energy for the molecule site. The retarded Green's function has two poles at ε_σ and $\varepsilon_\sigma+U$. The coupling with electrodes effectively broadens the width of the two poles via the self-energy terms $\Sigma^r_{L(R)}$.

In our numerical calculations, we show three calculations of the molecular Green's function with three different levels of approximations. In the first approximation we completely neglect any electron-electron interactions on the molecule (i.e. we set $U = 0$). In the second approximation, we use the normal mean-field theory (the first-order mean-field theory), and in the third we use the second-order mean-field theory. In Fig. (2.5), we show the spectral function of the molecule connected to the two electrodes, i.e., the imaginary part of the retarded Green's function. The red solid curve stands for the non-interacting result where U is set to 0. We see the position of the peak is at exactly ε_σ, in this case, -1.00. The green dashed line shows the result for the first-order mean-field approximation where U is set to 0.20, and the spectral function shows a single peak shifted as compared to the non-interacting calculation. Note that this is qualitatively incorrect, because the exact result predicts *two* peaks: the mean-field calculation is producing a single peak at the average location. The blue dashed line shows the result for the second-order mean-field approxima-

tion where U is also set to 0.20, and the spectrum shows a double-peak peak structure as expected in the analytical form of the retarded Green's function. The positions of the peaks are at -1.00 and -0.80 just as those predicted in the analytical solution.

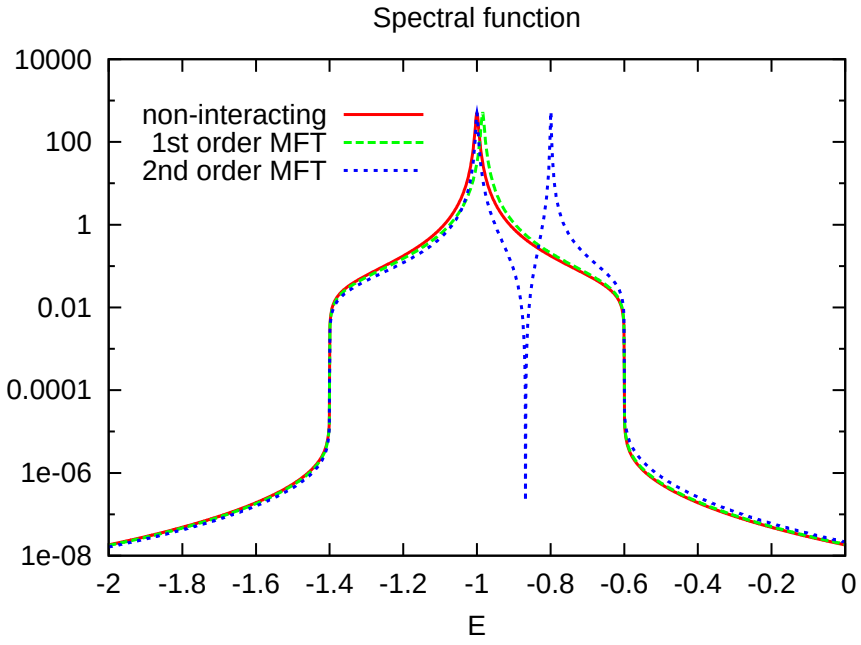

Figure 2.5: Spectral function for the one-site Hubbard model connected to two non-interacting electrodes.

We next show the current-voltage calculations for the three levels of approximations as shown in Fig. (2.6).

We see qualitative differences between different levels of approximations for calculating the current. The second-order mean-field approximation has more steps in the current-voltage plot as compared to either the one in the first-order mean-field approximation or the non-interacting calculations. Each of the steps in the second-order mean-field calculation corresponds correctly to a resonance in the spectral function. It is worth mentioning that, for the one-site Hubbard

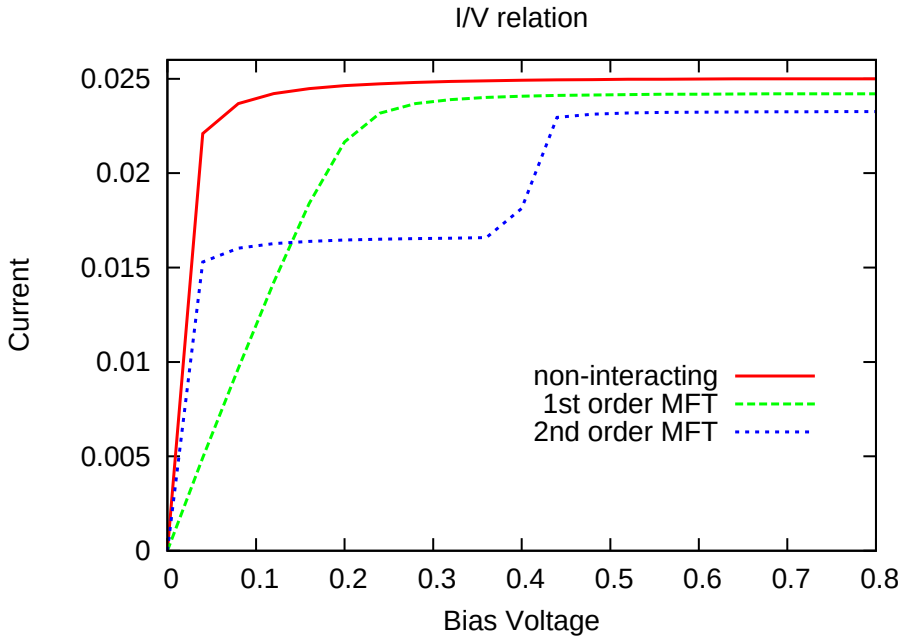

Figure 2.6: Current vs. voltage relation for the one-site Hubbard model connected to two non-interacting electrodes.

model under study, the second-order mean-field approximation is essentially exact since the two-body Green's functions are treated with no approximations at this level of truncation. We see that there are quite large differences in the current in the intermediate region between the two plateaus.

The second example we will now look at is the two-site Hubbard model as shown in Fig. (2.7).

Figure 2.7: Two-site Hubbard model connected to two non-interacting electrodes.

Similar to the one-site Hubbard model case, the spectral function in the second-order mean-field approximation reveals a more complex structure as

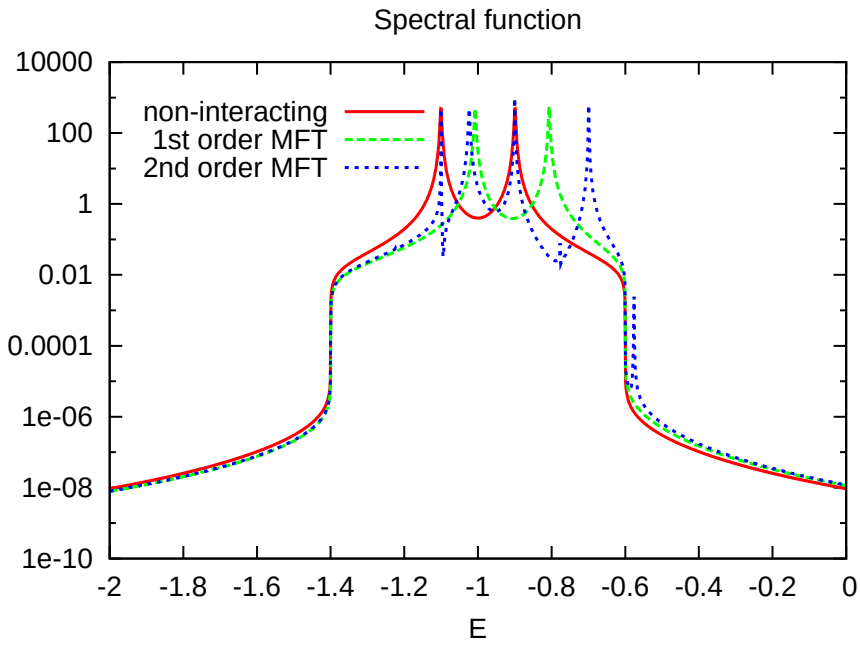

Figure 2.8: Spectral function for the two-site Hubbard model connected to two non-interacting electrodes.

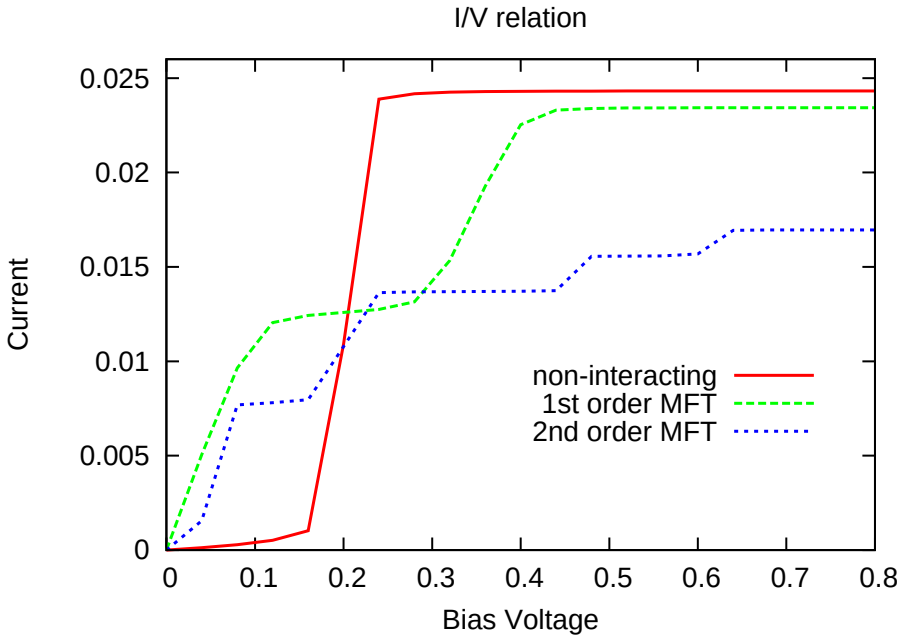

Figure 2.9: Current vs. voltage relation for the two-site Hubbard model connected to two non-interacting electrodes.

compared to the one using the first-order mean-field approximation. This is also reflected in the current calculations as shown in Fig. (2.9).

2.5 Conclusions

In this chapter, we introduced the non-equilibrium Green's function formalism used in electron transport calculations. The Meir-Wingreen scheme provides an exact expression for the current and conductance when electron-electron interaction is important in the molecular devices. To treat the electron-electron interactions, we derived a formally exact equation of motion Green's function technique which can be approximated in a systematic manner. By going to a second-order mean-field approximation, we see interesting features beyond the traditional mean-field approach, such as extra peaks in the spectral function and extra plateaus in the current-voltage curve. This is to be expected in the high-bias regime, where we are probing the the many-body nature of the excited states in the molecule.

BIBLIOGRAPHY

[1] C. Caroli, R. Combescot, P. Nozieres, and D. Saint-James. Direct Calculation of the Tunneling Current. *J. Phys. C: Solid St. Phys.*, 4:916, 1971.

[2] Y. Meir and N. S. Wingreen. Landauer Formula for the Current through an Interacting Electron Region. *Phys. Rev. Lett.*, 68:2512, 1992.

[3] A. Oguri. Fermi-Liquid Theory for a Condutance through an Interacting Region Attached to Noninteracting Leads. *J. Phys. Soc. Jpn.*, 66:1427, 1997.

[4] S. Quek, L. Venkataraman, H. J. Choi, S. G. Louie, M. S. Hybertsen, and J. B. Neaton. Amine-Gold Linked Single-Molecule Circuits: Experiment and Theory. *Nano Lett.*, 7:3477, 2007.

[5] C. Lacroix. Density of States for the Anderson Model. *J. Phys. F: Met. Phys.*, 11:2389, 1981.

[6] H. Haug and A.P. Jauho. *Quantum Kinetics in Transport and Optics of Semiconductors*. Springer, 1996.

CHAPTER 3

COULOMB BLOCKADE STUDY ON COBALT BIS(TERPYRIDYL) COMPLEX IN HARTREE-FOCK APPROXIMATION

3.1 Introduction and motivation

In the previous chapter, we explored how electron-electron interaction can give rise to qualitatively new features in the current-voltage (I-V) curve, e.g. new plateaus, which are not captured in conventional mean-field theory. This was to be expected, since we were probing conductance across a very wide bias range, where we access neutral excitations of the molecule which can have a correlated character. In the current chapter, we study the effect of electron-electron interactions on transport in a different regime, namely the *small* bias, weakly-coupling limit, under conditions of variable gate voltages. In the weakly-coupling limit, electrons traveling through the molecule are strongly localized in the molecular region. Due to the Coulomb repulsion from the localized electrons in the molecular region, other propagating electrons need more effort to transmit through the molecular region, resulting in an increased resistance at small bias voltages. This phenomena is called the Coulomb blockade effect. Transport in the Coulomb blockade limit probes the charged states rather than the neutral excitations of the molecule and is often described using mean-field theory. Exactly how mean-field theory achieves its description of the Coulomb blockade, (and in particular, the connection with the treatment of electron self-interaction) is what we will focus on in this study.

The main feature of transport in the Coulomb blockade regime is the occurrence of step-like features in the I-V curve as a function of gate voltage, which

correspond to successive integer charging events on the molecule. In Fig. (3.1), we show two different scenarios (corresponding to different bias voltages) in the Coulomb blockade regime where a molecular system is weakly coupled to the electrodes, so that we have an approximate chemical potential for the molecule even though it is an open system. Typical measurements are usually carried out at low temperatures, thus we assume that the Fermi-Dirac distribution function for the electrons in the electrodes takes the form of a Heaviside function.

In the left plot of Fig. (3.1), the chemical potential of the molecule does not lie in between the Fermi levels of the left and right electrodes, in such a configuration, the current is completely blocked. While in the right plot of Fig. (3.1), the chemical potential for a charged molecule lies in between the Fermi levels of the left and right electrodes, so the electron can flow from the left electrode, tunneling through the molecule and going to the right electrode.

The difference between the Coulomb blockade and the usual quantized conductance levels arising from quantization of the single particle levels is partly one of scales. In a mesoscopic device, for example, the spacing between the quantized levels can be quite small and yet rather large, uniformly spaced peaks are observed in the conductance as a function of gate voltage. This indicates the origin of the peaks is not simply due to the single particle level spacing. In a very small molecular device, where the single-particle level spacing is comparable to the Coulomb charging energy, the two processes of charge-transport are not so well separated. Nonetheless, the relatively straightforward nature of the phenomenon suggests that it can be understood using a simple theoretical approach.

In Fig. (3.2) we show a typical experimental measurement used to illustrate

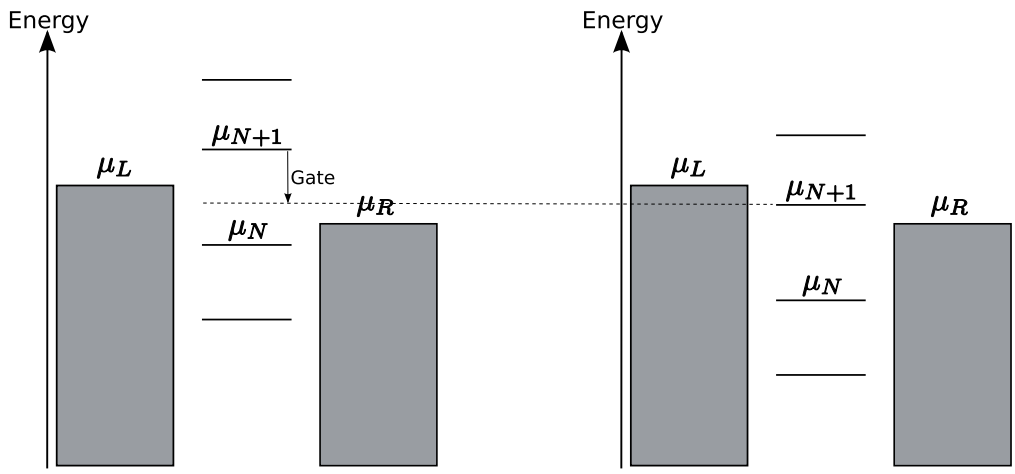

Figure 3.1: Schematic demonstration of the Coulomb blockade effect. Left plot: The chemical potential of the molecule does not lie in between the Fermi levels of the two electrodes. As a result, the current is blocked from the left electrode to the right electrode; Right plot: By applying a proper gate voltage, the chemical potential for a charged molecule is shifted in between the Fermi levels of the two electrodes. Thus, electron flows from the left electrode to the right electrode.

the Coulomb blockade, based on a cobalt bis(terpyridyl) complex of the type studied by Park *et al* [1]. This is known as a diamond plot, and is a plot of the differential conductance ($\partial I/\partial V$) as a function of gate and bias voltage. The bright linear lines correspond to the maximum of differential conductance when one of the Fermi levels of the electrodes aligns with the chemical potential of the molecule. The point where the two bright lines cross with each other is called the "degeneracy point" because the chemical potential of the charged molecule is degenerate with both the left and right electrodes as a result of a proper gate voltage. In principle, the magnitude of the gate voltage required to reach the degeneracy point is an indication that the energy scales involve Coulomb charging, although in practice it is hard to directly link the gate voltage applied in the measurement with the actual gate voltage experienced by the molecule.

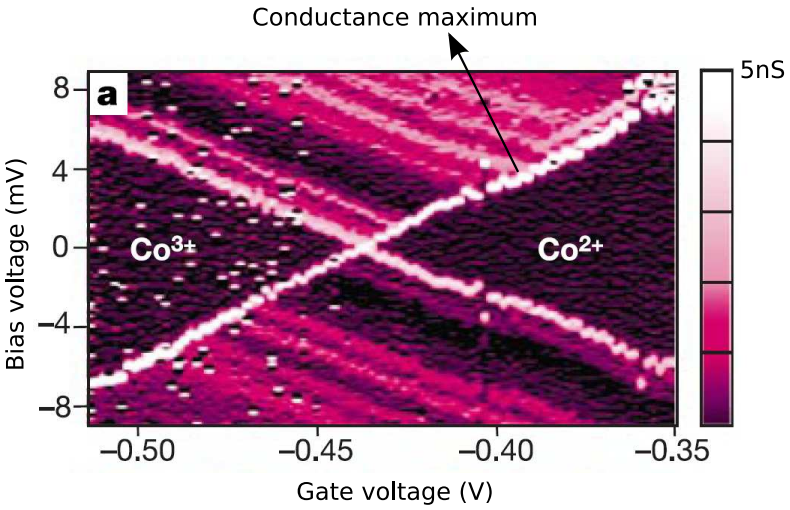

Figure 3.2: Differential conductance measurements under various gate and bias voltages.

3.2 Coulomb blockade in a cobalt bis(terpyridyl) complex

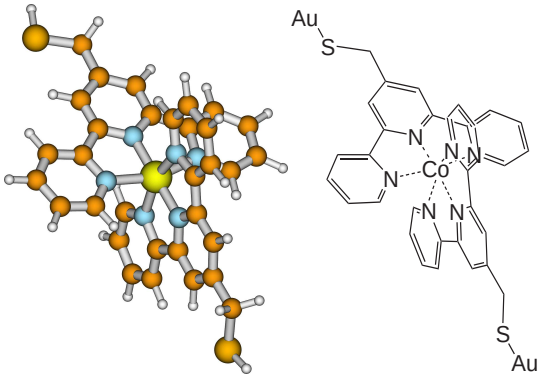

Figure 3.3: Cobalt bis(terpyridyl) complex. The Au (gold) terminating atoms in the left figure denote the beginning of the Au (gold) atomic chain electrodes.

3.2.1 Cobalt bis(terpyridyl) complex

Our model molecule is the cobalt bis(terpyridyl) complex $[Co(tpy - (CH_2)_2 - SH)_2]^{n+}$ shown in Fig. (3.3). Molecules of this kind with varying lengths of the thiol link-

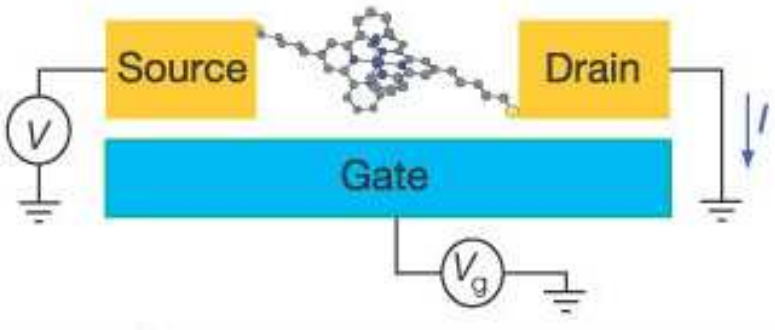

Figure 3.4: I-V measurements in cobalt bis(terpyridyl) complex (courtesy of the Abruña group).

ers have been studied experimentally by Park *et al* [1], as shown in Fig. (3.4). As we have discussed above, the Coulomb blockade refers to an increased resistance in a single-electron transistor under small bias voltages. From the electronic structure point of view, this is related to the localized electrons in the molecular devices, specifically, for our system, it is associated with the transition from the low-spin Co^{3+} formal oxidation state to the low-spin Co^{2+} formal oxidation state. In our calculations, the cobalt complex is attached via thiol linkages to atomic chain gold electrodes.

We carried out transport calculations using our own prototype non-equilibrium Green's function code. Our implementation is similar to that of Brandbyge *et al* [2] although we have used a finite cluster approximation to obtain the equilibrium part of the density matrix. For the cobalt complex, we used an *ab-initio* Hamiltonian in the STO-3G Gaussian basis [3]. The molecular geometry of the complex was optimized at the Hartree-Fock level. For the gold electrodes and the coupling matrix elements between the electrode and molecule basis functions, we used an Extended Hückel Hamiltonian [4] and the equilibrium chemical potential was chosen to be -10.0eV. An active-space of 16 orbitals was derived for the molecule from a restricted Hartree-Fock calculation

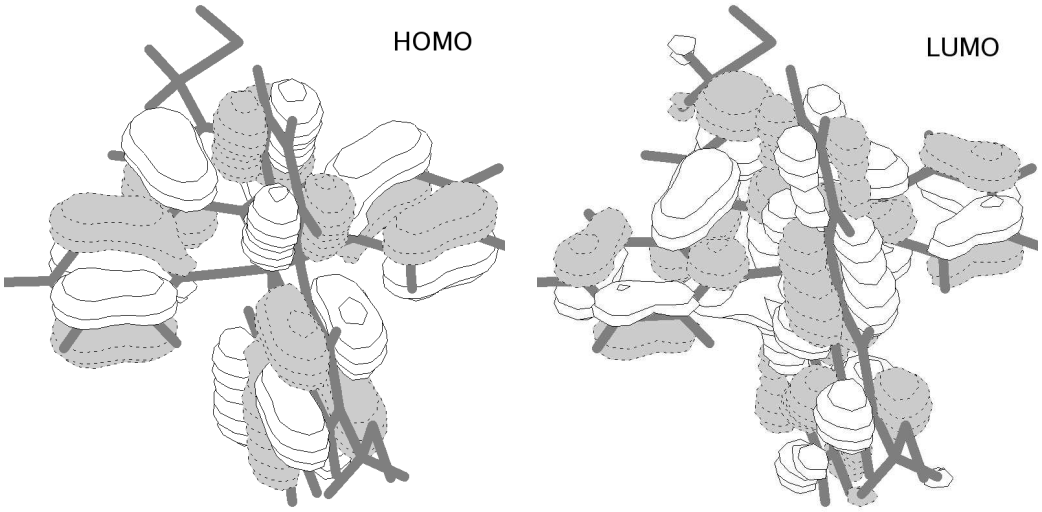

Figure 3.5: Cobalt complex molecular orbitals.

on the isolated (thiol-terminated) Co^{3+} complex. The orbitals were selected to be the 16 orbitals closest in energy to the HOMO and LUMO, excluding the sulfur non-bonding orbitals. (The sulfur non-bonding orbitals would be perturbed strongly on attachment to the gold electrodes to form bonding and anti-bonding orbitals that would lie outside our chosen active-space energy window). The resulting active-space orbitals were primarily π orbitals on the terpyridyl ligands (Fig. (3.5)). Both restricted (RHF) and unrestricted (UHF) Hartree-Fock calculations for the complete molecule-electrode system were performed using this same active-space representation for the molecule. In the transport calculations the bias voltage V was applied symmetrically as a chemical potential on the two electrodes ($\pm V/2$), while the gate voltage g was applied as a direct shift on the molecular active-space orbitals.

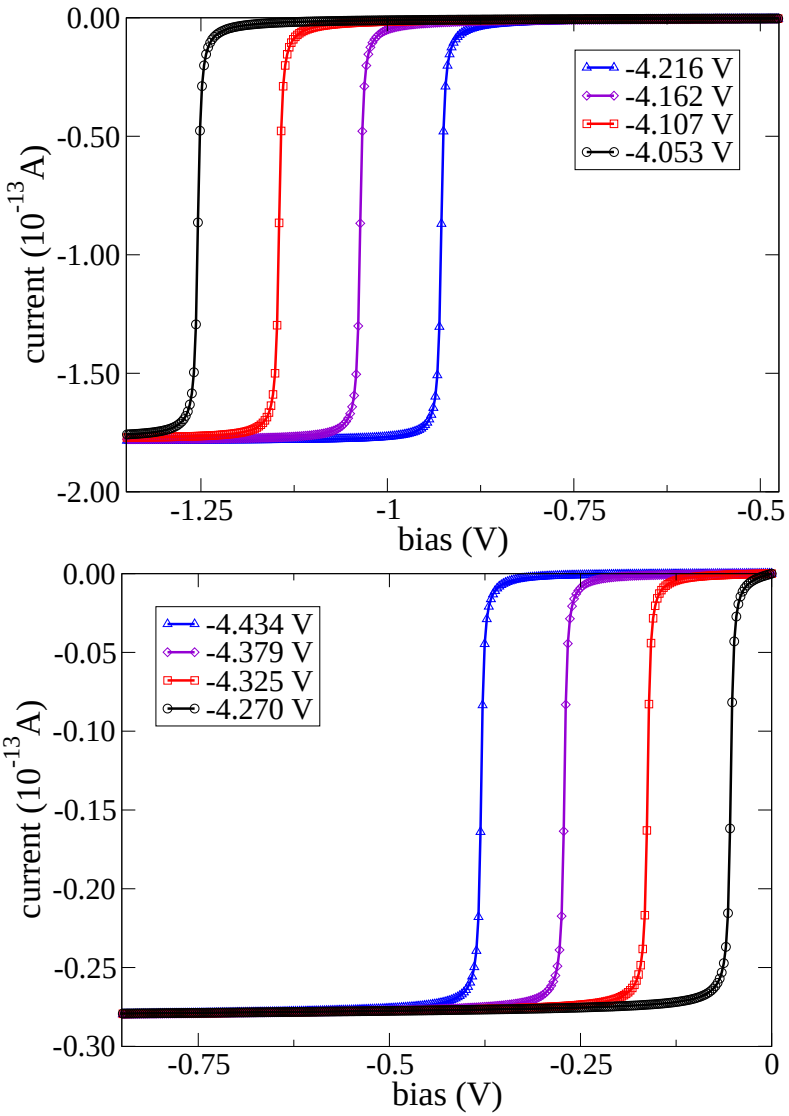

Figure 3.6: I-V curves at selected gate voltages.

3.2.2 Conductance and particle number as a function of gate and bias

The results of our Hartree-Fock NEGF transport calculations for the cobalt bis(terpyridyl) complex are shown in Figs. (3.6), (3.7), (3.8). Fig. (3.6) gives the current vs. bias (I-V) curves at selected gate voltages. Fig. (3.7) plots the

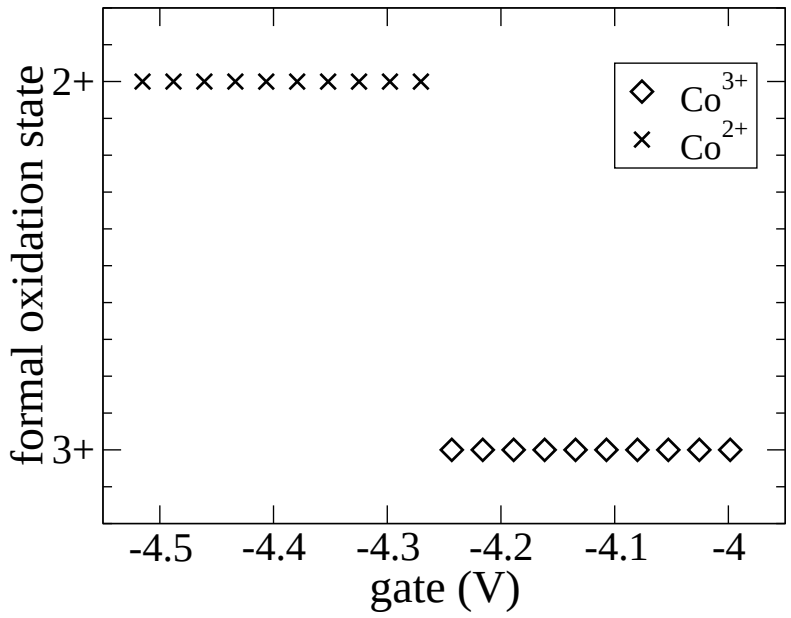

Figure 3.7: Formal oxidation state of the cobalt complex as a function of gate voltage.

oxidation state of the cobalt complex as a function of gate voltage at zero bias. (The oxidation state is evaluated from the occupation numbers of the orbitals which are primarily located on the complex; these are well localized because of the weak-coupling to the electrodes). Fig. (3.8) gives the diamond plot of the differential conductance $\partial I/\partial V$ as a function of gate voltage g and bias voltage V.

From these results we observe the following qualitative features:

- as the gate voltage (absolute value) increases, the molecule displays discrete integer charging (Fig. (3.7)),
- the maximum of the differential conductance peak shows a linear bias versus gate dependence (Fig. (3.6) and Fig. (3.8)),
- the linear dependence is interrupted by a discontinuity (Fig. (3.8)),

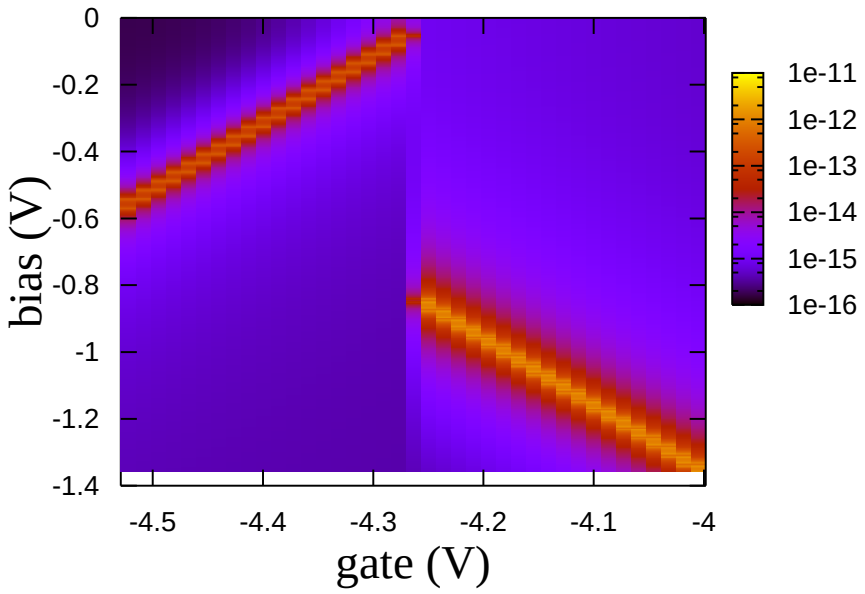

Figure 3.8: "Diamond" plot showing differential conductance as a function of gate and bias voltage. The discontinuity is an unphysical result arising from the mean-field spin-symmetry breaking. Brighter indicates larger conductance. The largest conductance is observed only for a very narrow range of values near the center of the bright bands.

- the maximum conductance in the Co^{2+} state is lower than in the Co^{3+} state (Fig. (3.6)).

Comparing with the experimental differential conductance plots in Park *et al* [1] shows that our theoretical plot is qualitatively similar, such as the discrete integer charging and the linear bias versus gate dependence, although the overall conductance maximum is smaller. Features (1) and (2) and possibly (4) appear to be in qualitative agreement with experiment, while (3) appears to be an artifact of the theoretical approximation.

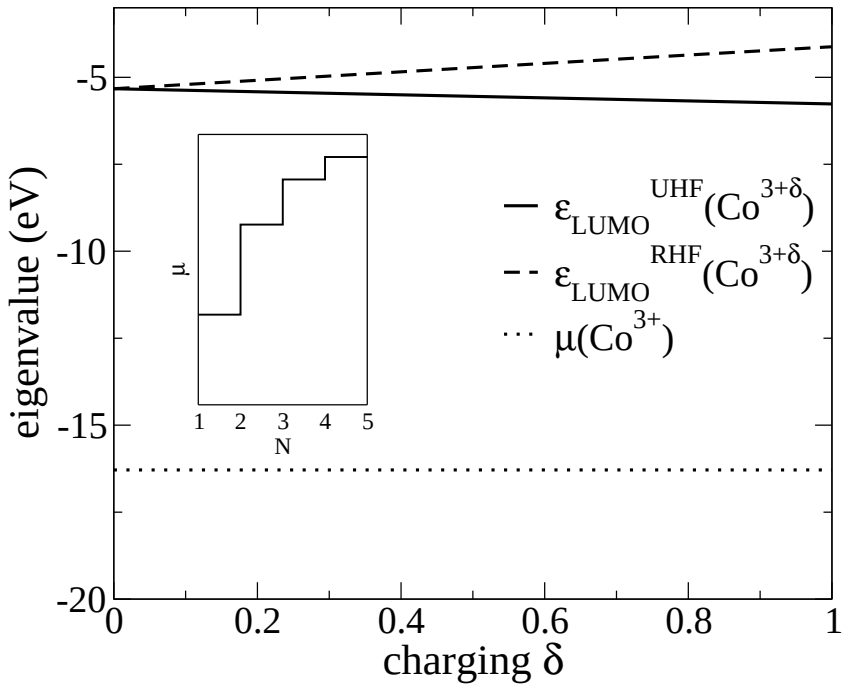

Figure 3.9: LUMO eigenvalue as a function of charging δ. As δ increases, the UHF LUMO eigenvalue decreases monotonically, while the RHF LUMO eigenvalue increases monotonically. The monotonic decrease of the UHF LUMO eigenvalue is what allows for the reproduction of integer charging in the Hartree-Fock theory of Coulomb blockade. Inset: Exact behaviour of the chemical potential μ as a function of the number of electrons.

Previous analysis of Coulomb blockade at the mean-field level (see e.g. Refs [5, 6]) has emphasized the appearance of spin-symmetry breaking in the mean-field theory and this explains many features of the Hartree-Fock conductance results. In the Co^{3+} system, the Hartree-Fock solution is restricted in nature, whereas in the Co^{2+} system it is unrestricted i.e. spin-symmetry breaking. The artifactual discontinuity in Fig. (3.8) arises because maximum conductance occurs when the LUMO or HOMO orbital eigenvalues are aligned with the biased levels of the electrode, i.e $\mu \pm V/2$, where μ is the chemical potential of the electrodes. The gate discontinuity is therefore the orbital energy difference $\epsilon^{RHF}_{LUMO}(Co^{3+}) - \epsilon^{UHF}_{HOMO}(Co^{2+})$. Similarly the decreased conductance in the Co^{2+}

state within the Hartree-Fock calculations is due to spin-symmetry breaking, as the unrestricted solution permits transport only through one of the two spin channels.

While the presence of qualitatively different restricted and unrestricted mean-field solutions on either side of a critical gate voltage permits a mean-field theory to emulate discrete jumps in particle number and conductance associated with Coulomb blockade charging, it does not fully explain the correct reproduction of features (1) and (2) in our results. For example, the molecule is formally an open system and the average particle number is a continuous variable. Thus while spin-symmetry breaking should produce a jump in particle number, it need not produce the correct *integer* jump as observed. Similarly it is not clear that a mean-field theory, where the eigenvalues have a non-linear dependence on density and charging, should produce a simple linear relationship between the maximum conductance gate voltage and bias. As one may expect, both these features result from the particular mean-field approximation used, i.e. Hartree-Fock theory, and are related to the absence of self-interaction error. The role of self-interaction in quantum transport has previously been discussed by several groups [7, 8, 9].

Let us first examine the discrete integer charging as a function of gate voltage, which is a hallmark of the Coulomb blockade. (We shall here assume zero bias and weak coupling). In an exact theory, discrete integer charging in an open system characterized by a chemical potential $\mu = \partial E/\partial N$ occurs because μ exhibits discontinuities at integer values of N and consists of straight line segments in between [9, 10, 11]. Consequently, for gate potential g, the molecule possesses integer charge N such that $I < \mu(N) < A$, where I and A are the ioniza-

tion energy and electron affinity of the molecule in the gate potential.

In a mean-field theory such as Hartree-Fock theory, the corresponding analysis requires examining the orbital eigenvalues as a function of charging in an open system. In a partially charged system such as the $Co^{3+\delta}$ complex the LUMO orbital is partially occupied yielding an ensemble one-particle density matrix

$$\gamma(Co^{3+\delta}) = \left(\sum_{i}^{HOMO} |\phi_i\rangle\langle\phi_i| \right) + \delta|\phi_{LUMO}\rangle\langle\phi_{LUMO}| \tag{3.1}$$

(Note that we have formally assigned the partial charge to the Co atom although in practice it is distributed also over the ligands). The chemical potential of the $Co^{3+\delta}$ complex is given then by the LUMO eigenvalue, $\mu(Co^{3+\delta}) = \epsilon_{LUMO}(Co^{3+\delta})$. Absence of partial charging implies that for any given μ, there are no lowest energy Hartree-Fock solutions with $\epsilon_{LUMO}(Co^{3+\delta}) \leq \mu$ for any value of δ other than 0 or 1. In Fig. (3.9) we have plotted the RHF and UHF LUMO eigenvalues $\epsilon_{LUMO}(Co^{3+\delta})$ of the isolated cobalt-complex (using the active space defined in section 3.2.1) as a function of the partial charging δ. Partial charging was enforced by occupying the LUMO with δ electrons and building the density matrix using Eq. (3.1).

For unrestricted Hartree-Fock theory we observe that $\epsilon_{LUMO}(Co^{3+\delta})$ decreases monotonically with δ. *The monotonic decrease of the LUMO is the key to integer charging*, as it ensures that as μ is raised from $\mu(Co^{3+})$ the first allowed charging event is an integer charging where $\mu = \epsilon^{UHF}_{LUMO}(Co^{2+})$. (Subsequently as μ is raised above $\epsilon^{UHF}_{LUMO}(Co^{2+})$, we could in principle deplete the LUMO orbital until $\epsilon^{UHF}_{LUMO}(Co^{2-\delta}) = \mu$; however this state would be higher in energy than the Hartree-Fock state with a completely filled LUMO, and thus would not be the lowest energy ensemble consistent with μ). In general the behaviour of the LUMO eigenvalue as a function of charging depends on the mean-field approx-

imation employed. In the UHF theory, the primary effect of the additional δ charge in the LUMO is to increase the Coulomb potential felt by the electrons in the lower lying orbitals. Within the LUMO however, the exchange interaction exactly cancels the electron self-interaction of the partial charge δ. In a frozen orbital Hartree-Fock approximation, the LUMO eigenvalue would therefore be independent of δ. Relaxation of the orbitals has a tendency to lower the LUMO eigenvalue, and this gives rise to the monotonic decrease of ϵ_{LUMO} with δ. (In the restricted Hartree-Fock theory, both the α and β LUMO orbitals become partially filled and interact via the Coulomb interaction, thus giving rise to the increase of the LUMO eigenvalue with δ).

The exact cancellation of self-interaction in the LUMO is a feature of unrestricted Hartree-Fock theory which does not generally occur in other unrestricted mean-field approximations, such as certain density functionals. These may therefore give rise to erroneous partial-charging in the Coulomb blockade regime as a function of gate voltage. An analogous partial charging occurs in the approximate density functional description of infinitely dissociated fragments [10, 11], and within transport calculations, is related to erroneous predictions of metallic transport in insulating molecules [9].

The observed physical linear behaviour of the maximum conductance bias as a function of gate within the Hartree-Fock approximation is closely linked to the faithful reproduction of integer charging. Although a non-linear mean-field theory could in principle produce a non-linear behaviour of the eigenvalues with gate in the weakly-coupled limit, this would require some form of charging which is here disallowed, except for integer charging. Thus the effect of the constant gate voltage g is simply to shift the orbital eigenvalues by g, which

immediately yields the linear relationship between g and the maximum conductance bias. When integer charging does occur, the subsequent discontinuity in the maximum conductance peak may be viewed in this context as an *extremely* non-linear behaviour of the eigenvalue arising from the mean-field nature of the theory.

3.3 Conclusions

To shortly summarize, here we have studied the transport characteristics of a cobalt bis(terpyridyl) complex in the Coulomb blockade regime using *ab-initio* Hartree-Fock theory combined with the NEGF formalism. We find that we can qualitatively reproduce the main features of the Coulomb blockade. While this is in part explained by the spin-symmetry breaking in the theory, we have shown that ultimately it is the correct description of electron self-interaction in Hartree-Fock theory that is directly responsible for the reproduction of important Coulomb blockade features such as integer charging, and linear dependence of maximum conductance bias on gate. As a corollary, mean-field density functionals (which do not usually correctly describe electron self-interaction) will not be expected to capture these basic features correctly.

BIBLIOGRAPHY

[1] J. Park, A. N. Pasupathy, J. I. Goldsmith, C. Chang, Y. Yaish, J. R. Petta, M. Rinkoski, J. P. Sethna, H. D. Abruña, P. L. McEuen, and D. C. Ralph. Coulomb Blockade and the Kondo Effect in Single-Atom Transistors. *Nature*, 417:722, 2002.

[2] M. Brandbyge, J. L. Mozos, P. Ordejón, J. Taylor, and K. Stokbro. Density-Functional Method for Nonequilibrium Electron Transport. *Phys. Rev. B*, 65:165401, 2002.

[3] M. J. Frisch, G. W. Trucks, H. B. Schlegel, G. E. Scuseria, M. A. Robb, J. R. Cheeseman, J. A. Montgomery, Jr., T. Vreven, K. N. Kudin, J. C. Burant, J. M. Millam, S. S. Iyengar, J. Tomasi, V. Barone, B. Mennucci, M. Cossi, G. Scalmani, N. Rega, G. A. Petersson, H. Nakatsuji, M. Hada, M. Ehara, K. Toyota, R. Fukuda, J. Hasegawa, M. Ishida, T. Nakajima, Y. Honda, O. Kitao, H. Nakai, M. Klene, X. Li, J. E. Knox, H. P. Hratchian, J. B. Cross, C. Adamo, J. Jaramillo, R. Gomperts, R. E. Stratmann, O. Yazyev, A. J. Austin, R. Cammi, C. Pomelli, J. W. Ochterski, P. Y. Ayala, K. Morokuma, G. A. Voth, P. Salvador, J. J. Dannenberg, V. G. Zakrzewski, S. Dapprich, A. D. Daniels, M. C. Strain, O. Farkas, D. K. Malick, A. D. Rabuck, K. Raghavachari, J. B. Foresman, J. V. Ortiz, Q. Cui, A. G. Baboul, S. Clifford, J. Cioslowski, B. B. Stefanov, G. Liu, A. Liashenko, P. Piskorz, I. Komaromi, R. L. Martin, D. J. Fox, T. Keith, M. A. Al-Laham, C. Y. Peng, A. Nanayakkara, M. Challacombe, P. M. W. Gill, B. Johnson, W. Chen, M. W. Wong, C. Gonzalez, and J. A. Pople. GAUSSIAN 03, REVISION C.02, Gaussian, Inc., Wallingford CT, 2004. see http://www.gaussian.com/.

[4] G. A. Landrum and W. V. Glassey. BIND(VER. 3.0) is distributed as part of the YAeHMOP extended Hückel molecular orbital package. see http://yaehmop.sourceforge.net/.

[5] B. Muralidharan, A. W. Ghosh, and S. Datta. Probing Electronic Excitations in Molecular Conduction. *Phys. Rev. B*, 73:155410, 2006.

[6] J. J. Palacios. Coulomb Blockade in Electron Transport through a C_{60} Molecule from First Principles. *Phys. Rev. B*, 72:125424, 2005.

[7] P. Mori-Sánchez, A. J. Cohen, and W. Yang. Many-Electron Self-Interaction Error in Approximate Density Functionals. *J. Chem. Phys.*, 125:201102, 2006.

[8] S. Ke, H. U. Baranger, and W. Yang. Role of the Exchange-Correlation

Potential in Ab Initio Electron Transport Calculations. *J. Chem. Phys.*, 126:201102, 2007.

[9] C. Toher, A. Filippetti, S. Sanvito, and K. Burke. Self-Interaction Errors in Density-Functional Calculations of Electronic Transport. *Phys. Rev. Lett.*, 95:146402, 2005.

[10] R. Parr and W. Yang. *Density-Functional Theory of Atoms and Molecules*. Oxford University Press, 1989.

[11] J. P. Perdew, R. G. Parr, M. Levy, and J. L. Balduz, Jr. Density-Functional Theory for Fractional Particle Number: Derivative Discontinuities of the Energy. *Phys. Rev. Lett.*, 49:1691, 1982.

CHAPTER 4

ELECTRON SCATTERING IN GRAPHENE NANORIBBONS

4.1 Introduction and motivation

Recently in 2004, Novoselov and Geim *et al* [1], using mechanical exfoliation (repeated peeling) method, have successfully prepared a single layer of carbon atoms, graphene, up to the size of a few micrometers. This material appears to be relatively low in defects and essentially two-dimensional. Ever since then, there has been much research on graphene from both theoretical and experimental sides due to the possible applicability as an electronic material.

In graphene, the carbon atoms are arranged in a honeycomb lattice in two dimensions as shown in Fig. (4.1), with a separation of $a = 1.42$Å between nearest neighbouring carbon atoms.

The lattice structure of graphene does not fall into any category of the Bravais lattices. Instead it can be viewed as a triangular lattice with two carbon atoms per unit cell as shown in Fig. (4.1). Each atom in the unit cell forms a sublattice. Around each atom, there are three neighbouring atoms of the other sublattice. Here we use sublattice A and sublattice B to distinguish between them. The lattice vectors can be written as:

$$\vec{a}_1 = \left(\frac{3a}{2}, \frac{\sqrt{3}a}{2}\right), \vec{a}_2 = \left(\frac{3a}{2}, -\frac{\sqrt{3}a}{2}\right) \tag{4.1}$$

and the three nearest neighbouring vectors around a carbon atom are,

$$\vec{\delta}_1 = \left(\frac{a}{2}, \frac{\sqrt{3}a}{2}\right), \vec{\delta}_2 = \left(\frac{a}{2}, -\frac{\sqrt{3}a}{2}\right), \vec{\delta}_3 = (-a, 0) \tag{4.2}$$

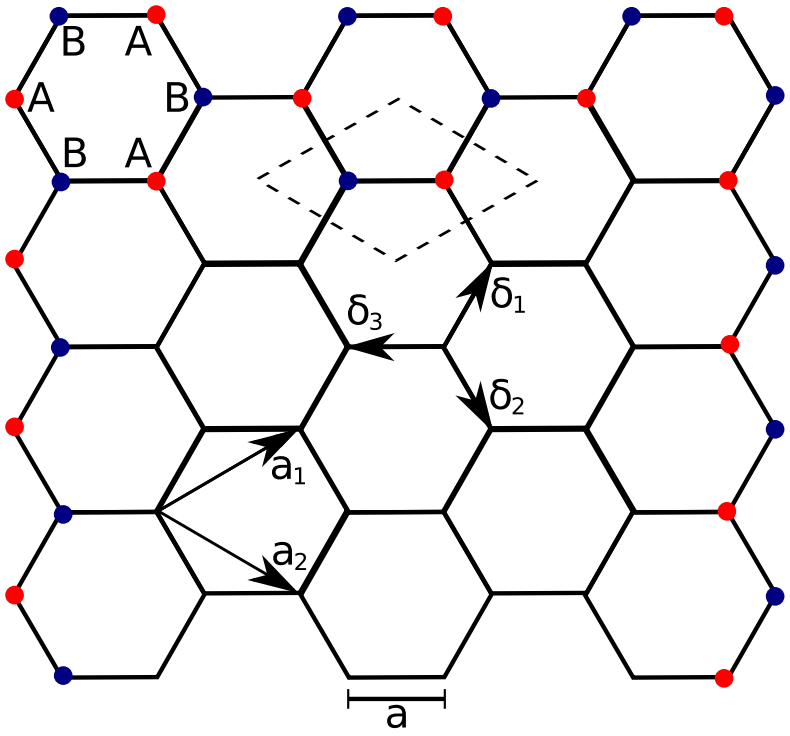

Figure 4.1: Graphene lattice. Within a unit cell (dashed diamond), there are two carbon atoms separated by a distance of $a = 1.42$Å. Each atom forms a sublattice. We use red dots to represent the atoms in sublattice A, and blue dots in sublattice B. Next to one carbon atom, there are three carbon atoms from the opposite sublattice, connected by three nearest neighbouring vectors $\vec{\delta}_{1,2,3}$.

What makes graphene unusual from a fundamental point of view is its unique electronic band structure. Graphene is a semi-metal which means that the band gap vanishes, but only at certain special points on the Fermi surface. Near those points, there is a linear dispersion relation (i.e. linear dependence of the orbital energy on wavevector modulus). This dispersion relation resembles that of a free relativistic massless particle or Dirac fermion, with an effectively modified (larger) fine-structure constant and (reduced) speed of light. Thus many effects (such as the Klein paradox) that occur in relativistic systems can effectively be studied in the framework of graphene electrons near the Fermi

surface.

In the current chapter, we first derive the semi-metallic band structure of graphene and then relate it to the effective massless Dirac fermion model. We then proceed to a study of transport in graphene nanoribbons, the main topic of the chapter. Graphene samples typically contain impurities of various kinds, and it is not yet known how they affect the electron transport. The influence of charged impurities, in particular, is controversial. The aim of our study is to understand the effects of different types of scatterers in graphene, both from a numerical Landauer perspective and from the perspective of Dirac fermions. We then look at how we can use some unusual features of relativistic scattering to control transport through graphene nanoribbons.

4.2 Electronic band structure of graphene

In graphene, the $2s$, $2p_x$ and $2p_y$ orbitals from the carbon atoms hybridize into three sp^2 orbitals, that lie in the planar carbon framework, forming three σ bands. The σ bands are low-lying bands that stabilize the graphene framework. The $2p_z$ orbitals are perpendicular to the planar sheet, forming a π band. In neutral graphene, each of the $2p_z$ orbitals has an extra electron which gives rise to a half-filled π band. As a result, only the electrons in the π bands are relevant for the transport properties. To start with, we shall investigate the electronic band structure of graphene in the tight-binding limit.

In periodic systems such as that of graphene, due to the translational symmetry of the unit cells in the directions of the lattice vectors a_i ($i = 1, 2$), the eigen-

functions satisfy the Bloch's theorem, that is,

$$T_{\vec{a}_i}\Psi = e^{i\vec{k}\cdot\vec{a}_i}\Psi \qquad (i = 1, 2) \tag{4.3}$$

where $T_{\vec{a}_i}$ is the translational operator along the lattice vector $\vec{a}_i$, and $\vec{k}$ is the wavevector.

To find the eigenfunctions that satisfy the Bloch equation as shown in Eq. (4.3), we start with a set of the atomic orbitals that are localized around the atoms, although one could in principle use any kind of orbitals, for example plane-wave orbitals that are commonly used in solid state physics studies. For general purposes, we would assume that for each unit cell we have n such orbitals. A functional form which satisfies Eq. (4.3) is based on the n atomic orbitals in the unit cell (for graphene lattice, $n = 2$) can be written as,

$$\Phi_j\left(\vec{k}, \vec{r}\right) = \frac{1}{\sqrt{N}} \sum_{\vec{R}}^{N} e^{i\vec{k}\cdot\vec{R}} \varphi_j\left(\vec{r} - \vec{R}\right), (j = 1, \ldots, n) \tag{4.4}$$

where N is the number of atoms in the system, $\vec{R}$ is the position of the atom and φ_j is the jth atomic orbital. For a given wavevector $\vec{k}$, we have n such Bloch functions. Just for illustration purposes, one can prove that Φ_j does satisfy the Bloch's theorem.

$$\begin{aligned}
\Phi_j\left(\vec{k}, \vec{r} + \vec{a}\right) &= \frac{1}{\sqrt{N}} \sum_{\vec{R}}^{N} e^{i\vec{k}\cdot\vec{R}} \varphi_j\left(\vec{r} + \vec{a} - \vec{R}\right) \\
&= e^{i\vec{k}\cdot\vec{a}} \frac{1}{\sqrt{N}} \sum_{\vec{R}-\vec{a}}^{N} e^{i\vec{k}\cdot\left(\vec{R}-\vec{a}\right)} \varphi_j\left(\vec{r} - \left(\vec{R} - \vec{a}\right)\right) \\
&= e^{i\vec{k}\cdot\vec{a}} \Phi_j\left(\vec{k}, \vec{r}\right)
\end{aligned} \tag{4.5}$$

One can think of the Bloch functions Φ_j as the counterpart of the symmetry adapted orbitals in the normal quantum chemistry language. To construct a "symmetry orbital" $\Phi_j\left(\vec{k}, \vec{r}\right)$, one needs a linear combination of the atomic or-

bitals $\varphi_j\left(\vec{k}, \vec{r}-\vec{R}\right)$ with the "coefficients" $e^{i\vec{k}\cdot\vec{R}}$, where $\vec{R}$ loops over all the atomic orbitals of the same type in the $N\left(\sim 10^{23}\right)$ unit cells of the solid.

To calculate the energy spectrum of the system, we first construct a set of functions Ψ_i from the linear combinations of symmetry adapted basis functions Φ_j.

$$\Psi_i\left(\vec{k}, \vec{r}\right) = \sum_{j=1}^{n} C_{ij}\left(\vec{k}\right)\Phi_j\left(\vec{k}, \vec{r}\right) \tag{4.6}$$

Following the linear property of Ψ_i as shown in Eq. (4.6), it is easy to prove that Ψ_i also satisfies the Bloch theorem.

The energy of the system can be evaluated variationally by,

$$E_i\left(\vec{k}\right) = \frac{\langle\Psi_i|\mathcal{H}|\Psi_i\rangle}{\langle\Psi_i|\Psi_i\rangle} \tag{4.7}$$

where $\mathcal{H}$ is the Hamiltonian for the system. Substituting Eq. (4.6) into Eq. (4.7), we have,

$$\begin{aligned} E_i\left(\vec{k}\right) &= \frac{\sum_{j,j'=1}^{n} C_{ij}^* C_{ij'}\langle\Phi_j|\mathcal{H}|\Phi_{j'}\rangle}{\sum_{j,j'=1}^{n} C_{ij}^* C_{ij'}\langle\Phi_j|\Phi_{j'}\rangle} \\ &= \frac{\sum_{j,j'=1}^{n} \mathcal{H}_{jj'}\left(\vec{k}\right) C_{ij}^* C_{ij'}}{\sum_{j,j'=1}^{n} \mathcal{S}_{jj'}\left(\vec{k}\right) C_{ij}^* C_{ij'}} \end{aligned} \tag{4.8}$$

where both

$$\mathcal{H}_{jj'} = \langle\Phi_j|\mathcal{H}|\Phi_{j'}\rangle \tag{4.9}$$

and

$$\mathcal{S}_{jj'} = \langle\Phi_j|\mathcal{S}|\Phi_{j'}\rangle \tag{4.10}$$

are $n \times n$-dimension matrices.

In the following, we will assume the overlap matrix $\mathcal{S}$ is the identity matrix for simplicity. Now we will examine how the Hamiltonian $\mathcal{H}$ looks like in graphene.

In graphene π bands, each atom contributes one p_z orbital. Thus here $n = 2$, as within each unit cell, there are two carbon atoms.

$$\mathcal{H} = \begin{bmatrix} \mathcal{H}_{AA} & \mathcal{H}_{AB} \\ \mathcal{H}_{BA} & \mathcal{H}_{BB} \end{bmatrix} \tag{4.11}$$

with

$$\mathcal{H}_{AA} = \langle \Phi_A | \mathcal{H} | \Phi_A \rangle \tag{4.12}$$

and $\mathcal{H}_{AB}$, $\mathcal{H}_{BA}$, $\mathcal{H}_{BB}$ are similarly defined. Further simplifying the equation above, we have,

$$\mathcal{H} = \begin{bmatrix} \epsilon_{2p} & t f\left(\vec{k}\right) \\ t f^*\left(\vec{k}\right) & \epsilon_{2p} \end{bmatrix} \tag{4.13}$$

where ϵ_{2p} is the atomic on-site energy of carbon $2p_z$ orbital. t is the hopping integral between nearest neighbouring carbon atoms. $f\left(\vec{k}\right) \equiv e^{i\vec{k}\cdot\vec{\delta_1}} + e^{i\vec{k}\cdot\vec{\delta_2}} + e^{i\vec{k}\cdot\vec{\delta_3}}$, and $\vec{\delta}_1, \vec{\delta}_2$ and $\vec{\delta}_3$ are the three nearest neighbouring vectors as shown in Fig. (4.1).

We can adjust ϵ_{2p} to 0 for convenience. Then by diagonalizing $\mathcal{H}$, we find the spectrum to be,

$$\begin{aligned} E\left(\vec{k}\right) &= \pm t \sqrt{\left| f\left(\vec{k}\right) \right|^2} = \pm t \sqrt{\left| e^{i\vec{k}\cdot\vec{\delta_1}} + e^{i\vec{k}\cdot\vec{\delta_2}} + e^{i\vec{k}\cdot\vec{\delta_3}} \right|^2} \\ &= \pm t \sqrt{1 + 4\cos\left(\frac{3a}{2}k_x\right)\cos\left(\frac{\sqrt{3}a}{2}k_y\right) + 4\cos^2\left(\frac{\sqrt{3}a}{2}k_y\right)} \end{aligned} \tag{4.14}$$

Here we show the graphene band structure in the left plot of Fig. (4.2). From Eq. (4.14), the conduction band touches the valence band at six $\vec{K}$ points in the first Brillouin zone, where $f\left(\vec{k}\right) = 0$.

Solving for k, we have,

$$\vec{K} = \left(\frac{2\pi}{3a}, \frac{2\pi}{3\sqrt{3}a}\right), \qquad \vec{K}' = \left(\frac{2\pi}{3a}, -\frac{2\pi}{3\sqrt{3}a}\right) \tag{4.15}$$

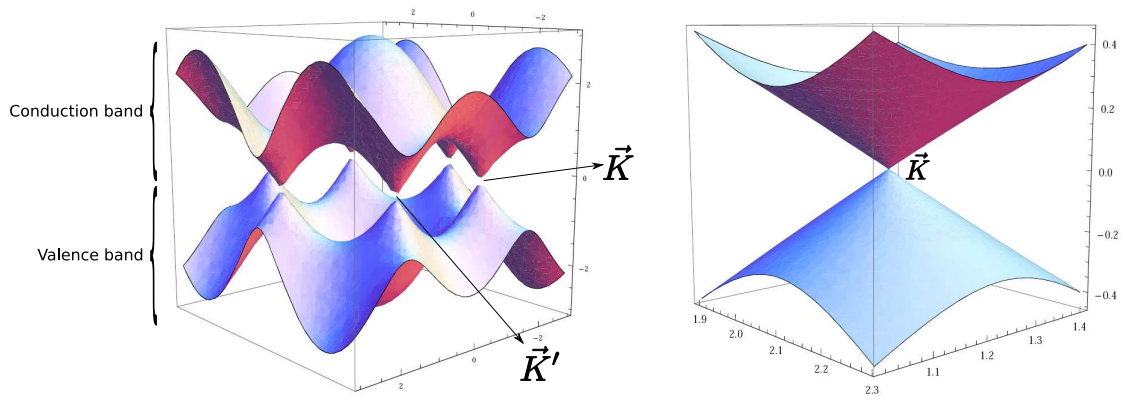

Figure 4.2: Graphene band structure (left) and linear dispersion (right) near the Dirac point.

with the other four equivalent points at the corner of the first Brillouin zone. Around each of these six $\vec{K}$ points, we see the linear dispersion relation as shown in the right plot of Fig. (4.2). This linear dispersion relation allows us to construct an effective low-energy theory to model the electrons near the Fermi surface as massless Dirac fermions.

Dirac fermions in effective mass approximation

In the low energy regime (energy close to ϵ_{2p}, which is set to 0), the electronic wavelength is much larger than the graphene lattice constant $\sqrt{3}a$, so that we can take the limit of $a \to 0$, and write down a continuum equation. At low-energies, one has to be near the $\vec{K}$ points. Consequently, we can do a Taylor expansion of the off-diagonal coupling elements $f\left(\vec{k}\right)$ around the $\vec{K}$ points as $\vec{k} = \vec{K} + \vec{q}$ with, for example, $\vec{K} = \left(\frac{2\pi}{3a}, \frac{2\pi}{3\sqrt{3}a}\right)$, and neglect the higher order terms of $\vec{q} = \left(q_x, q_y\right)$.

$$\begin{aligned} f\left(\vec{k}\right) &= f\left(\vec{K} + \vec{q}\right) \\ &= e^{i\vec{K}\cdot\vec{\delta_1}} e^{i\vec{q}\cdot\vec{\delta_1}} + e^{i\vec{K}\cdot\vec{\delta_2}} e^{i\vec{q}\cdot\vec{\delta_2}} + e^{i\vec{K}\cdot\vec{\delta_3}} e^{i\vec{q}\cdot\vec{\delta_3}} \end{aligned}$$

$$
\begin{aligned}
&= e^{i\vec{K}\cdot\vec{\delta_1}}\left(1+i\vec{q}\cdot\vec{\delta_1}\right)+e^{i\vec{K}\cdot\vec{\delta_2}}\left(1+i\vec{q}\cdot\vec{\delta_2}\right)+e^{i\vec{K}\cdot\vec{\delta_3}}\left(1+i\vec{q}\cdot\vec{\delta_3}\right)\\
&= \left(e^{i\vec{K}\cdot\vec{\delta_1}}+e^{i\vec{K}\cdot\vec{\delta_2}}+e^{i\vec{K}\cdot\vec{\delta_3}}\right)+i\left(e^{i\vec{K}\cdot\vec{\delta_1}}\vec{q}\cdot\vec{\delta_1}+e^{i\vec{K}\cdot\vec{\delta_2}}\vec{q}\cdot\vec{\delta_2}+e^{i\vec{K}\cdot\vec{\delta_3}}\vec{q}\cdot\vec{\delta_3}\right)\\
&= \frac{3a}{2}\left(q_x-iq_y\right)e^{i\frac{5\pi}{6}} \qquad (4.16)
\end{aligned}
$$

It can be easily shown that neglecting $e^{i\frac{5\pi}{6}}$ and $e^{-i\frac{5\pi}{6}}$ in the off-diagonal terms only changes the phase of the eigenfunction, so in the following we will simply neglect these phase terms.

The Hamiltonian then can be written in the form of the Dirac equation similar to that of massless fermions studied in high energy physics. The $\vec{K}$ points at which the band gap goes to zero are the so-called Dirac points for this reason.

$$
H\left(\vec{q}\right)=\begin{bmatrix} 0 & \frac{3at}{2}\left(q_x-iq_y\right) \\ \frac{3at}{2}\left(q_x+iq_y\right) & 0 \end{bmatrix}=\hbar\upsilon_f\sigma\cdot\vec{q} \qquad (4.17)
$$

where $\hbar\upsilon_f=\frac{3at}{2}$, $\upsilon_f\approx 10^6 m/s$ (the modified speed of light). $\sigma=\left(\sigma_x,\sigma_y\right)$ are the Pauli matrices. The wave function for the momentum around $\vec{K}$ is given by,

$$
\psi_{\pm,\vec{K}}\left(\vec{q}\right)=\frac{1}{\sqrt{2}}\begin{pmatrix} 1 \\ \pm e^{i\theta_{\vec{q}}} \end{pmatrix} \qquad (4.18)
$$

where $\theta_{\vec{q}}=arg(q_x+iq_y)$, and ± represents particle and hole sectors respectively. The eigenvalues are

$$
\epsilon=\pm\hbar\upsilon_f|\vec{q}| \qquad (4.19)
$$

For $\vec{K}'$ point, we can derive a similar equation, written as,

$$
H\left(\vec{q}\right)=\hbar\upsilon_f\sigma^{\dagger}\cdot\vec{q} \qquad (4.20)
$$

where $\sigma^{\dagger}=\left(\sigma_x,-\sigma_y\right)$. The wave function for the momentum around $\vec{K}'$ is given by,

$$
\psi_{\pm,\vec{K}'}\left(\vec{q}\right)=\frac{1}{\sqrt{2}}\begin{pmatrix} 1 \\ \pm e^{-i\theta_{\vec{q}}} \end{pmatrix} \qquad (4.21)
$$

4.3 Electron transport in finite graphene nanoribbons

In the following, we will mainly focus on transport properties of finite graphene nanoribbons. These are of interest as possible semiconducting elements such as wires and transistors. Graphene nanoribbons share a lot of properties of infinite graphene sheets. Due to the finite size confinement, graphene nanoribbons are also similar to carbon nanotubes in that they are both quasi-one-dimensional systems. Depending on the boundary conditions, one can have either metallic or semiconducting graphene nanoribbons. The finite size leads to a quantization in the finite direction and gives rise to "subbands". Graphene nanoribbons are different from carbon nanotubes in that in graphene nanoribbons there exist edges functioning as open boundaries, while in carbon nanotubes no such edges exist. The edges in graphene nanoribbons can bring about exponentially localized edge states originating from the edges. Thus, boundary conditions need to be taken care of carefully in such systems. In Fig. (4.3), we show two types of nanoribbons based on what the edges look like.

- **Armchair nanoribbons** Nanoribbons with armchair edges are called armchair ribbons as shown in the upper half of Fig. (4.3). Note that we label the edges using orange colors. The boundary condition requires that (in a Dirac fermion treatment where q is the deviation from the Dirac point), $\sin\left(q_y W\right) = 0$, with the width $W = \frac{\sqrt{3}a(M+2)}{2}$, M is the number of carbon atoms along the zigzag chain vertical to the armchair edges as shown in the first plot in Fig. (4.3). It can be proved that for $mod(M,3) = 2$, the band gap has a zero solution for $q_x = 0$, that is, armchair ribbons are metallic when $mod(M,3) = 2$. When $mod(M,3) = 0$ or 1, no such zero solution for the band gap exists, thus the armchair ribbons are semiconducting in these

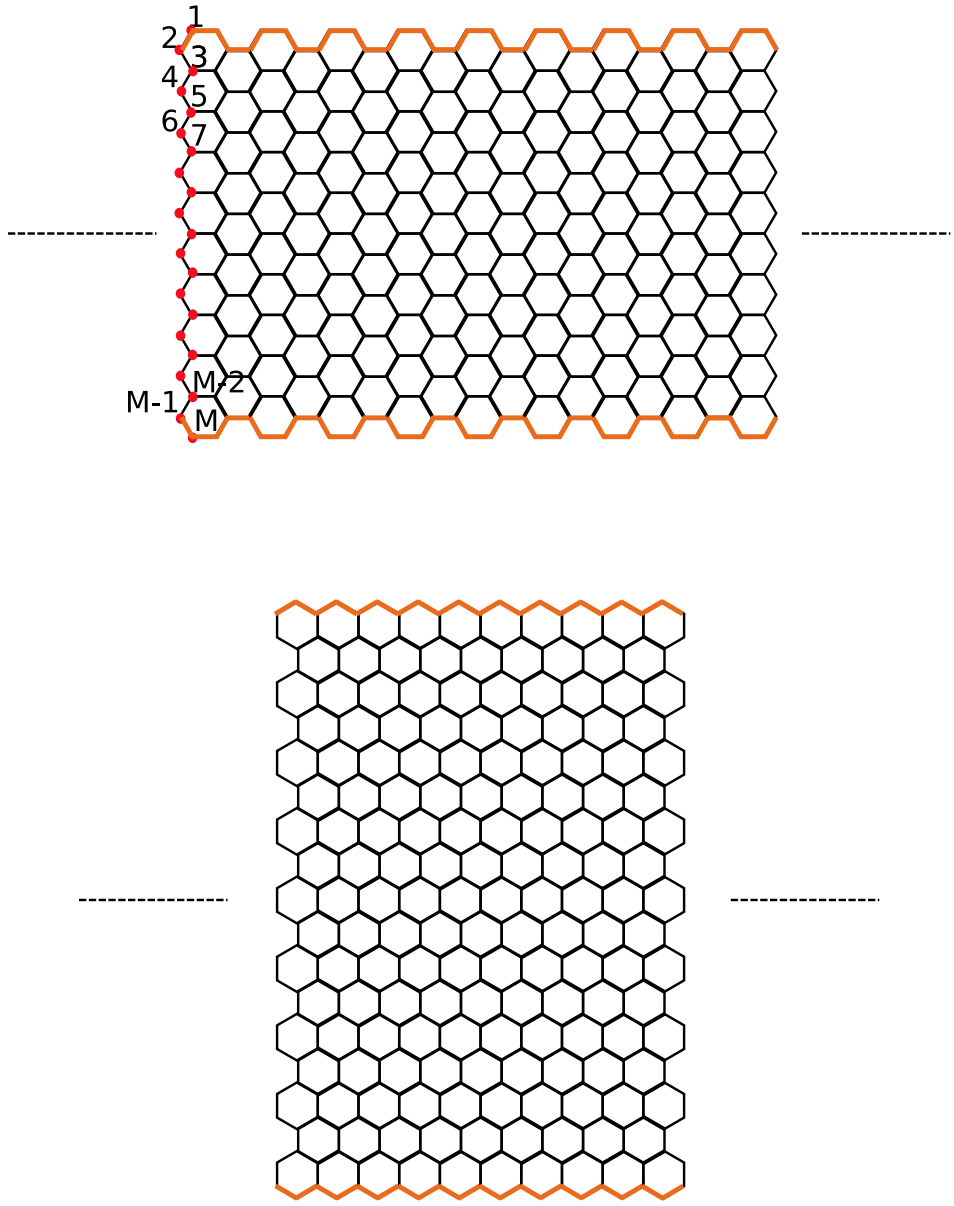

Figure 4.3: Finite graphene nanoribbons. Upper half: armchair nanoribbon, M labels the number of carbon atoms along the zigzag chain vertical to the armchair edges; Lower half: zigzag nanoribbon. We use orange to label the edges of the nanoribbons. Dashed lines stand for the direction along which the nanoribbons extend.

cases [2].

- **Zigzag nanoribbons** Nanoribbons with zigzag edges are called zigzag ribbons as shown in the lower half of Fig. (4.3). One can prove that all zigzag nanoribbons are metallic (i.e. have a vanishing gap) although this vanishing gap is produced by localized edge states [2].

Here we show in Fig. (4.4) the electronic band structures of graphene nanoribbons [3]. The left plot shows the electronic band structure of a metallic armchair nanoribbon in which the conduction band and valence band intersect. For semiconducting armchair nanoribbons, the electronic band structure will have a gap. The right plot shows the electronic band structure of a zigzag nanoribbon, and we notice at zero energy, there exists a flat band, which indicates localized edge states with zero group velocity.

In the following we will first look at the effects of various static scattering sources on the transmission of electrons through graphene nanoribbons, and further the effects of gating. Then we will investigate the effect of dynamic scattering due to electron-electron interactions in graphene nanoribbons.

4.3.1 Static scattering in graphene nanoribbons

In practical experimental preparations of graphene, it is common that the sample graphene sheets contain various defects. These can include adsorbed charge impurities, vacancies, and even substitution atoms, rotated bonds and other such high energy defects as shown in Fig. (4.5). The qualitative and quantitative effect of these defects on electronic transport in graphene has yet to be

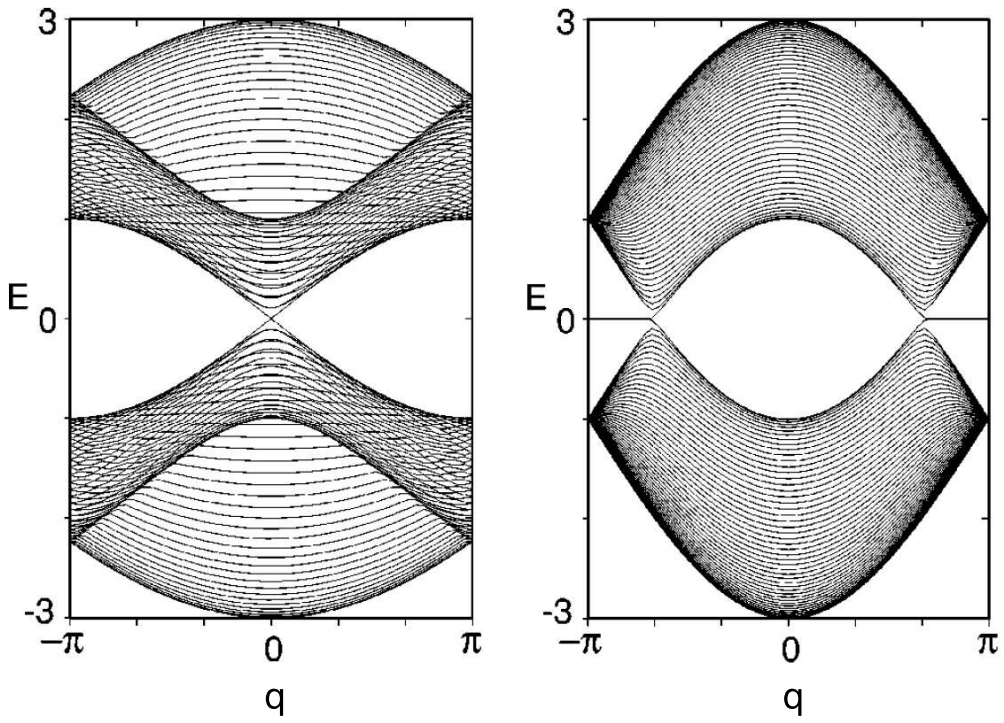

Figure 4.4: Band structures for metallic armchair (left) and zigzag (right) graphene nanoribbons.

fully understood and in the following we carry out a study to see how electron transport is modified in the presence of these various defects. If not mentioned otherwise, the nanoribbon that was used in the following calculations has a length of 32 atoms along the armchair edges and a height of 53 atoms along the zigzag edges, which corresponds to a size of 1696 carbon atoms in total for the nanoribbon. While this is quite small, ribbons of this size can be made at a constriction of a graphene membrane [4]. Within the range of the nanoribbon, we put only a single defect, such as a single charge impurity, a single rotated-bond defect or other types of defects. The location of the defect is chosen to be as close as possible to the center of the nanoribbon.

Our starting point is the Landauer formulation of conductance as discussed

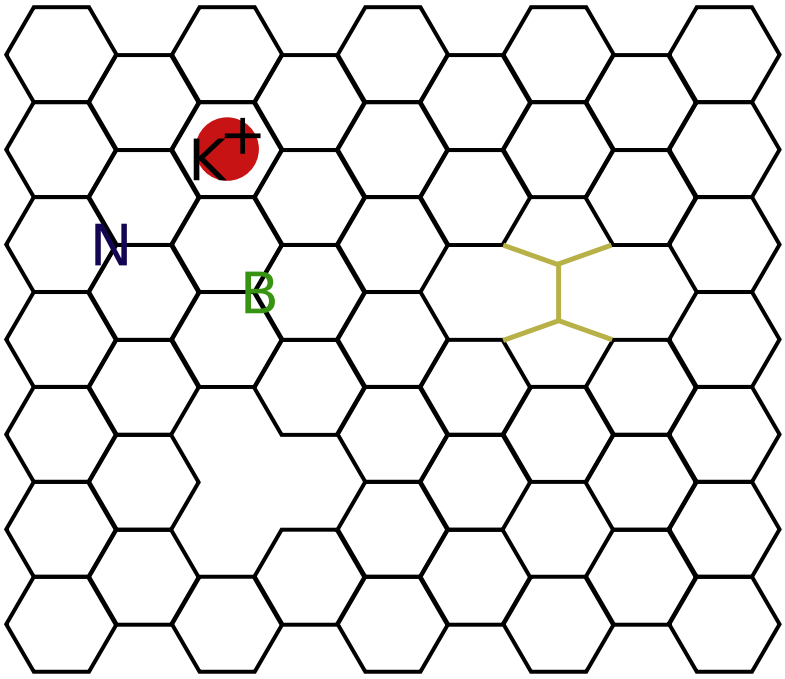

Figure 4.5: Various defects in graphene nanoribbons.

in the previous chapters.

$$G(E) = \frac{2e^2}{h} \sum_{\mu\nu} \mathcal{T}_{\mu\nu}(E) \tag{4.22}$$

$$\mathcal{T}_{\mu\nu} = \mathrm{Tr}(\Gamma_\mu \mathcal{G}^R \Gamma_\nu \mathcal{G}^A) \tag{4.23}$$

where μ and ν stand for different subbands transmitting through the ribbon. This means that we are assuming that transport in graphene is a coherent process. There are conflicting reports of the coherence length of transport in graphene, ranging from 10's of nm's to a few microns. For the sample sizes that we are going to be studying numerically, however, coherent transport is probably appropriate.

Our model of the graphene sheet is a simple tight-binding model.

$$\mathcal{H} = -\sum_{\langle ij \rangle} t_{ij} c_i^\dagger c_j \tag{4.24}$$

where $\langle ij \rangle$ denotes nearest neighbours, and $t_{ij} = 0.1E_h$. An external gate is applied by changing the diagonal elements of $\mathcal{H}$.

Connecting to square electrodes could significantly reduce the transmission because of the contact resistance due to mismatch between the electrodes and the graphene nanoribbon lattices. To make sure all the observed physics is due to the interactions within the graphene region, in the following calculations, we mainly focus on finite graphene nanoribbons of different configurations connected to two hexagonal lattice electrodes of the same width as shown in Fig. (4.6). One can view the problem as studying electron transport on an infinite graphene nanoribbon with a specifically defined region which we call the graphene conductor and the rest being the electrodes. The graphene conductor is chosen large enough such that the finite size effects can be neglected.

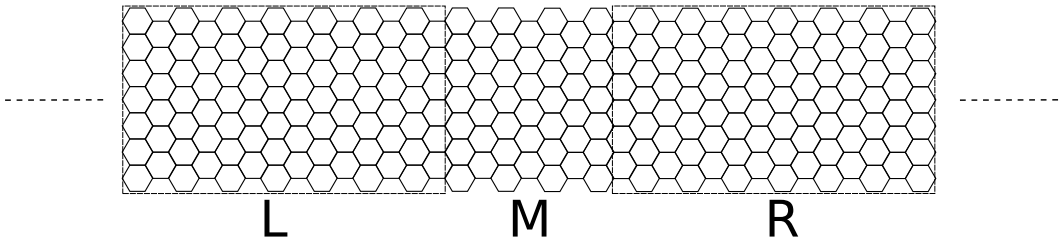

Figure 4.6: Setup for graphene nanoribbon systems (M) with hexagonal lattice electrodes (L and R) of the same width.

Charge impurity scattering in graphene nanoribbons

Charge impurities exist in certain graphitic compounds such as that of intercalation compounds in which a potassium atom is sandwiched between two layers of graphite. They are also probably the most likely impurities to exist in experimental preparations of single layer graphene. Here we are going to look at how

charge impurities can affect the electron transport in graphene nanoribbons. The impurity we use here is a potassium atom on top of the graphene nanoribbon. The distance between the potassium impurity and graphene nanoribbon is one carbon-carbon bond length, that is, 1.42Å.

We treat the impurity as creating a simple electrostatic potential on all the carbon atoms. The Hamiltonian is given as,

$$\mathcal{H} = -\sum_{\langle ij \rangle} t_{ij} c_i^\dagger c_j - \sum_i \frac{Z}{\epsilon R_{Ki}} n_i \tag{4.25}$$

where Z is the charge of the impurity, here we use potassium, so $Z = 1$. ϵ is the dielectric constant (here we set it to 2.0 [5]), and R_{Ki} is the distance between the potassium atom and the ith carbon atom in the graphene sheet.

We first move the impurity to various locations on top of the graphene nanoribbon, and compare the transmission coefficient of a clean graphene nanoribbon and that of a graphene nanoribbon with one potassium charge impurity. Here we show a transmission difference map measured for a metallic armchair nanoribbon, and the black dashed line in the figure shows a benzene ring in the center of the nanoribbon.

We have two key observations:

- When a potassium impurity is located on top of the flat carbon-carbon bond, the transmission difference is fairly small, as indicated by the bright yellow region in the heat map.
- When a potassium impurity is located on top of the center of the benzene ring, the transmission of the nanoribbon with the impurity is reduced by about 9% of that of a clean graphene nanoribbon.

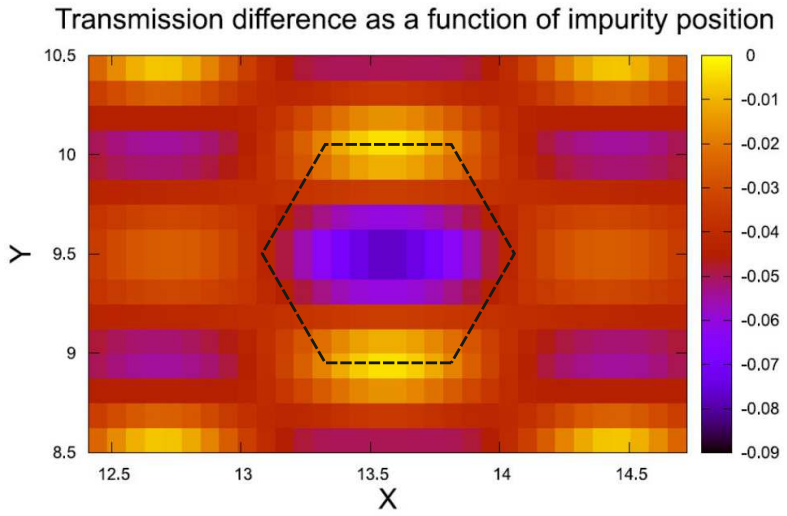

Figure 4.7: Transmission difference between a clean graphene and a graphene with a charge impurity at various locations at a fixed energy. The unit length in x- and y-axis is the graphene lattice constant $\sqrt{3}a$.

Now we will look at the transmission difference at a fixed location but at various energies of the transmitted electron. The top plot shows the measurement for a metallic armchair ribbon, and the bottom plot shows the one of a zigzag ribbon.

The observations we have are:

- Particle-hole symmetry is broken due to the charge impurity.
- The particle sector is noisier as compared to the hole side. The transmission in the hole side is smoothed because of the presence of the charge impurity.
- The potassium impurity with a positive charge acts as an attractive trap for the particle carriers and as a barrier for the hole carriers. Correspondingly, in a transport process, the impurity traps the electron for a while, thus

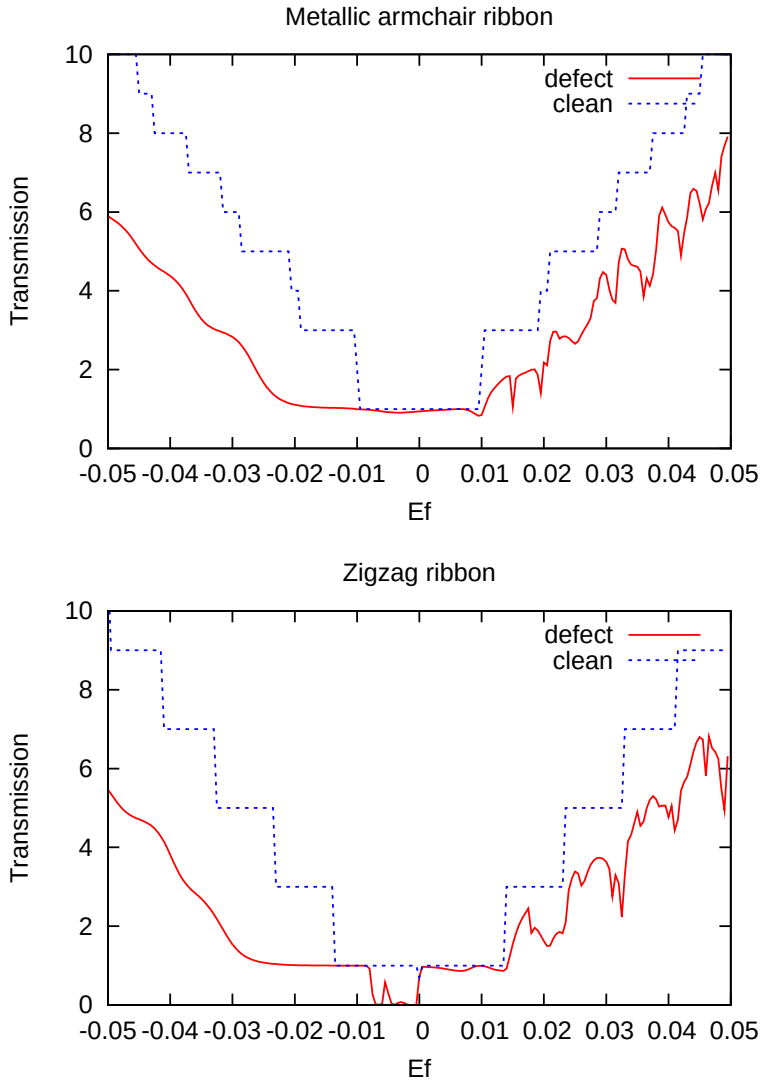

Figure 4.8: Transmission difference between a clean graphene and a graphene with a charge impurity at a fixed location at various energies. The unit for x-axis is Hartree.

forming a virtual bound state that can strongly modify the transmission for the particle sector.

- In the zigzag nanoribbon case, at $E_f = 0$, the transmission coefficient of a clean graphene is reduced due to the localized edge states. For nanoribbons with sufficiently localized edge states, one can show that the transmission coefficient is exponentially decreasing to zero.

- For the zigzag nanoribbon, at low energies, the introduction of a single impurity could completely shutdown the transmission.
- Compared to the zigzag case, for clean graphene measurements, the armchair curve shows an irregular spacing between each jump in the transmission coefficients. This is due to the so-called trigonal warping effect [6], as only existing in armchair graphene nanoribbons.

Vacancy scattering in graphene nanoribbons

We carried out similar calculations on a vacancy in which one of the carbon atoms is deleted from the nanoribbon. Such a defect corresponds to a delta potential, thus is a very short-ranged potential around the defect. Again the top plot shows the transmission calculation for a metallic armchair ribbon, and the bottom plot shows the one for a zigzag ribbon.

Observations:

- Vacancy defects do not break the particle-hole symmetry.
- The peak in the zigzag transmission calculation at zero energy is due to exponentially localized edge states. (In this case, we used a nanoribbon with a fairly small length of 2 atoms along the zigzag edges just for computational convenience as the defect is a short-ranged delta potential). As we increase the length of the graphene nanoribbon across which the transmission is measured, the height of this peak will exponentially decrease.

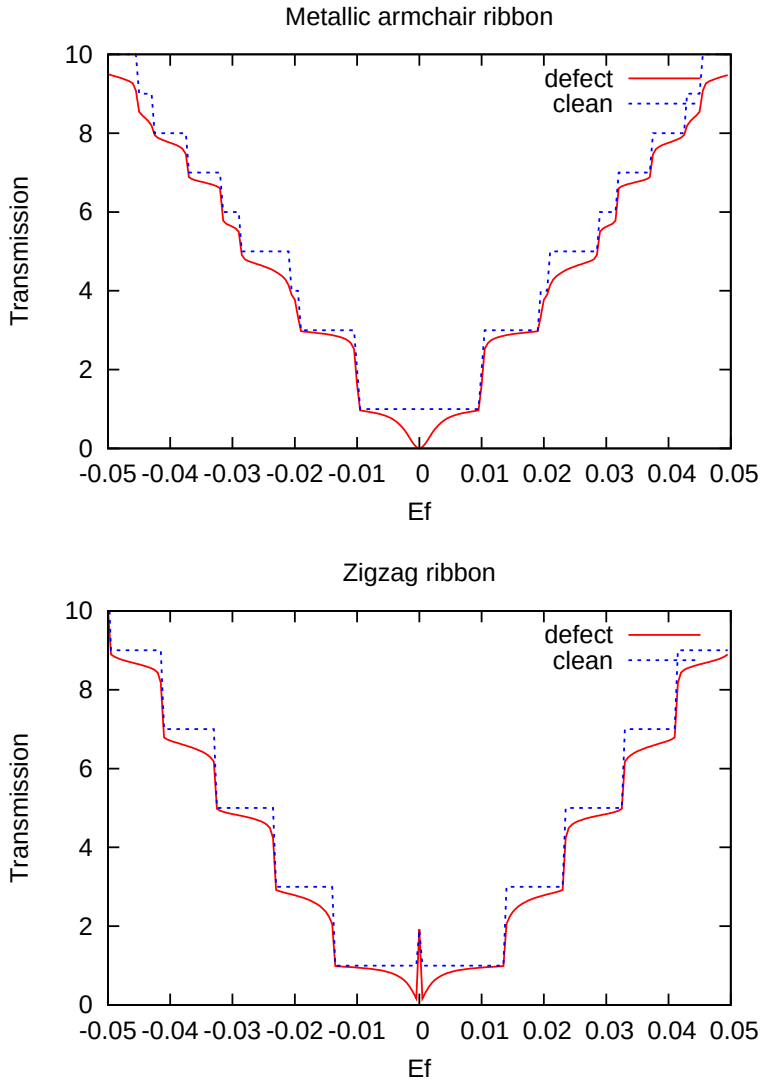

Figure 4.9: Transmission difference between a clean graphene and a graphene with a vacancy at a fixed location at various energies. The unit for x-axis is Hartree.

Substitution elements as scattering sources in graphene nanoribbons

Now we replace a carbon atom by an atom of a different element. The same procedure is carried out for the calculation of the transmission function.

The first one we will look at is the boron element. Boron is less electrostati-

cally negative than carbon, thus the on-site energy is higher than that of carbon. Furthermore the wave function of boron is more diffuse than that of carbon, so the hopping amplitude between boron and neighbouring carbon atoms is larger than that of the carbon-carbon hopping amplitude.

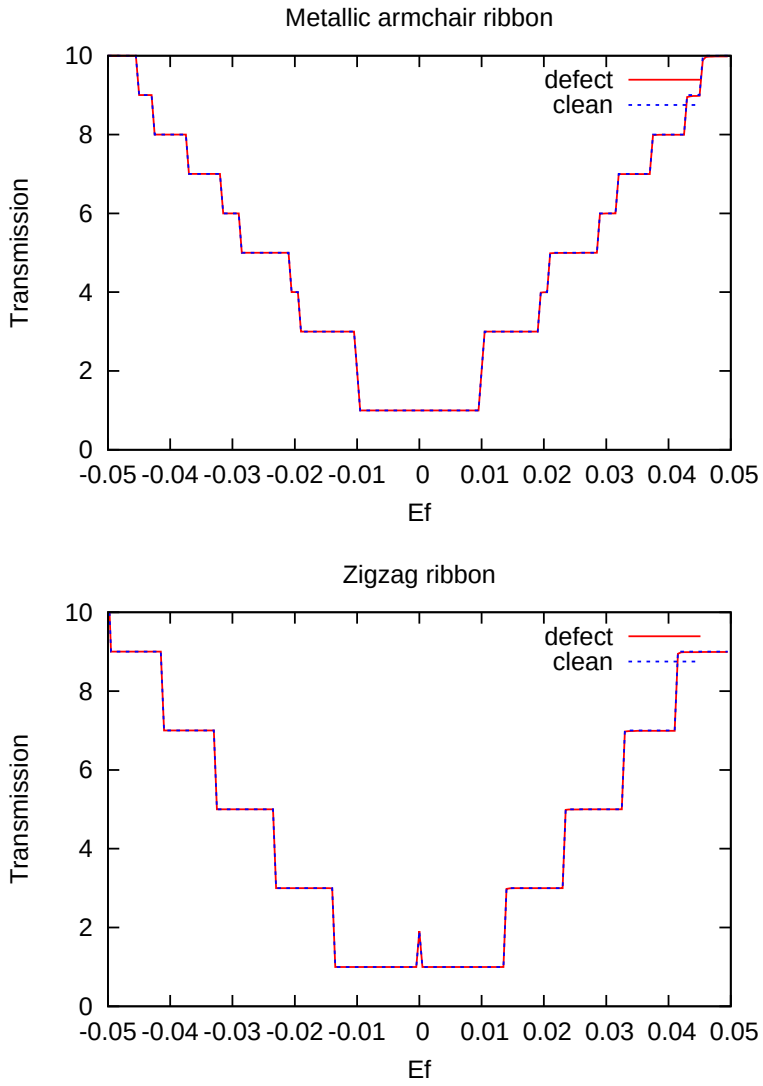

Figure 4.10: Transmission difference between a clean graphene and a graphene with a boron substitution atom at a fixed location at various energies. The unit for x-axis is Hartree.

The second element we look at is nitrogen. Nitrogen is more electrostatically

negative than carbon, thus the on-site energy is lower than that of carbon. And the wave function of nitrogen is less diffuse than that of carbon, so the hopping amplitude between nitrogen and neighbouring carbon atoms is smaller than the one of carbon-carbon hopping amplitude.

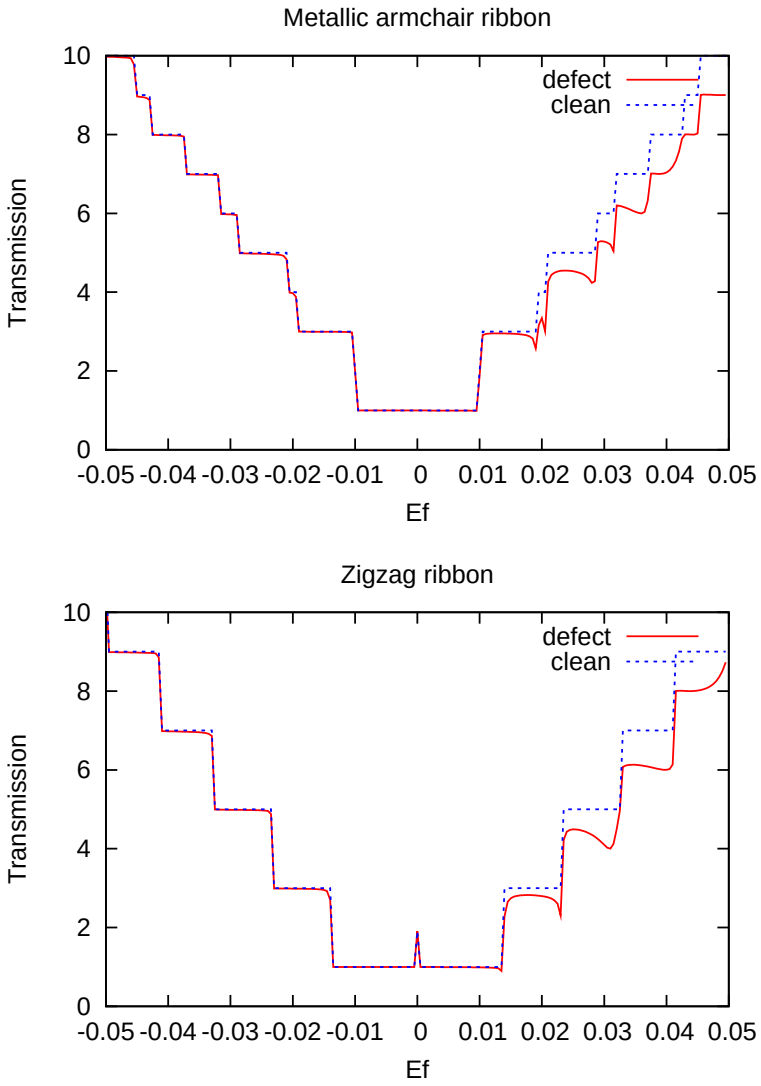

Figure 4.11: Transmission difference between a clean graphene and a graphene with a nitrogen substitution atom at a fixed location at various energies. The unit for x-axis is Hartree.

From the transmission function we have the following observations,

- Using nitrogen as a substitution atom changes the transmission more strongly than using boron as a substitution atom.
- Both boron and nitrogen will break the particle-hole symmetry, although in the boron case, it is not as obvious as in calculations with a nitrogen atom. We can track down the reason by only changing the hopping amplitude without changing the on-site energy as shown in Fig. (4.12). In Fig. (4.12), the hopping amplitudes change from $0.1t$ to $0.5t$ and $2.0t$. We can see from the plots, that when the hopping amplitude between the defect and neighbouring carbon atoms equals to $0.1t$, the change of the transmission is strongest. This corresponds to forming a virtual bound state around the defect. Using $2.0t$ as the hopping amplitude barely changes the transmission as the electron spends too little time on the defect to notice the difference in site-potential.

Bond rotation scattering in graphene nanoribbons

Topological disorder such as bond rotation (Stone-Wales defects) can occur at high temperatures. In a Stone-Wales defect, four hexagons are changed into two pentagons and two heptagons as shown in Fig. (4.5). Fig. (4.13) shows the transmission difference between a clean graphene nanoribbon and a nanoribbon with a single Stone-Wales defect.

Observations:

- A rotated bond breaks particle-hole symmetry. The loss of particle-hole symmetry can be understood from the loss of alternancy in the system.

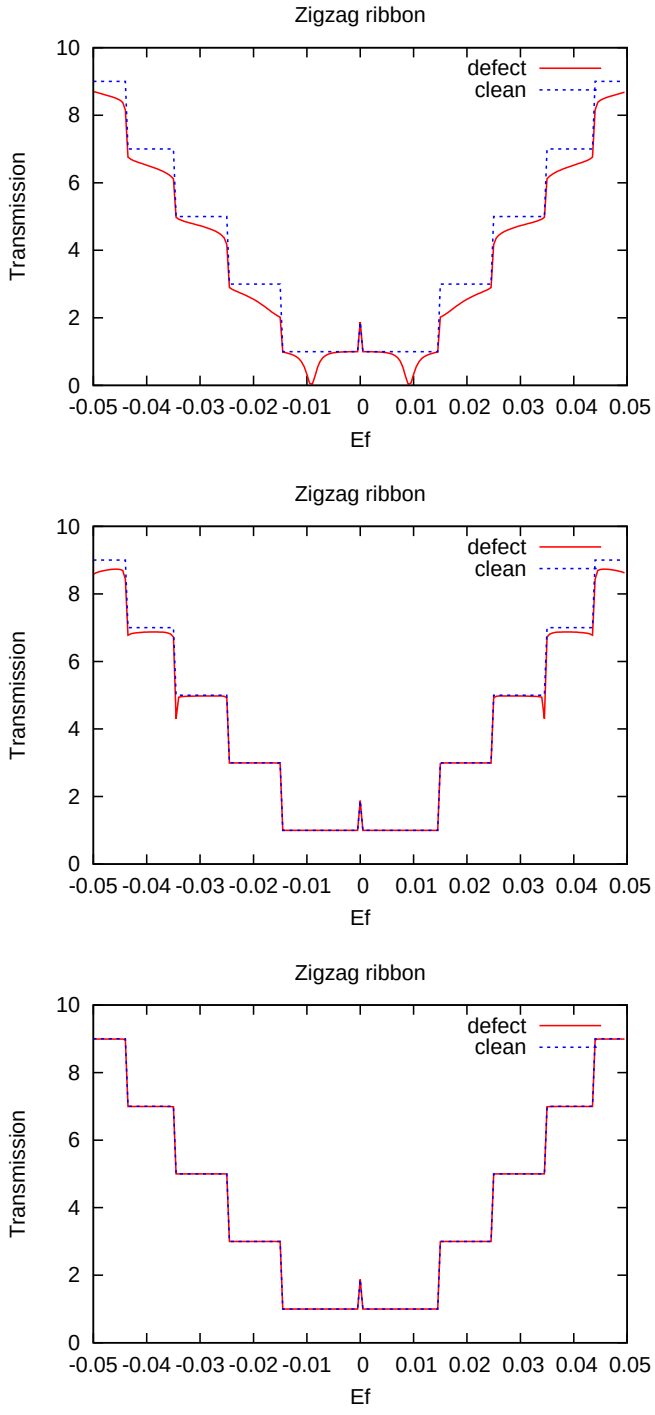

Figure 4.12: Transmission difference between a clean graphene and a graphene with a carbon atom at a fixed location with modified hopping amplitude to neighbouring carbon atoms at various energies. The unit for x-axis is Hartree. The hopping amplitude between the defect and neighbouring carbon atoms changes from $0.1t$, $0.5t$ to $2.0t$, corresponding to the top, middle and bottom plots respectively.

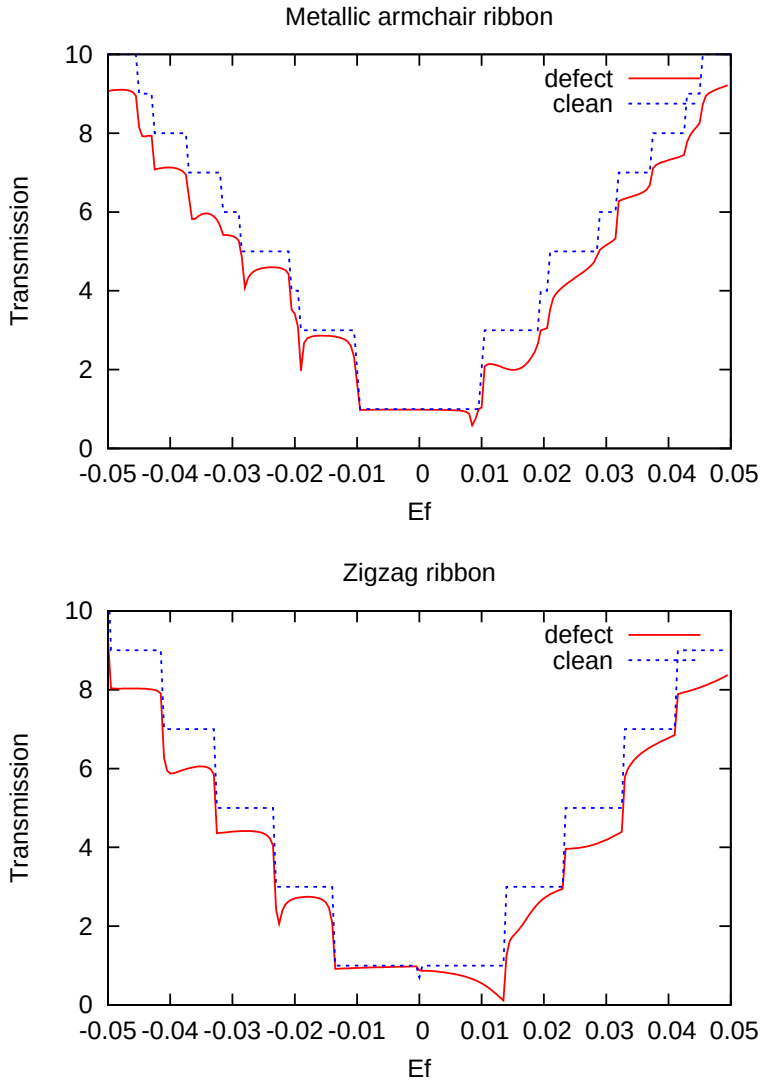

Figure 4.13: Transmission difference between a clean graphene and a graphene with a rotated bond at a fixed location at various energies. The unit for x-axis is Hartree.

One can show that such a topological disorder induces a gauge field in the Dirac theory, which breaks the particle-hole symmetry [7].

Gating effect in graphene nanoribbons

Applying a gate on a fragment of graphene leads to interesting transport phenomena. This is because relativistic particles show very different behaviour when tunneling through a potential barrier because of the existence of negative energy states. Unimpeded penetration of relativistic particles across barriers through virtual negative energy states is known as Klein scattering, and is sometimes also known as the Klein paradox mainly because for a normal particle that is described by the Schrödinger's equation, when such a barrier is present, the wave function decays exponentially in the gated barrier region, thus leading to a significant reduction of transmission. The analogy between scattering in infinite graphene sheets and Klein scattering of relativistic particles was first studied in Ref. [8] using Dirac theory. Here we study the Klein scattering in a finite graphene nanoribbons in the tight-binding limit.

In real space, the wave function in the particle/hole sector (+/−) can be written as:

$$\psi_{\pm,\vec{K}}(\vec{r}) = \frac{1}{\sqrt{2}} \begin{pmatrix} 1 \\ \pm e^{i\theta_{\vec{q}}} \end{pmatrix} e^{i\vec{q}\cdot\vec{r}} \tag{4.26}$$

where $\vec{q} = \vec{K} - \vec{k}$, i.e. is the momentum relative to the Dirac point $\vec{K}$, and $\theta_{\vec{q}} = arg(q_x + iq_y)$.

The wave function in the scattering process can be written as a superposition of the transmitted wave and reflected wave. The different regions involved in scattering are shown in Fig. (4.14).

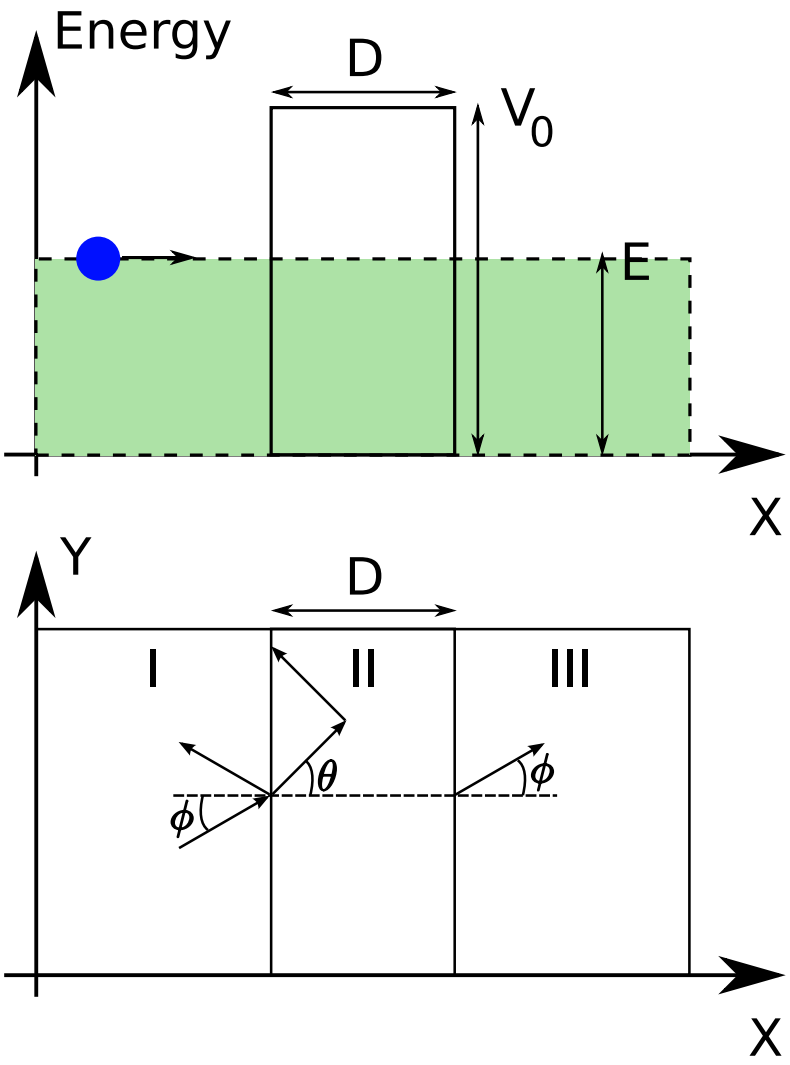

Figure 4.14: Top: schematic picture of the scattering of Dirac fermions by a square gate. Bottom: definition of the angles ϕ and θ used in the scattering formalism in region I, II and III.

In region I, we have,

$$\psi_I(\vec{r}) = \frac{1}{\sqrt{2}}\left[\begin{pmatrix} 1 \\ se^{i\phi} \end{pmatrix} e^{i(k_x x + k_y y)} + r\begin{pmatrix} 1 \\ se^{i(\pi-\phi)} \end{pmatrix} e^{i(-k_x x + k_y y)}\right] \tag{4.27}$$

where $\phi = arctan\left(k_y/k_x\right)$, $k_x = k_f cos\phi$ and $k_y = k_f sin\phi$.

In region II, we have,

$$\psi_{II}(\vec{r}) = \frac{1}{\sqrt{2}}\left[a\begin{pmatrix}1\\ s'e^{i\theta}\end{pmatrix}e^{i(p_x x+k_y y)} + b\begin{pmatrix}1\\ s'e^{i(\pi-\theta)}\end{pmatrix}e^{i(-p_x x+k_y y)}\right] \tag{4.28}$$

where $\theta = arctan\left(k_y/p_x\right)$, $s' = sign\,(E - V_0)$ and $p_x = \sqrt{(V_0 - E)^2/\upsilon_f^2 - k_y^2}$. V_0 is the height of the square barrier.

In region III, we have,

$$\psi_{III}(\vec{r}) = \frac{1}{\sqrt{2}}\left[t\begin{pmatrix}1\\ se^{i\phi}\end{pmatrix}e^{i(k_x x+k_y y)}\right] \tag{4.29}$$

where $s = sign\,(E)$.

The coefficients r, a, b and t are determined by matching the wave function at the boundaries. The transmission coefficient is given by t^*t,

$$T(\phi) = \frac{cos^2\theta cos^2\phi}{\left[cos\,(Dq_x)\,cos\phi cos\theta\right]^2 + \left[sin\,(Dq_x)\,(1 - ss'sin\phi sin\theta\right]^2} \tag{4.30}$$

where D is the width of the square barrier.

There are several important results to note. Firstly, for normal incidence, the transmission is always equal to one for any barrier potential with $V_0 > E$! Secondly, the transmission has a complicated angular dependence, as shown in Fig. (4.15) (see more in Ref. [8]).

Here we will look at mainly three types of gating effects in graphene nanoribbons: (i) a normal square gate (the left grey region), (ii) a rotated square gate (the right grey region), and (iii) a mass gate (the middle one with two different on-site energies).

The normal square gate refers to applying a square gate voltage in a rectangular region whose long axis is perpendicular to the graphene nanoribbon with

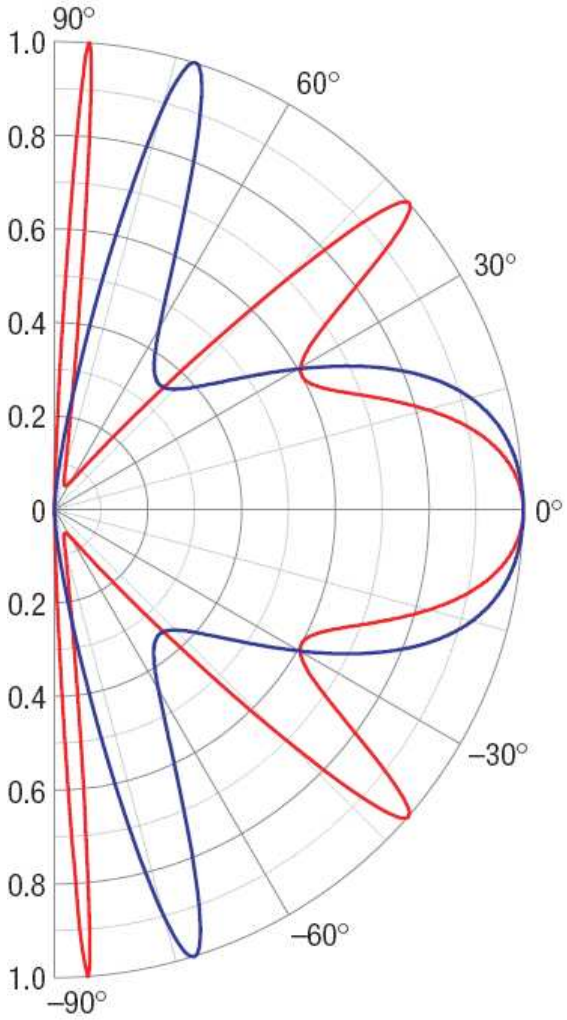

Figure 4.15: Angular dependence of the transmission function in Klein scattering in graphene sheets. In the plot, the two curves stand for different concentrations of hole carriers within the barrier region.

a width of ten times of the graphene lattice constant $\sqrt{3}a$. In order to study the angular dependence of the gating effect, we apply rotated square gates with various angles. The nanoribbon used in the calculations has 41 atoms along the zigzag edges and 70 atoms along the armchair edges. The height of the gated barrier potential is $0.030Eh$ with a rotation angle ranging from 0° to 45°. The injection energy of the electron from the electrode is set to be $0.005Eh$. We then

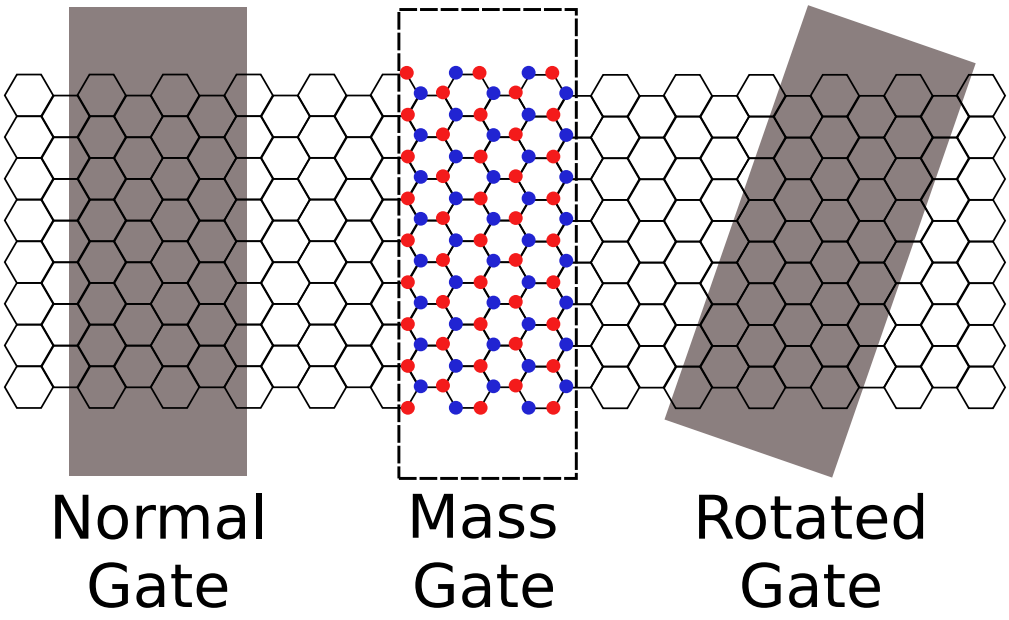

Figure 4.16: Various types of gates applied to graphene nanoribbon.

plot the transmission coefficient as a function of the rotation angle of the applied gate for the first subband.

When the rotation angle of the gate is 0°, i.e. the normal gate, we get perfect transmission, i.e. $T = 1$, as expected in the analytical result in Eq. (4.30), As we rotate the gate, the transmission shows a strong angular dependence.

Mass gate refers to changing the on-site energies of the carbon atoms on the A and B sublattices separately. The analogous effect in the Dirac fermion picture is to give mass to the particles, hence the name mass gate. Here we first apply a small normal square gate of $0.001Eh$, and then vary the mass gate values M from $0.000Eh$ to $0.002Eh$, which ensures that only the first subband is under study. Technically the mass gate is implemented by shifting the on-site energy of carbon by $\pm M$ on atoms of sublattice A and sublattice B respectively within the region where the normal square gate is applied. By doing so, one can open up a band gap of $2M$, that is originally absent in graphene with massless

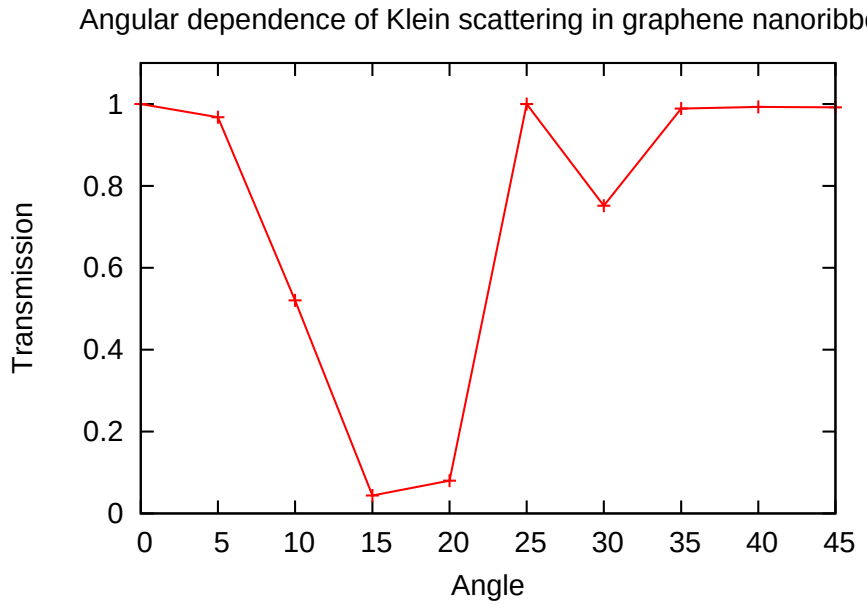

Figure 4.17: Angular dependence of the transmission coefficient. The unit for the angle is degree.

fermions.

We find that in range $[0.001, 0.002]$, the transmission decreases exponentially just as expected for a semiconductor with a band gap, i.e. the electrons are feeling the ordinary square gate potential. In range $[0.000, 0.001]$, the transmission decreases due to the back-scattering.

4.3.2 Dynamic scattering in graphene nanoribbons

Besides static scattering processes from defects, another class of scattering processes that is interesting to us is the dynamic scattering process. In particular, we will investigate how electron-electron interactions can change the electron transport process.

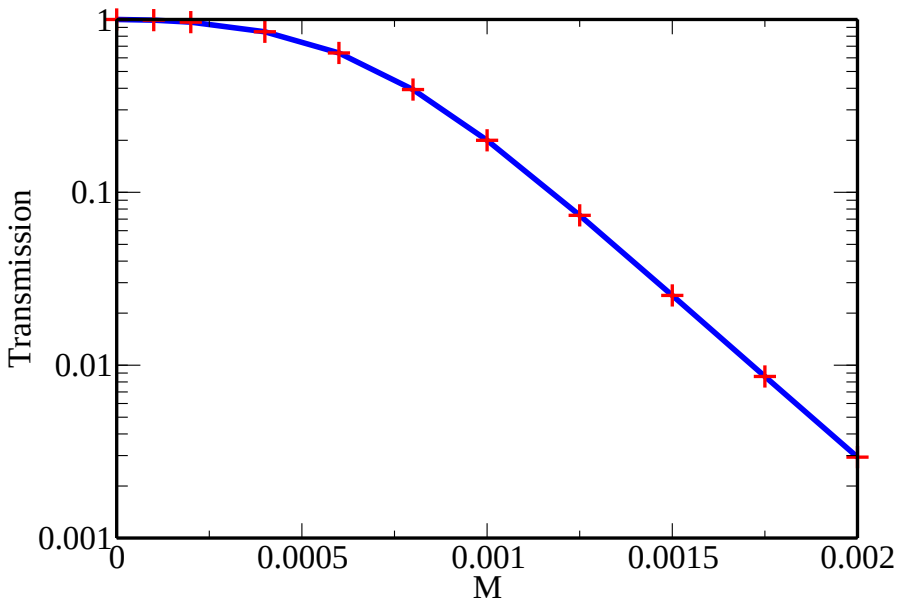

Figure 4.18: Transmission with various mass gates. The unit for x-axis is Hartree.

We use the Pariser-Parr-Pople (PPP) model [9, 10] to describe the electron-electron interactions in the conductor. This is given by

$$\mathcal{H} = -\sum_{\langle ij \rangle} t_{ij} c_i^\dagger c_j + \sum_{ij} U_{ij}(n_i^\uparrow - 1)(n_i^\downarrow - 1) \tag{4.31}$$

$\langle ij \rangle$ denotes nearest neighbours. $t_{ij} = 0.1E_h$. The electron-electron interaction in graphene is introduced through the second term in which U_{ij} is given by the parametrization, $1/\epsilon_0(\gamma_0^{-1} + R_{ij})$ where $\gamma_0 = 10.84eV$, R_{ij} is the distance between carbon atoms on site i and site j, ϵ_0 is the dielectric constant (here we set to 2.0).

In the earlier studies the (graphene) electrodes were treated as non-interacting, but to avoid a spurious contact resistance, especially at nonzero energies, we need to include the effects of Coulomb interactions within the electrodes as well. To do this we first apply periodic boundary condition on a finite clean graphene nanoribbon. The periodicity is only applied across the direction of the nanoribbon along which the conductance is measured. The size of

the unit cell is chosen to be large enough such that the variation of the periodic potential built from all the electrons in the unit cell is small as compared to hopping amplitude between neighbouring carbon atoms. For each energy, a self-consistent field calculation is then carried out. We then feed the converged Fock operator into the numerical renormalization group procedure to get the surface greens function for the infinite graphene electrodes with the electron-electron interactions included. For calculations with an impurity, we carry out another SCF calculation with the same periodic boundary condition as that of clean graphene. For the self-energy due to the coupling between the electrodes and the conductor, we use the same diagonal elements from the clean graphene calculation.

The first plot shows the tight-binding result for an metallic armchair nanoribbon as in Fig. (4.8). The second plot shows the transmission where the electron-electron interaction is described by the PPP model for the same fragment of graphene nanoribbon as in the first plot.

Observations:

- Due to the relaxation of the electron density in the presence of the electron-electron interactions, the transmission function is smoothed compared to the one in the tight-binding calculation.
- The subband spacings are broader due to the electron-electron repulsion.

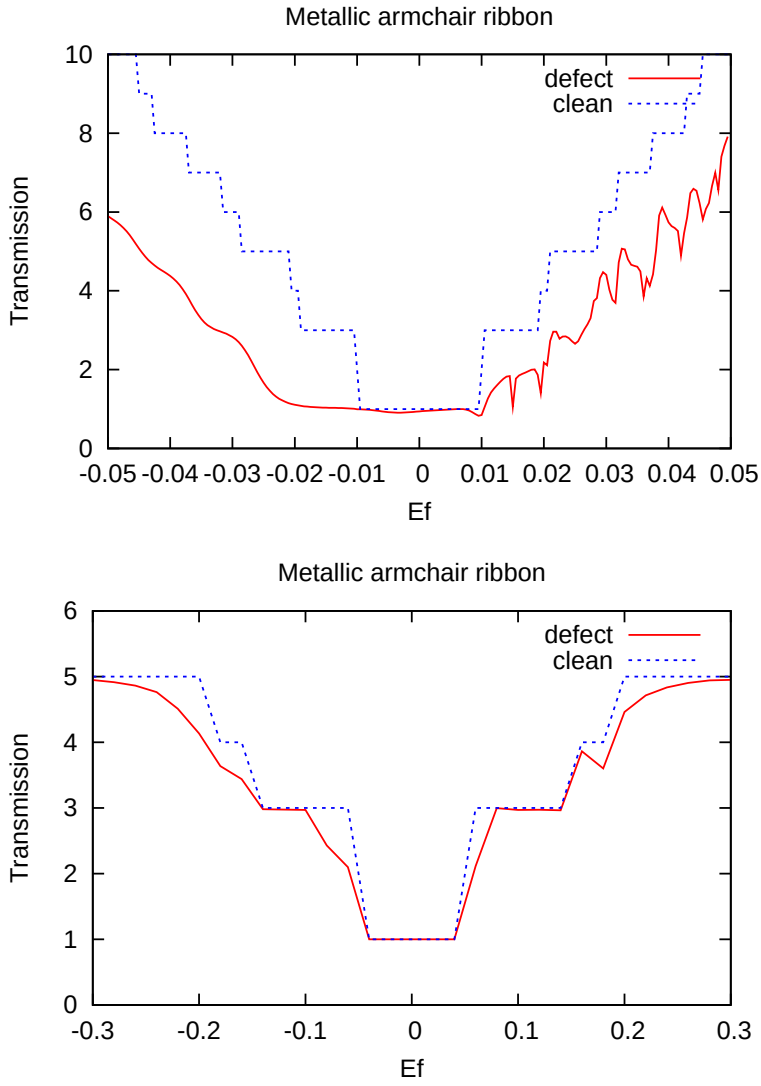

Figure 4.19: Transmission difference between a clean graphene and a graphene with a charge impurity at a fixed location at various energies. Top plot: transmission difference in the tight-binding limit; Bottom plot: transmission difference with electron-electron interactions as described by the PPP model. The unit for x-axis is Hartree.

4.4 Conclusions

To shortly summarize, in this chapter, by utilizing the Landauer formula, we studied the effects of various defects in graphene on the transmission of elec-

trons in the tight-binding limit. We found that different kinds of defects are associated with different characteristic changes in transmission. We also studied the effects of gating in graphene nanoribbons. We showed that the transmission coefficient has a strong angular dependence on the rotated gate potentials. Applying a mass gate to graphene nanoribbons exponentially reduces the transmission. We further utilized the Pariser-Parr-Pople model and investigated how dynamic scattering process such as electron-electron interaction modifies the transmission of the electrons.

BIBLIOGRAPHY

[1] K. S. Novoselov, A. K. Geim, S. V. Morozov, D. Jiang, Y. Zhang, S. V. Dubonos, I. V. Grigorieva, and A. A. Firsov. Electric Field Effect in Atomically Thin Carbon Films. *Science*, 306:666, 2004.

[2] K. Nakada, M. Fujita, G. Dresselhaus, and M. S. Dresselhaus. Edge State in Graphene Ribbons: Nanometer Size Effect and Edge Shape Dependence. *Phys. Rev. B*, 54:17954, 1996.

[3] K. Wakabayashi, M. Fujita, H. Ajiki, and M. Sigrist. Electronic and Magnetic Properties of Nanographite Ribbons. *Phys. Rev. B*, 59:8271, 1998.

[4] L. A. Ponomarenko, F. Schedin, M. I. Katsnelson, R. Yang, E. W. Hill, K. S. Novoselov, and A. K. Geim. Chaotic Dirac Billiard in Graphene Quantum Dots. *Science*, 320:356, 2008.

[5] E. H. Hwang, S. Adam, and S. Das Sarma. Carrier Transport in Two-Dimensional Graphene Layers. *Phys. Rev. Lett.*, 98:186806, 2007.

[6] R. Saito, G. Dresselhaus, and M. S. Dresselhaus. Trigonal Warping Effect of Carbon Nanotubes. *Phys. Rev. B*, 61:2981, 2000.

[7] J. Gonzale, F. Guine, and M. A. H. Vozmediano. Electron-Electron Interactions in Graphene Sheets. *Phys. Rev. B*, 63:134421, 2001.

[8] M. I. Katsnelson, K. S. Novoselov, and A. K. Geim. Chiral Tunnelling and the Klein Paradox in Graphene. *Nat. Phys.*, 2:620, 2006.

[9] R. Pariser and R. G. Parr. A Semi-Empirical Theory of the Electronic Spectra and Electronic Structure of Complex Unsaturated Molecules. I. *J. Chem. Phys.*, 21:466, 1953.

[10] J. A. Pople. Electron Interaction in Unsaturated Hydrocarbons. *Trans. Faraday Soc.*, 49:1375, 1953.

CHAPTER 5

CONCLUSIONS

In this thesis, we first introduced the single-particle Landauer formulation of electron transport. We further investigated an exact scheme to go beyond a single-particle picture by combining the non-equilibrium Green's function formalism with the equation of motion Green's function technique. This leads to a hierarchical set of equations for the many-body Green's functions. We found significant qualitative differences in the high-bias regime between the usual mean-field theory and an improved theory that was truncated at a higher level of the Green's function hierarchy. We then utilized the non-equilibrium Green's function formalism combined with Hartree-Fock theory to study the Coulomb blockade problem in the small bias limit as seen in some weakly-coupled metal-ligand clusters. Here we tried to understand the effect of electron self-interaction on the reproduction of the Coulomb blockade features. Finally we used the standard Landauer formalism to study the effect of defects on transport through graphene nanoribbons in a tight-binding description. We found that different kinds of defects are associated with different characteristic changes in transmission. We also studied the effects of gating in graphene nanoribbons, where we found that the transmission coefficient has a strong angular dependence on the rotated gate potentials, while applying a mass gate exponentially reduces the transmission. We further studied the effect of dynamic scattering, especially the electron-electron interactions, within the nanoribbons. The inclusion of electron-electron interactions opened up the spacing between subbands, thus making the transmission coefficients drastically different as compared to the tight-binding calculations.

The electron transport problem has been under heavy investigation in both chemistry and physics. One of the interesting future directions of research could be to utilize the density matrix renormalization group (DMRG) method to study the effects of electron-electron interactions in strongly correlated electron transport. Interesting phenomenon such as the Kondo resonance can only be explained when the multi-reference nature of the wave function can be treated correctly. Many of the systems that have been studied can be viewed as one-dimensional or quasi-one-dimensional systems, for which the DMRG method provides a quasi-exact description of the electronic structure. Possible extensions to the electron transport problem have been recently proposed by several groups [1, 2]. As to the application side, it would be a very interesting study to try to understand how the optically *dark* states modify the electron transport process in the light-harvesting molecule β-carotene which was one of the first molecules used in early molecular transport experiments and of which the electronic structure was recently studied using *ab-initio* DMRG method [3].

BIBLIOGRAPHY

[1] D. Bohr, P. Schmitteckert, and P. Wolfle. DMRG Evaluation of the Kubo Formula – Conductance of Strongly Interacting Quantum Systems. *Europhys. Lett.*, 73:246, 2006.

[2] K. A. Al-Hassanieh, A. E. Feiguin, J. A. Riera, C. A. Busse, and E. Dagott. Adaptive Time-Dependent Density-Matrix Renormalization-Group Technique for Calculating the Conductance of Strongly Correlated Nanostructures. *Phys. Rev. B*, 73:195304, 2006.

[3] D. Ghosh, J. Hachmann, T. Yanai, and G. K.-L. Chan. Orbital Optimization in the Density Matrix Renormalization Group, with Applications to Polyenes and Beta-Carotene. *J. Chem. Phys.*, 128:144117, 2008.

APPENDIX A

APPENDIX

A.1 Basics of Green's functions

In mathematics, Green's functions have been widely used to solve various inhomogeneous differential equations. Particularly, in quantum mechanics, noticing that the Schrödinger equation is of the type of an inhomogeneous differential equation, we can utilize the Green's function to solve for the evolution of the electronic wave function. We will start our adventure by first introducing three pictures for solving a quantum mechanical problem, namely, the Schrödinger picture, the Heisenberg picture and the interaction picture.

A.1.1 Schrödinger picture

In basic quantum mechanics, we typically assume that the electronic wave function of the Schrödinger equation is time-dependent, while the operators are time-independent,

$$i\hbar\frac{\partial}{\partial t}|\Psi_S\,(t)\rangle = \hat{H}|\Psi_S\,(t)\rangle \tag{A.1}$$

where $\hat{H}$ is the Hamiltonian operator (The *hat* symbol indicates that this is an operator), which we assume is not explicitly dependent on time. We use the subscript S to denote that we are working in the Schrödinger picture.

The formal solution of the equation above is,

$$|\Psi_S\,(t)\rangle = e^{-i\hat{H}(t-t_0)/\hbar}|\Psi_S\,(t_0)\rangle \tag{A.2}$$

As we can see, the wave function at time t is entirely determined by the initial condition $|\Psi(t_0)\rangle$. Although people work in the Schrödinger picture for many problems, the description of the evolution of the wave function in the Schrödinger picture has certain drawbacks, e.g., when the Hamiltonian is time-dependent, the wave function no longer follows such a simple form as that shown in Eq. (A.2), and numerically it could be challenging to solve for the evolution of the wave function in an easy way.

A.1.2 Heisenberg picture

In the Schrödinger picture, we assume that the operators are time-independent, and the wave function is time-dependent. On the contrary, in the Heisenberg picture, we assume that the operators are time-dependent, and the wave functions are time-independent. Pictorially this corresponds to a rotation of the coordinate frame. Instead of solving for the evolution of the wave function, in the Heisenberg picture, we solve for the evolution of the operators.

$$|\Psi_H(t)\rangle \equiv e^{i\hat{H}t/\hbar}|\Psi_S(t)\rangle \tag{A.3}$$

where we use the subscript H to denote that we are working in the Heisenberg picture.

The time derivative of $|\Psi_H(t)\rangle$ is given by,

$$\begin{aligned} i\hbar\frac{\partial}{\partial t}|\Psi_H(t)\rangle &= \left(i\hbar\frac{\partial}{\partial t}e^{i\hat{H}t/\hbar}\right)|\Psi_S(t)\rangle + e^{i\hat{H}t/\hbar}\left(i\hbar\frac{\partial}{\partial t}|\Psi_S(t)\rangle\right) \\ &= \left(-He^{i\hat{H}t/\hbar}\right)|\Psi_S(t)\rangle + e^{i\hat{H}t/\hbar}\left(H|\Psi_S(t)\rangle\right) = 0 \end{aligned} \tag{A.4}$$

showing that $|\Psi_H(t)\rangle$ is time-independent.

In order to compute the operators in the Heisenberg picture, we need to carry out a unitary transformation of the operators in the Schrödinger picture.

$$\langle \Psi'_S(t) \left| \hat{O}_S \right| \Psi_S(t) \rangle = \langle \Psi'_H \left| e^{i\hat{H}t/\hbar} \hat{O}_S e^{-i\hat{H}t/\hbar} \right| \Psi_H \rangle \tag{A.5}$$

This gives an operator in the Heisenberg picture, written as,

$$\hat{O}_H(t) = e^{i\hat{H}t/\hbar} \hat{O}_S e^{-i\hat{H}t/\hbar} \tag{A.6}$$

Now we can write down the equation of motion for operator $\hat{O}_H(t)$.

$$\begin{aligned} i\hbar \frac{\partial}{\partial t} \hat{O}_H(t) &= i\hbar \frac{\partial}{\partial t} \left(e^{i\hat{H}t/\hbar} \hat{O}_S e^{-i\hat{H}t/\hbar} \right) \\ &= \left(-\hat{H} e^{i\hat{H}t/\hbar} \hat{O}_S e^{-i\hat{H}t/\hbar} \right) + \left(e^{i\hat{H}t/\hbar} \hat{O}_S \hat{H} e^{-i\hat{H}t/\hbar} \right) \\ &= \left[e^{i\hat{H}t/\hbar} \hat{O}_S e^{-i\hat{H}t/\hbar}, \hat{H} \right] \\ &= [\hat{O}_H, \hat{H}] \end{aligned} \tag{A.7}$$

A.1.3 Interaction picture

Sometimes a small perturbation or some kind of external field might be added to an easily solvable Hamiltonian. In this case, we divide the Hamiltonian into an easily solvable part and a difficult part. Instead of treating the two parts in the Hamiltonian on the same footing like what we did in the Heisenberg picture, we will work in the so-called interaction picture, where we have the Hamiltonian written as,

$$\hat{H} = \hat{H}_0 + \hat{H}_{int} \tag{A.8}$$

and

$$|\Psi_I(t)\rangle \equiv e^{i\hat{H}_0 t/\hbar} |\Psi_S(t)\rangle \tag{A.9}$$

where we use the subscript I to indicate that we are working in the interaction picture.

Now taking the time derivative of $|\Psi_I(t)\rangle$ gives us,

$$\begin{aligned} i\hbar\frac{\partial}{\partial t}|\Psi_I(t)\rangle &= \left(i\hbar\frac{\partial}{\partial t}e^{i\hat{H}_0 t/\hbar}\right)|\Psi_S(t)\rangle + e^{i\hat{H}_0 t/\hbar}\left(i\hbar\frac{\partial}{\partial t}|\Psi_S(t)\rangle\right) \\ &= e^{i\hat{H}_0 t/\hbar}\left[-\hat{H}_0 + \hat{H}_0 + \hat{H}_{int}\right]e^{-i\hat{H}_0 t/\hbar}|\Psi_I(t)\rangle \\ &= e^{i\hat{H}_0 t/\hbar}\hat{H}_{int}e^{-i\hat{H}_0 t/\hbar}|\Psi_I(t)\rangle \end{aligned} \tag{A.10}$$

In the interaction picture, not only the wave function is time-dependent, but also the operators are time-dependent. We then write down the equation of motion for operators in the interaction picture, similar to what we did for operators in the Heisenberg picture. We then get,

$$\hat{O}_I(t) \equiv e^{i\hat{H}_0 t/\hbar}\hat{O}_S e^{-i\hat{H}_0 t/\hbar} \tag{A.11}$$

Thus, for operators in the interaction picture, we have,

$$\hat{H}_{int,I}(t) \equiv e^{i\hat{H}_0 t/\hbar}\hat{H}_{int}e^{-i\hat{H}_0 t/\hbar} \tag{A.12}$$

The equation of motion for the wave function is then given by,

$$i\hbar\frac{\partial}{\partial t}|\Psi_I(t)\rangle = \hat{H}_{int,I}(t)\,|\Psi_I(t)\rangle \tag{A.13}$$

In the interaction picture, the equation of motion for the operators is given by,

$$i\hbar\frac{\partial}{\partial t}\hat{O}_I(t) = \left[\hat{O}_I(t), \hat{H}_0\right] \tag{A.14}$$

Now we solve for the wave function in the interaction picture.

$$|\Psi_I(t)\rangle = \hat{U}(t, t_0)\,|\Psi_I(t_0)\rangle \tag{A.15}$$

$$
\begin{aligned}
|\Psi_I(t)\rangle &= e^{i\hat{H}_0 t/\hbar}|\Psi_S(t)\rangle \\
&= e^{i\hat{H}_0 t/\hbar}e^{-i\hat{H}(t-t_0)/\hbar}|\Psi_S(t_0)\rangle \\
&= e^{i\hat{H}_0 t/\hbar}e^{-i\hat{H}(t-t_0)/\hbar}e^{-i\hat{H}_0 t/\hbar}|\Psi_I(t_0)\rangle
\end{aligned} \tag{A.16}
$$

$$
\hat{U}(t,t_0) = e^{i\hat{H}_0 t/\hbar}e^{-i\hat{H}(t-t_0)/\hbar}e^{-i\hat{H}_0 t/\hbar} \tag{A.17}
$$

Since $\hat{H}$ and $\hat{H}_0$ do not commute with each other in general, thus the order of the operators in $\hat{U}(t,t_0)$ should always be maintained. Now we solve for $\hat{U}(t,t_0)$,

$$
i\hbar\frac{\partial}{\partial t}\hat{U}(t,t_0) = \hat{H}_{int,I}(t)\,\hat{U}(t,t_0) \tag{A.18}
$$

This gives us,

$$
\begin{aligned}
\hat{U}(t,t_0) &= \hat{U}(t_0,t_0) - \frac{i}{\hbar}\int_{t_0}^{t} d\tau \hat{H}_{int,I}(\tau)\,\hat{U}(\tau,t_0) \\
&= 1 - \frac{i}{\hbar}\int_{t_0}^{t} d\tau \hat{H}_{int,I}(\tau)\,\hat{U}(\tau,t_0)
\end{aligned} \tag{A.19}
$$

By iteration, we have,

$$
\hat{U}(t,t_0) = \sum_{n=0}^{\infty}\left(\frac{-i}{\hbar}\right)^n \frac{1}{n!}\int_{t_0}^{t} d\tau_1 \cdots \int_{t_0}^{t} d\tau_n T\left[\hat{H}_{int,I}(\tau_1)\cdots\hat{H}_{int,I}(\tau_n)\right] \tag{A.20}
$$

where T is the time ordering operator, which puts the operator at the latest time to the rightmost in the operator sequence. By writing in this way, we can easily calculate $\hat{U}(t,t_0)$ numerically.

A.1.4 Green's functions

We start by defining a time-ordered Green's function.

$$
\hat{G}_{\hat{A},\hat{B}}(x,t;x',t') = \frac{-i}{\hbar}\frac{\langle\Psi_0\left|T\left[\hat{A}_H(x,t)\,\hat{B}_H(x',t')\right]\right|\Psi_0\rangle}{\langle\Psi_0|\Psi_0\rangle} \tag{A.21}
$$

where the subscript H denotes that we are working in the Heisenberg picture, $|\Psi_0\rangle$ is the ground state also in the Heisenberg picture.

In equilibrium and uniform systems, Green's functions depend only on the difference of variables.

$$\hat{G}_{\hat{A},\hat{B}}(x,t;x',t') = \hat{G}_{\hat{A},\hat{B}}(x-x',t-t') \tag{A.22}$$

Eq. (A.21) requires the exact solution $|\Psi_0\rangle$ of the perturbed system $\hat{H}$, which is usually difficult to get at the first place, and which is also exactly the final goal that we use Green's functions to solve for.

By adiabatically turning on the perturbation $\hat{H}_{int}$, Gell-Mann and Low [1] was able to show that the exact solution $|\Psi_0\rangle$ of $\hat{H}$ can be linked to the solution of the unperturbed solution $|\Phi_0\rangle$ of $\hat{H}_0$. Gell-Mann and Low theorem reads as,

$$|\Psi_0\rangle = \hat{U}(0,-\infty)|\Phi_0\rangle \tag{A.23}$$

The definition of $\hat{U}$ has been shown in the above section (Eq. (A.17)). In Eq. (A.23), we used the fact that at time $t = 0$, the ground state wave function is identical in both the Heisenberg picture and the interaction picture. In analogy, we also have,

$$\langle\Psi_0| = \langle\Phi_0|\hat{U}(\infty,0) \tag{A.24}$$

which evolves the system from $t = \infty$ "back" to $t = 0$. It is essential to realize, as shown in Gell-mann and Low's proof of their theorem (see Ref. [2] for detailed derivation), that the eigenstates $|\Psi_0\rangle$ developing out of $|\Phi_0\rangle$ as in Eq. (A.23) and Eq. (A.24) could in principle differ by a phase factor.

The possible difference in the phase is canceled out by the denominator in

the Green's function.

$$\begin{aligned}\hat{G}_{\hat{A},\hat{B}}(x,t;x',t') &= \frac{-i}{\hbar}\frac{\left\langle \Psi_0 \left| T\left[\hat{A}_H(x,t)\,\hat{B}_H(x',t')\right]\right| \Psi_0\right\rangle}{\langle\Psi_0|\Psi_0\rangle} \\ &= \frac{-i}{\hbar}\frac{\left\langle \Phi_0 \left| \hat{U}(\infty,0)\,T\left[\hat{A}_H(x,t)\,\hat{B}_H(x',t')\right]\hat{U}(0,-\infty)\right| \Phi_0\right\rangle}{\left\langle \Phi_0 \left| \hat{U}(\infty,0)\,\hat{U}(0,-\infty)\right| \Phi_0\right\rangle}\end{aligned} \tag{A.25}$$

Here we relate the operators in the Heisenberg picture with the operators in the interaction picture. From Eq. (A.6), we know that,

$$\hat{O}_H(t) = e^{i\hat{H}t/\hbar}\hat{O}_S\,e^{-i\hat{H}t/\hbar} \tag{A.26}$$

From Eq. (A.11), we know that,

$$\hat{O}_S = e^{-i\hat{H}_0 t/\hbar}\hat{O}_I(t)\,e^{i\hat{H}_0 t/\hbar} \tag{A.27}$$

Combing Eq. (A.26) and Eq. (A.27), we have,

$$\hat{O}_H(t) = e^{i\hat{H}t/\hbar}e^{-i\hat{H}_0 t/\hbar}\hat{O}_I(t)\,e^{i\hat{H}_0 t/\hbar}e^{-i\hat{H}t/\hbar} \tag{A.28}$$

Noticing that $\hat{U}(t,t_0) = e^{i\hat{H}_0 t/\hbar}e^{-i\hat{H}(t-t_0)/\hbar}e^{-i\hat{H}_0 t/\hbar}$ (Eq. (A.17)). We have,

$$\hat{O}_H(t) = \hat{U}(0,t)\,\hat{O}_I(t)\,\hat{U}(t,0) \tag{A.29}$$

Thus, the Green's function can be rewritten as,

$$\hat{G}_{\hat{A},\hat{B}}(x,t;x',t') = \frac{-i}{\hbar}\frac{\left\langle \Phi_0 \left| \hat{U}(\infty,0)\,T\left[\hat{U}(0,t)\,\hat{A}_I(x,t)\,\hat{U}(t,t')\,\hat{B}_I(x',t')\,\hat{U}(t',0)\right]\hat{U}(0,-\infty)\right| \Phi_0\right\rangle}{\left\langle \Phi_0 \left| \hat{U}(\infty,-\infty)\right| \Phi_0\right\rangle} \tag{A.30}$$

As in a time-ordered Green's function, we can move the operators in the numerator around. One can show that,

$$\hat{G}_{\hat{A},\hat{B}}(x,t;x',t') = \frac{-i}{\hbar}\frac{\langle \Phi_0 \left| T\left[\hat{U}(\infty,-\infty)\,\hat{A}_I(x,t)\,\hat{B}_I(x',t')\right]\right| \Phi_0\rangle}{\langle \Phi_0 \left| \hat{U}(\infty,-\infty)\right| \Phi_0\rangle} \tag{A.31}$$

Generally, the operators $\hat{A}$ and $\hat{B}$ are many-body operators. We then need to apply Wick's theorem to evaluate the expectation values with respect to $|\Phi_0\rangle$.

The time-ordered Green's function can be easily evaluated systematically in the procedure shown above. Here we define several more different types of Green's functions.

- the retarded Green's function: $\hat{G}^{r}_{\hat{A},\hat{B}}(x,t;x',t') = -i\theta(t-t')\langle\left\{\hat{A}(x,t),\hat{B}(x',t')\right\}\rangle$
- the advanced Green's function: $\hat{G}^{a}_{\hat{A},\hat{B}}(x,t;x',t') = i\theta(t'-t)\langle\left\{\hat{A}(x,t),\hat{B}(x',t')\right\}\rangle$
- the lesser Green's function: $\hat{G}^{<}_{\hat{A},\hat{B}}(x,t;x',t') = i\langle\hat{B}(x',t')\hat{A}(x,t)\rangle$
- the greater Green's function: $\hat{G}^{>}_{\hat{A},\hat{B}}(x,t;x',t') = -i\langle\hat{A}(x,t)\hat{B}(x',t')\rangle$

The curly bracket {} is the anti-commutator for fermions and the commutator for bosons. These Green's functions provide a powerful technique to compute many properties of many-body systems. For example, the response function can be calculated from the retarded and advanced Green's functions, while information on the state of the system is provided by the lesser and greater Green's functions. The imaginary parts of these Green's functions provide information about the density of states etc.

A.2 Self-interaction error

As mentioned in the introduction chapter, for mesoscopic systems, the electron transport process requires a full quantum description. The Landauer formula and the non-equilibrium Green's function (NEGF) formulation are among the most popular of such theories. For scattering processes in non-interacting systems, they are essentially equivalent to each other. It is only in the case of scattering processes in interacting systems that the NEGF formalism shows great

advantages. For any practical electron transport calculations, one usually combines NEGF together with an electronic structure theory, typically density functional theory (DFT). Such a scheme is computationally inexpensive since DFT is a single-particle method, and physically useful to help people understand more realistically the electron scattering process. One of the problems with DFT is the so-called self-interaction error (SIE), which is one of the major problems that makes DFT fail badly in certain circumstances, one of which is that DFT overestimates the conductance as shown in [3].

In density functional theory, one can write down the electronic ground state energy as a functional of the electron density ρ,

$$E[\rho] = T[\rho] + V[\rho] + J[\rho] + E_{xc}[\rho] \tag{A.32}$$

where T is the kinetic energy of a non-interacting reference system with the same density, V represents the electron-nuclear interaction, $J[\rho] = \frac{1}{2}\int d\mathbf{r}d\mathbf{r}' \left([\rho(\mathbf{r})\rho(\mathbf{r}')]/|\mathbf{r}-\mathbf{r}'|\right)$ is the electron-electron Coulomb repulsion energy, and E_{xc} is the exchange-correlation energy functional.

For systems with only a single electron such as a hydrogen atom, there will not be any electron-electron interactions. In this case, T and V are the exact kinetic and potential energies of the system, and the sum of J and E_{xc} should be equal to zero. Exact density functionals should also satisfy this relation.

$$J + E_{xc} = 0 \tag{A.33}$$

Unfortunately for most of the parametrized density functionals available, this sum is not zero. Physically, it is equivalent to saying that the electron is interacting with itself through the functional that is non-linearly dependent on the electron density. This is the so-called self-interaction error (SIE) in a one-electron

system

$$\text{SIE} = J + E_{xc} \tag{A.34}$$

For systems with more than just one electron, the definition of SIE has been generalized recently in the following work [4].

A.3 Calculating surface Green's function via numerical renormalization group

We use tight-binding model to describe the electrodes and also the coupling between the electrodes and the molecule. Since only the surface layer of the electrodes and directly coupled to the molecule, only the surface Green's function of the electrodes are necessary in order to calculate the self-energies that effectively modifies the molecular part of the total Hamiltonian. The contributions from the layers deep in the bulk electrodes can be incorporated through a numerical renormalization group procedure as shown in Ref. [5]. We show a schematic procedure to illustrate the renormalization group method as shown in Fig. (A.1). There are two key steps in the renormalization group method, namely, blocking and decimation. As in our example, in the blocking step, we group the two neighbouring sites into a block. In the decimation step, we transform the block into an effective site. By progressively applying the blocking and decimation steps, we can extract the information of very large systems (often in their thermodynamic limit), such as ground state, phase diagram and as in this case the surface Green's function.

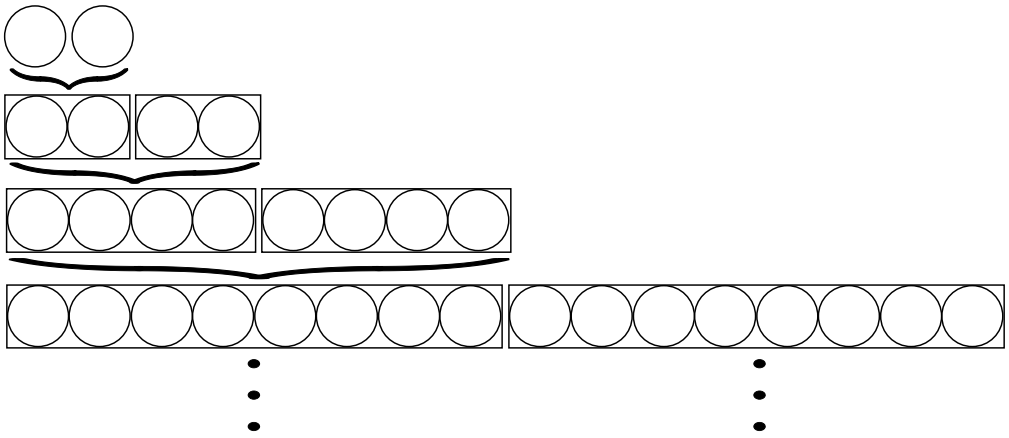

Figure A.1: Renormalization group method for tight-binding description of the electrodes.

We start from the total Green's function for a uniform system.

$$(\omega - H)\, G\,(\omega) = I \tag{A.35}$$

where the Hamiltonian possesses a tridiagonal form. Here we show the first few layers of the right electrode in a matrix form.

H_{00}	H_{01}	0	0	0	$\cdots$
H_{10}	H_{11}	H_{12}	0	0	$\cdots$
0	H_{21}	H_{22}	H_{23}	0	$\cdots$
0	0	H_{32}	H_{33}	H_{34}	$\cdots$
0	0	0	H_{43}	H_{44}	$\cdots$
$\vdots$	$\vdots$	$\vdots$	$\vdots$	$\vdots$	$\ddots$

where H_{00} couples with the molecular part of the total Hamiltonian.

By expanding the matrix multiplication, we can get,

$$(\omega - H_{00})\, G_{00}\,(\omega) = I + H_{01} G_{10} \tag{A.36}$$

$$(\omega - H_{11})\, G_{10}\,(\omega) = H_{10} G_{00} + H_{12} G_{20} \tag{A.37}$$

$$(\omega - H_{22})\, G_{20}(\omega) = H_{21}G_{10} + H_{13}G_{30} \tag{A.38}$$

$$\cdots$$

$$(\omega - H_{nn})\, G_{n0}(\omega) = H_{n,n-1}G_{n-1,0} + H_{n-1,n+1}G_{n+1,0} \tag{A.39}$$

We assume that $H_{n,n-1} = H_{10}$, for any $n \in (1, 2, \cdots, n)$. If we further assume that all the on-site energies are the same, i.e., $H_{nn} = H_{00}$. Thus we have,

$$(\omega - H_{00})\, G_{00}(\omega) = I + H_{01}G_{10} \tag{A.40}$$

$$(\omega - H_{00})\, G_{10}(\omega) = H_{10}G_{00} + H_{01}G_{20} \tag{A.41}$$

$$\cdots \tag{A.42}$$

$$(\omega - H_{00})\, G_{n0}(\omega) = H_{10}G_{n-1,0} + H_{01}G_{n+1,0} \tag{A.43}$$

Note $H_{10} = H_{01}^{\dagger}$. Setting $n = 1$, we have,

$$G_{10}(\omega) = (\omega - H_{00})^{-1} (H_{10}G_{00} + H_{01}G_{20}) \tag{A.44}$$

Combing Eq. (A.40) and Eq. (A.44), we have,

$$(\omega - H_{00})\, G_{00}(\omega) = I + H_{01}G_{10} = I + H_{01}(\omega - H_{00})^{-1} (H_{10}G_{00} + H_{01}G_{20}) \tag{A.45}$$

$$\left(\omega - H_{00} - H_{01}(\omega - H_{00})^{-1} H_{10}\right) G_{00}(\omega) = I + H_{01}(\omega - H_{00})^{-1} H_{01}G_{20} \tag{A.46}$$

We can calculate G_{00}, if G_{20} is known. Similarly, we can replace $G_{n-1,0}$ and $G_{n+1,0}$ in Eq. (A.43), and we have,

$$\left(\omega - H_{00} - H_{01}(\omega - H_{00})^{-1} H_{10} - H_{10}(\omega - H_{00})^{-1} H_{01}\right) G_{n0} =$$
$$H_{10}(\omega - H_{00})^{-1} H_{10}G_{n-2,0} + H_{01}(\omega - H_{00})^{-1} H_{01}G_{n+2,0} \tag{A.47}$$

As a short summary, the equations read as,

$$(\omega - \varepsilon_{1S})\, G_{00} = I + \alpha_1 G_{20} \tag{A.48}$$

$$(\omega - \varepsilon_1)\, G_{n0} = \beta_1 G_{n-2,0} + \alpha_1 G_{n+2,0} \tag{A.49}$$

$$(\omega - \varepsilon_1)\, G_{nn} = I + \beta_1 G_{n-2,n} + \alpha_1 G_{n+2,n} \tag{A.50}$$

with $n \geq 2$ and

$$\alpha_1 = H_{01}(\omega - H_{00})^{-1} H_{01} \quad \text{(A.51)}$$

$$\beta_1 = H_{10}(\omega - H_{00})^{-1} H_{10} \quad \text{(A.52)}$$

$$\varepsilon_{1S} = H_{00} + H_{01}(\omega - H_{00})^{-1} H_{10} \quad \text{(A.53)}$$

$$\varepsilon_1 = H_{00} + H_{01}(\omega - H_{00})^{-1} H_{10} + H_{10}(\omega - H_{00})^{-1} H_{01} \quad \text{(A.54)}$$

Notice that Eq. (A.48) - Eq. (A.50) now involve only the even indices, we can rewrite the equations as,

$$(\omega - \varepsilon_{1S}) G_{00} = I + \alpha_1 G_{20} \quad \text{(A.55)}$$

$$(\omega - \varepsilon_1) G_{2n,0} = \beta_1 G_{2(n-1),0} + \alpha_1 G_{2(n+1),0} \quad \text{(A.56)}$$

$$(\omega - \varepsilon_1) G_{2n,2n} = I + \beta_1 G_{2(n-1),2n} + \alpha_1 G_{2(n+1),2n} \quad \text{(A.57)}$$

The equations above have effectively transformed two layers to one unit layer. Comparing these equations with Eq. (A.51) - Eq. (A.54), after i iterations, we arrive,

$$\alpha_i = \alpha_{i-1}(\omega - \varepsilon_{i-1}) \alpha_{i-1} \quad \text{(A.58)}$$

$$\beta_i = \beta_{i-1}(\omega - \varepsilon_{i-1}) \beta_{i-1} \quad \text{(A.59)}$$

$$\varepsilon_{iS} = \varepsilon_{i-1,S} + \alpha_{i-1}(\omega - \varepsilon_{i-1})^{-1} \beta_{i-1} \quad \text{(A.60)}$$

$$\varepsilon_i = \varepsilon_{i-1} + \alpha_{i-1}(\omega - \varepsilon_{i-1})^{-1} \beta_{i-1} + \beta_{i-1}(\omega - \varepsilon_{i-1})^{-1} \alpha_{i-1} \quad \text{(A.61)}$$

where $\varepsilon_0 = H_{00}$, $\alpha_0 = H_{01}$, and $\beta_0 = H_{10}$.

The Green's functions now read as,

$$(\omega - \varepsilon_{iS}) G_{00} = I + \alpha_i G_{2^i n,0} \quad \text{(A.62)}$$

$$(\omega - \varepsilon_i) G_{2^i n,0} = \beta_i G_{2^i(n-1),0} + \alpha_i G_{2^i(n+1),0} \quad \text{(A.63)}$$

with $n \geq 1$. This iterative procedure is carried out until α_i and β_i are small enough. Then we have,

$$\varepsilon_i \simeq \varepsilon_{i-1} \tag{A.64}$$

$$\varepsilon_{i,S} \simeq \varepsilon_{i-1,S} \tag{A.65}$$

$$(\omega - \varepsilon_{iS})\, G_{00} \simeq I \tag{A.66}$$

Therefore the surface Green's function can be calculated by,

$$G_{00} \simeq (\omega - \varepsilon_{iS})^{-1} \tag{A.67}$$

Note these derivations calculate the left surface Green's function. The right surface Green's function is given by,

$$\bar{G}_{00} \simeq (\omega - \bar{\varepsilon}_{iS})^{-1} \tag{A.68}$$

where $\bar{\varepsilon}_{iS} = \bar{\varepsilon}_{i-1,S} + \beta_{i-1}\,(\omega - \varepsilon_{i-1})^{-1}\,\alpha_{i-1}$ starting with $\bar{\varepsilon}_{0S} = \varepsilon_{0S} = H_{00}$.

A.4 PPP model Hamiltonian

We used the Pariser-Parr-Pople (PPP) model Hamiltonian to describe the electronic structure of the π conjugated graphene nanoribbons. The PPP Hamiltonian reads as,

$$\mathcal{H} = -\sum_{\langle ij \rangle} t_{ij} c_i^{\dagger} c_j + \sum_{ij} \gamma_{ij}\,(n_i - 1)\left(n_j - 1\right) \tag{A.69}$$

where the first term is the tight-binding Hamiltonian representing the hopping between nearest neighbouring sites, and the second term represents the Coulomb repulsion. For the Coulomb repulsion term, here we use the Mataga-Nishimoto parametrization scheme [6], n_i is the occupation number of site i,

and

$$\gamma_{ij} = \frac{1}{\epsilon_0 \left(\gamma_0^{-1} + R_{ij}\right)} \tag{A.70}$$

with $\gamma_0 = 10.84eV$, ϵ_0 is the dielectric constant, and R_{ij} is the distance between site i and site j.

Comparing directly with *ab-initio* Hamiltonian, we have the following mappings,

$$-t_{ii} = h_{ii} + \sum_{q \neq i} J_{qqii} \tag{A.71}$$

$$-t_{ij} = h_{ij} + \sum_{q} J_{qqij} n_q \tag{A.72}$$

$$\gamma_{ij} = J_{iijj} \tag{A.73}$$

where h_{ij} and J_{pqrs} are the effective one-electron integrals and two-electron Coulomb integrals, respectively.

$$h_{pq} = \left\langle p \left| -\frac{1}{2}\nabla^2 + V_{eff} \right| q \right\rangle \tag{A.74}$$

$$J_{pqrs} = \left\langle pq \left| \frac{1}{|\mathbf{r} - \mathbf{r}'|} \right| rs \right\rangle \tag{A.75}$$

with V_{eff} defined as a sum over the nuclei and core orbitals of all atoms,

$$V_{eff} = -\sum_{A} \left\langle p \left| \frac{1}{|\mathbf{r} - \mathbf{R}_A|} \right| q \right\rangle + \sum_{i \in core(A)} \left(2J^A_{pqii} - J^A_{piqi}\right) \tag{A.76}$$

It is clear from the definitions above, in the PPP Hamiltonian, all exchange and hybrid two-electron integrals are simply neglected.

BIBLIOGRAPHY

[1] M. Gell-mann and F. Low. Bound States in Quantum Field Theory. *Phys. Rev.*, 84:350, 1951.

[2] A. L. Fetter and J. D. Walecka. *Quantum Theory of Many-Particle Systems*. Dover, 2003.

[3] C. Toher, A. Filippetti, S. Sanvito, and K. Burke. Self-Interaction Errors in Density-Functional Calculations of Electronic Transport. *Phys. Rev. Lett.*, 95:146402, 2005.

[4] P. Mori-Sánchez, A. J. Cohen, and W.Yang. Many-Electron Self-Interaction Error in Approximate Density Functionals. *J. Chem. Phys.*, 125:201102, 2006.

[5] M. P. Lopez Sancho, J. M. Lopez Sancho, J. M. L. Sancho, and J. Rubio. Highly Convergent Schemes for the Calculation of Bulk and Surface Green Functions. *J. Phys. F: Met. Phys.*, 15:851, 1985.

[6] N. Mataga and K. Nishimoto. Electronic Structure and Spectra of Nitrogen Heterocycles. *Z. Phys. Chem. (Frankfurt)*, 13:140, 1957.